

Summer 2013

# Exploration of aqueous interfaces and their effect on ion behavior

Oneka T. Cummings

Follow this and additional works at: <https://digitalcommons.latech.edu/dissertations>

 Part of the [Applied Mathematics Commons](#), and the [Physical Chemistry Commons](#)

---

**EXPLORATION OF AQUEOUS INTERFACES  
AND THEIR EFFECT ON ION  
BEHAVIOR**

by

Oneka T. Cummings, B.S., M.S.

A Dissertation Presented in Partial Fulfillment  
of the Requirements of the Degree  
Doctor of Philosophy

COLLEGE OF ENGINEERING AND SCIENCE  
LOUISIANA TECH UNIVERSITY

August 2013

UMI Number: 3577729

All rights reserved

INFORMATION TO ALL USERS

The quality of this reproduction is dependent upon the quality of the copy submitted.

In the unlikely event that the author did not send a complete manuscript and there are missing pages, these will be noted. Also, if material had to be removed, a note will indicate the deletion.

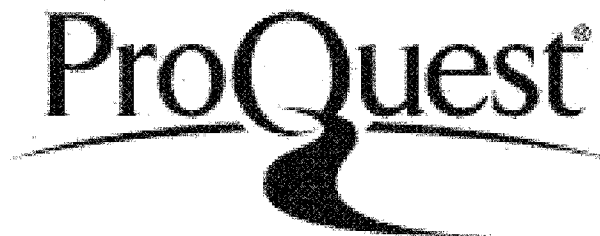


UMI 3577729

Published by ProQuest LLC 2014. Copyright in the Dissertation held by the Author.

Microform Edition © ProQuest LLC.

All rights reserved. This work is protected against unauthorized copying under Title 17, United States Code.



ProQuest LLC  
789 East Eisenhower Parkway  
P.O. Box 1346  
Ann Arbor, MI 48106-1346

LOUISIANA TECH UNIVERSITY  
THE GRADUATE SCHOOL

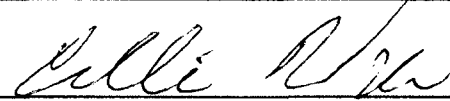
MAY 15, 2013

Date

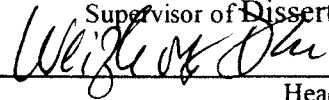
We hereby recommend that the dissertation prepared under our supervision by  
**Oneka T. Cummings, B.S., M.S.**

Entitled **Exploration of Aqueous Interfaces and Their Effect on Ion Behavior**

be accepted in partial fulfillment of the requirements for the Degree of  
**Doctor of Philosophy**



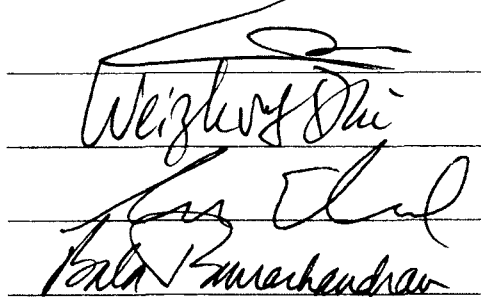
Supervisor of Dissertation Research



Head of Department

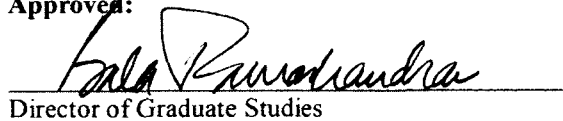
**COMPUTATIONAL ANALYSIS & MODELING**  
Department

Recommendation concurred in:



Advisory Committee

Approved:



Director of Graduate Studies

Approved:



Dean of the Graduate School



Dean of the College

## ABSTRACT

An in-depth understanding of a wide range of physical, chemical, atmospheric and biological processes can only be achieved after the structure and dynamics of interfaces and the interfacial behavior of aqueous species, such as ions, are thoroughly studied and understood. This dissertation describes computational studies conducted to gain a more comprehensive understanding of such interfaces and the behavior of ions in the bulk and interfacial regions of the (1) air/water interface, and (2) alkane/water interfaces.

At the air/water interface the effect of counterion (sodium cations) charge and the influence of ion pairing on anion (chloride) propensity for the air/water interface of water was investigated. Higher counterion charge led to greater interfacial activity of the chloride anions and also caused stronger binding between the sodium and chloride ions. Shorter sodium-chloride interatomic distance also led to greater anion interfacial propensity while dampening the interaction strength between the counterion and anion had a small effect on propensity of the anions for the interface. Another phenomenon examined at the air/water interface was the effect of the halide ion in various sodium halide electrolyte solutions on the surface tension and surface excess while including electrostatic damping in the simulation model. Divalent strontium chloride was also examined in comparison to monovalent sodium chloride. Findings suggested that the smaller halide ions were found farthest from the air/water interface—in keeping with

trends from previous studies—and resulted in the largest (most negative) surface excess, which would in turn cause the greatest increase in surface tension of water. Divalent strontium chloride had a more negative surface excess when compared to sodium chloride and the inclusion of electrostatic damping in the models reduced propensity of the ions for the interface and caused overall increase in surface excess.

The alkane/water interface was investigated to determine the effect of changing the length of the alkyl chain on the water/alkane interfacial width. Two separate studies found that longer alkane chain length led to shorter alkane/water interfacial widths. A long term goal of this research is to catalog the behavior of ionic species at different interfaces. The distribution of sodium-halide ions was compared at the alkane/water and air/water interfaces. Sodium halide ions were found closer to the air/water interface than the alkane/water interface. In the future, similar studies will be carried out at the alcohol/water interface and the effects of the nature of the organic phase (alkane or alcohol with varied chain lengths, degrees of branching, and solubility in water) will be examined.

## APPROVAL FOR SCHOLARLY DISSEMINATION

The author grants to the Prescott Memorial Library of Louisiana Tech University the right to reproduce, by appropriate methods, upon request, any or all portions of this Dissertation. It is understood that "proper request" consists of the agreement, on the part of the requesting party, that said reproduction is for his personal use and that subsequent reproduction will not occur without written approval of the author of this Dissertation. Further, any portions of the Dissertation used in books, papers, and other works must be appropriately referenced to this Dissertation.

Finally, the author of this Dissertation reserves the right to publish freely, in the literature, at any time, any or all portions of this Dissertation.

Author 

Date June 21, 2013

## **DEDICATION**

For: Merleen, Burchell, Eugene, and Rudolph.

## TABLE OF CONTENTS

ABSTRACT.....	iii
DEDICATION.....	vi
LIST OF TABLES.....	xii
LIST OF FIGURES.....	xiii
ACKNOWLEDGMENTS.....	xvi
CHAPTER 1 INTRODUCTION.....	1
1.1 Motivation.....	2
1.2 Background.....	4
1.2.1 Air/Water Interface.....	4
1.2.2 Hydrophobic/Water Interfaces.....	6
1.2.3 Ions at Different Interfaces.....	8
CHAPTER 2 METHODS.....	10
2.1 Computer Simulations Techniques.....	10
2.2 Molecular Dynamics.....	12
2.2.1 Numerical Integration Methods.....	13
2.2.2 The Verlet Algorithm.....	14
2.2.3 The Velocity Verlet Algorithm.....	15
2.3 Statistical Ensembles.....	16
2.3.1 Statistical Mechanics.....	16
2.3.2 Microcanonical Ensemble (NVE).....	17

2.3.3	Canonical Ensemble (NVT).....	17
2.3.4	Isothermal Isobaric Ensemble (NpT).....	18
2.3.5	Thermostats and Barostats .....	18
2.4	Thermodynamics Properties .....	20
2.5	Radial Distribution Function (RDF).....	21
2.6	Force Fields.....	24
2.6.1	Lennard-Jones Potential.....	26
2.6.2	Coulomb Potential .....	27
2.6.3	Polarizable Interactions and Polarizability .....	28
2.6.4	Always Stable Predictor Corrector (ASPC) Method.....	29
CHAPTER 3 INFLUENCE OF THE COUNTERION ON ANION PROPENSITY		
	FOR THE AIR/WATER INTERFACE .....	31
3.1	Introduction.....	31
3.2	Simulation Details.....	33
3.2.1	Concentrated Systems.....	33
3.2.2	Single Ion Pairs .....	35
3.3	Results and Discussions.....	36
3.3.1	Density Profiles.....	36
3.3.2	Radial Distribution Functions (RDFs).....	37
3.3.3	Induced Dipole.....	40
3.3.4	Free Energy Profiles .....	41
3.4	Conclusions.....	45
CHAPTER 4 EFFECT OF IONS ON SURFACE TENSION OF WATER WITH		
	ELECTROSTATIC DAMPING .....	46
4.1	Introduction.....	46

4.2	Model Development .....	47
4.2.1	Interaction Potential Form .....	47
4.2.2	Ion-Water Interaction Parameterization.....	50
4.2.3	Ion-Ion Interaction Parameterization .....	52
4.3	Simulation Details.....	53
4.4	Results and Discussions.....	55
4.4.1	Single Ion Solvation.....	55
4.4.2	Concentrated Bulk Aqueous Solutions .....	57
4.4.3	Interfacial Ion Distributions .....	60
4.4.4	Surface Tensions and Excesses.....	66
4.5	Conclusions.....	68
<b>CHAPTER 5 EXPLORATION OF PROPERTIES OF THE N-ALKANE/WATER</b>		
	<b>INTERFACE .....</b>	<b>70</b>
5.1	Introduction.....	70
5.2	Simulation Details.....	71
5.2.1	Molecular Models .....	71
5.2.2	Simulation Details.....	73
5.3	Results and Discussions.....	75
5.3.1	Density Profiles, Interfacial Tensions and Widths.....	75
5.3.2	Interfacial Structural Expansion and Contraction .....	78
5.3.3	Molecular Orientation.....	84
5.3.4	Electrostatic Potential .....	86
5.4	Conclusions.....	88

## CHAPTER 6 THE EFFECT OF ALKYL CHAIN LENGTH ON ALKANE/WATER

INTERFACIAL WIDTH.....	90
6.1 Introduction.....	90
6.2 Simulation Details.....	91
6.3 Results and Discussions.....	93
6.3.1 Density Profiles.....	93
6.3.2 Electron Density Profiles and X-ray Reflectivity .....	95
6.3.3 Capillary Wave Theory.....	99
6.3.4 Distribution of Carbons.....	102
6.4 Conclusion and Future Work.....	105
CHAPTER 7 A COMPARISON OF IONS AT THE AIR/ WATER AND <i>N</i> -	
ALKANE/WATER INTERFACES.....	107
7.1 Introduction.....	107
7.2 Simulation Details.....	108
7.2.1 Molecular Models .....	108
7.2.2 Simulation Details.....	108
7.3 Results and Discussions.....	109
7.4 Conclusions.....	113
APPENDIX A THE WATER MODEL .....	114
A.1 The Water Model.....	115
A.2 The Dang-Chang Water Model.....	116
A.3 The Flexible Water Model.....	116
APPENDIX B EXPLANATION OF TERMINOLOGY.....	118
B.1 SHAKE and RATTLE.....	119
B.2 Potential Mean Force (PMF) .....	120

B.3	Potential Truncation and Analytical Tail Corrections .....	121
B.4	Particle Mesh Ewald Summation Technique.....	122
BIBLIOGRAPHY .....		124

## LIST OF TABLES

<b>Table 4-1:</b> Showing Force Field Parameters Used to Describe the Ions .....	49
<b>Table 4-2:</b> Showing a Comparison of the Free Energy of Hydration for the Ions Investigated .....	56
<b>Table 4-3:</b> The Value of $\delta$ used and a Comparison of the $a_{cc}$ Values Calculated from Simulation and Experimental Activity Coefficients According to Eq 4-12... 60	60
<b>Table 4-4:</b> Showing Computed versus Experimental Surface Excesses.....	67
<b>Table 5-1:</b> Intermolecular Parameters Used for the Alkane Force Field .....	72
<b>Table 5-2:</b> Comparison between Simulation and Experiment for the Bulk Densities and Heats of Vaporizations for the Bulk Alkane Systems Investigated .....	73
<b>Table 5-3:</b> Showing a Comparison of the Simulation and Experimental Interfacial Tensions .....	75
<b>Table 5-4:</b> Interfacial Widths (in Å) of the Water and Alkane Phases as Fit by a Hyperbolic Tangent Function, Along with the Distance Between the Gibbs Dividing Surfaces (GDS) of the Alkane and Water Phases. ....	77
<b>Table 6-1:</b> Interfacial Width in Å of the <i>n</i> -Alkane Water Systems Studied, Including a Fit to the Raw Data (Raw), the Values Extracted from Eq. 6.6 ( $\sigma_{cw}$ ), and the Results From a Fit to the Raw Data Convolved With a Gaussian of Width $\sigma_{cw}$ (Conv). The uncertainties for all numbers were between 0.02 to 0.03 Å.....	99
<b>Table 7-1:</b> Showing a comparison of the Simulation and Experimental Interfacial Tensions .....	112

## LIST OF FIGURES

<b>Figure 2-1:</b> Showing the spherical shell of thickness $\delta r$ used to calculate the radial distribution function .....	22
<b>Figure 2-2:</b> Radial distribution function determined from molecular dynamics simulation of an aqueous 1M NaCl solution at 298K. The RDF is between the water oxygen and the chloride ion in the NaCl.....	23
<b>Figure 3-1:</b> Showing a snapshot of the air/water interface with NaCl ions.....	32
<b>Figure 3-2:</b> Density profiles of sodium (bottom) and chloride (bottom) ions as a function of distance from the GDS.....	36
<b>Figure 3-3:</b> Sodium-chloride RDFs for the systems investigated.....	38
<b>Figure 3-4:</b> Sodium-oxygen (top) and chloride-oxygen (bottom) RDFs. The insets showed a closeup of the first peak of the Cl-O RDF.....	39
<b>Figure 3-5:</b> Average anion induced dipole as a function of position for the systems investigated.....	40
<b>Figure 3-6:</b> PMFs for a single chloride and the NaCl pair for the systems investigated with $r_0=2.25 \text{ \AA}$ .....	42
<b>Figure 3-7:</b> Angular distribution of NaCl for the different single ion systems investigated.....	43
<b>Figure 3-8:</b> A comparison of the PMFs for chloride alone and for NaCl with $r_0=2.25 \text{ \AA}$ and $r_0=4.5 \text{ \AA}$ . .....	44
<b>Figure 4-1:</b> Cation-oxygen (top), anion-oxygen (bottom, dashed lines), and anion-hydrogen (bottom, solid lines) RDFs from the 3M NaX systems and the 2.7M SrCl <sub>2</sub> system.....	57
<b>Figure 4-2:</b> Cation-anion RDFs for the 3M NaX and 2.7 M SrCl <sub>2</sub> systems .....	58
<b>Figure 4-3:</b> KB integrals as a function of integration distance obtained from the 3M NaX and 2.7M SrCl <sub>2</sub> systems.....	59
<b>Figure 4-4:</b> Density profiles of 1M (blue lines) and 3M (red lines) NaX systems.....	61

<b>Figure 4-5:</b> Density profiles of 1M NaX systems comparing our model (solid lines) with the D-C model (dashed lines).....	63
<b>Figure 4-6:</b> Density profiles of the 1M and 2.7M SrCl <sub>2</sub> solutions.....	65
<b>Figure 5-1:</b> Showing a snapshot of the alkane/water interface.....	71
<b>Figure 5-2:</b> Density profiles for water (solid lines) and alkanes (dashed lines) for the systems described. The GDS of water is represented as zero. ....	76
<b>Figure 5-3:</b> Average distance between water oxygens in first solvation shell as a function of water center of mass position.....	79
<b>Figure 5-4:</b> Average induced dipole of water as a function of center of mass position ..	80
<b>Figure 5-5:</b> Average distance between carbons of different molecules in first solvation shell as a function of carbon atomic positions.....	81
<b>Figure 5-6:</b> Average induced dipole of alkane molecules as a function of alkane center of mass position .....	82
<b>Figure 5-7:</b> Alkane end to end distance squared divided by the number of carbons squared as a function of alkane center of mass position. ....	83
<b>Figure 5-8:</b> Profile of average orientational order from the angle of the vector between adjacent carbons and the z-axis as a function of atomic position. ....	85
<b>Figure 5-9:</b> Electrostatic potential as a function of position for the whole system (solid lines), from water molecules alone (dotted lines), and from alkane molecules alone (dashed lines).....	87
<b>Figure 6-1:</b> Density profiles for water (solid lines) and alkanes (dashed lines) for the systems described. The GDS for the water is represented as zero. ....	94
<b>Figure 6-2:</b> Electron density profiles for the <i>n</i> -alkane/water systems studied. The GDS for the water is represented as zero. ....	96
<b>Figure 6-3:</b> Logarithm of x-ray reflectivity, normalized to Fresnel reflectivity $R_F(q_Z^T)$ , as a function of $q_Z q_Z^T$ , for the <i>n</i> -alkane/water systems obtained from the raw electron density data. ....	98
<b>Figure 6-4:</b> Logarithm of x-ray reflectivity, normalized to Fresnel reflectivity $R_F(q_Z^T)$ , as a function of $q_Z q_Z^T$ , for the <i>n</i> -alkane/water systems obtained from the electron density data convoluted using the capillary wave theory.....	101

- Figure 6-5:** The distribution of methylene carbons compare to methyl carbons in the *n*-hexane-water (solid lines) and *n*-nonane-water (dashed lines) systems studied. The GDS for the water is represented as zero..... 103
- Figure 6-6:** The electron density of methyl and methylene carbons and hydrogens (bottom) and integral of these electron density profiles (top) as a function of distance from the atom centers ..... 104
- Figure 7-1:** Distribution of NaX ions as a function of position for the OCT system and the air/water interface with X<sup>-</sup> being chloride (bottom figure), bromide (middle figure), and iodide (top figure). ..... 110
- Figure A-1:** Snapshot of the possible geometries for the rigid water model ranging from three to six interaction sites.....115

## ACKNOWLEDGMENTS

I would like to thank my advisor, Dr. Collin Wick, for his guidance and support throughout graduate school has been invaluable to me. Additionally, I want to acknowledge Dr. Bala “Ramu” Ramuchandran, Dr. Weizhong Dai, Dr. Sven Eklund, and Dr. Chokchai “Box” Leangsuksun who took time out from their busy schedules to be a part of my advisory committee; all your contributions to my overall success have been greatly appreciated.

I would also like to thank my family and friends, who were my support system throughout graduate school: Merleen Forde, Burchell Forde, Eugene Forde, Rudolph Forde, Averil Bunbury, Patricia Mendonca, John Brown, Judith Mendes, Christina Sugirtharaj, Troy Browne, Dacia Carter, Renata Valz, David Irakiza, Krystal Corbett, Abena Primo, Ankunda Kiremire, Alicia Boudreaux, Rachel Parks and many others. I could not have made it to the end of this journey without your continued support.

This material is based upon work supported by the National Science Foundation under the NSF EPSCoR Cooperative Agreement No. EPS-1003897 with additional support from the Louisiana Board of Regents. The simulations were carried out using the resources from the Louisiana Optical Network Initiative (LONI).

## CHAPTER 1

### INTRODUCTION

Over the past few decades, computer simulations have evolved into an essential branch of science and computer simulation techniques have become indispensable tools [1-3]. Computer simulations are often used to provide a hint to experimentalists for further investigations (as a complement to experiment) and are sometimes the only available method when experiments are not possible. Among other reasons, computations are often cheaper and faster than physical experiments. In most cases different possibilities can be explored simultaneously which means that unlikely scenarios can be ruled out before expensive physical experiments are conducted [2]. Molecular modeling as a whole aims to mimic the behavior and properties of molecules and molecular systems to study complex processes [2]. Furthermore, molecular simulations can provide microscopic level details about systems which cannot be explained by macroscopic experiments. Molecular Dynamics (MD) is the simulation technique used to study the air/water and alkane/water interfacial systems discussed in this dissertation. Molecular dynamics is one of the available simulation techniques available for investigation molecular systems. Monte Carlo (MC) is another one of these methods that will be described briefly in Chapter 2 along with more details about MD simulations. Simply stated however, MD is employed as the computational method for this research because

of its major advantage over other methods like MC. While other methods like MC provide a smeared picture of the system studied, MD provides a detailed movie of the system.

### 1.1 Motivation

A wide range of physical, biological, atmospheric, and chemical processes occur at some '*sort of*' interface—the boundary that forms between two different phases. As a result, a detailed understanding of the properties of these interfaces will benefit eclectic fields of study which involve any one or combination of the aforementioned processes. If we can use interfacial studies to establish that a particular species has a propensity for the interface, its extraction at the interface would probably happen more readily than otherwise. Furthermore, it may be possible to exploit these tendencies to enhance the rate of many interfacial process or mechanism [4-6]. Many of the characteristics of interfaces observed at the macroscopic level can only be scrutinized at the microscopic level which requires the use of sophisticated experimental and/or computational techniques. For instance, we observe foam formation along the shore line where sea water breaks, while the edges of fresh water lakes are usually devoid of foam. At the microscopic level, scientist have detected that the presence of salts, in this case sodium chloride (NaCl), is one factor which inhibits the joining of water bubbles causing the foam to form [7].

An in depth understanding of interfaces can also lead to break through technology that can be useful in the area of waste water cleanup [8]. Simulation studies can provide insight about the behavior of water contaminants and their likelihood of binding to specific ligands which can be present in an immiscible phase and in the proximity of the interface [8-9]. Another major application of interfacial studies is in the construction of

biological membranes. Successful construction of these membranes requires a detailed understanding of how the molecules that make up the membranes interact, as well as how they interact with the molecules in the natural cellular environment [10-12].

A thorough investigation of interfaces also requires an understanding of the ability of the interfaces to interact with various species and how they are affected by other species, particularly ions. Studies at the air–water interface have revealed that the presence of ions at the interface can influence the interfacial tension and the reactivity of the surface [9]. Also, previous research has shown that the behavior of ions near the interface can influence the best means for specific ion extraction from an aqueous mixture [9]. Furthermore, the structure and stability of many proteins and membranes have been linked to the distribution of ions in the interfaces that form those systems [4, 13-15]. The composition of the marine boundary layer in the atmosphere can be affected by the nature of seawater aerosols which is influenced by the uptake of atmospheric species, and reactions of ions in the aerosols with different atmospheric species [16-17]. Many studies have been conducted to investigate hydroxyl radicals at aqueous environments. These studies are primarily motivated by the fact that the hydroxyl radical is found in significant concentrations in the lower atmosphere and is found to react with the halide ions in saltwater aerosols [18-20]. Though studies have found no significant reactions between the hydroxyl radicals and these ionic species it is important that we have a method of examining the mechanisms of such systems which are undoubtedly vital [21].

This dissertation work is aimed at increasing our understanding of interfaces using computational methods. In particular, we explored the air/water and the

alkane/water interfaces. Molecular Dynamics (MD) was the computational technique employed for the studies documented in this dissertation. More details about the computational methods are addressed in Chapter 2, and relevant information about the simulations is included in related chapters throughout the dissertation. Some common properties of interfaces that are usually of interest and are addressed in this work include surface tension, surface excess, and reactivity [9]. Since in reality interfaces rarely exist in the absence of other species which can greatly affect the nature of the interfaces, this work includes investigations of the behavior of these interfaces in the presence of various ionic species. The ionic species explored were mainly extended to the sodium halides (chloride, bromide, and iodide) and to a lesser extent strontium chloride.

## 1.2 Background

### 1.2.1 Air/Water Interface

In the past few decades, much research has been conducted with the effort of understanding ion transport and the behavior of ions at aqueous interfaces. Initially, a fairly comprehensive idea was developed about ion solvation and ion pairing at aqueous interfaces [22-23]. Many of the initial ideas came from pioneering work by Benjamin [22-23]. However, these studies excluded polarizability in their models, which was later found to be a very vital part in the understanding ion interfacial behavior. A completely different picture emerged when polarizability was included in the molecular models. The inclusion of polarizability was found to significantly enhance the anion propensity for the air/water interface [11, 24-26]. Moreover, it was found that the larger, more polarizable, the halide anion, the greater its propensity for the air-water interface [24, 27]. It should be noted that without polarizability, larger sized anions still have a propensity for the air-

water interface in comparison with smaller ones. However, this interfacial propensity was not as strong as with polarizable interactions [28-33].

When investigating the free energy profile of a single anion, chloride had a higher free energy near the interface than in the bulk [25] indicating that the chloride ion is unlikely to be found near the interface. However, concentrated NaCl solutions studied using similar models found that chloride has a propensity for the air/water interface [33-34]. Furthermore, divalent cations are found to significantly enhance this effect [35]. This led us to believe that the cation, even if it does not have a propensity for the interface itself, plays a major role in the distribution of ions at the air/water interface. The origin for this effect is not well understood, and Chapter 3 of this dissertation details a study conducted to fill this gap. This molecular dynamics simulation study looks at how the cation (counterion) charge and degree of ion pairing influence the distribution and interfacial free energy of anions at the air/water interface. In Chapter 4, we also explore the effect of the ions in sodium halide and strontium chloride electrolyte solutions on surface tension and surface tension excess. These systems include electrostatic dampening with Kirkwood-Buff integrals in the simulation model. As a result, we explore the effect of including dampening on the ion distribution and surface tensions and excesses.

The behavior of water next to the air/water interface has been widely investigated experimentally and computationally, along with how different species are affected by them [11, 24, 26, 36-45]. Comparative studies of different interfaces are not as prevalent, and discerning how specific hydrophobic species directly influence the water structure is not well understood. More recent studies have been conducted to fill this void;

developing an understanding of how water behaves next to general hydrophobic interfaces [4, 26, 33, 46-59].

### 1.2.2 Hydrophobic/Water Interfaces

Usually, hydrophobic liquids come into contact with water and results in the formation of an interface between them. It is important from both a technical and a theoretical point of view to gain detailed insight into the properties of hydrophobic/water interfaces especially since they play an important role in surface science and surfactant behavior [60]. A molecular level understanding of reactions at hydrophobic/water interfaces will strongly benefit atmospheric science, but will also provide general insight into important industrial, pharmaceutical, and biological processes like crude oil extraction [61], detergent activity [8], membrane dynamics, drug absorption [4], ion complexation [62], and phase transfer catalysis [63]. If for instance, certain species have a greater propensity for certain hydrophobic interfaces than others, it may be possible to exploit these tendencies to enhance the rate of an interfacial process, or even promote greater selectivity [4-6]. Understanding the water structure and dynamics as well as the thermodynamic properties of the interface that forms between a hydrophobic liquid and water can be exploited for the flooding of oil wells with water in secondary oil recovery [8].

Richmond and coworkers have carried out extensive work utilizing both sum frequency generation (SFG) spectroscopy and molecular simulations to make comparisons among many interfaces for the structure of water [4-6, 64]. The nature of the hydrophobic liquid that water comes in contact with has been found to significantly influence the water structure and dynamics [4-6]. This in turn influences the

thermodynamic properties of the interface as well as affects the behavior of water molecules, general reactivity, and interfacial behavior of aqueous species, such as ions. The hydrophobic/water interfaces of focus in this dissertation are various alkane/water interfaces which will be described in detail in Chapters 5 and 6 and to a lesser extent in Chapter 7.

Alkane/water interfaces are considered a prototypical system for studying the interaction of water with hydrophobic liquid surfaces [4], primarily because the molecular structure of alkanes can be easily modified by varying chain length and their degree of branching. Furthermore, alkane/water interfaces are prevalent in water flooding of oil wells [61], and understanding how different types of alkanes, including the role of chain length on alkane/water interfacial properties, can bring greater insight into this and many other processes. Previous spectroscopic studies found that for *n*-alkanes, those with an even number of carbons packed differently than those with an odd number of carbons [47]. On the other hand, molecular dynamics simulations of water next to self-assembled monolayers found that there was no significant difference in the interfacial structure when the monolayers had odd and even numbers of alkanes [65]. X-ray reflectivity studies of *n*-alkane/water interfaces found no odd/even effect in regard to interfacial width, but greater interfacial widths with longer *n*-alkane chain lengths [46, 55, 59]. These studies suggest that the chain length of *n*-alkanes may influence the interfacial structure, but the issue still requires further investigation. Even if longer alkane chain cause an increase the interfacial width, researchers still do not understand the mechanism for this phenomenon. Also, it is not conclusive whether *n*-alkanes with an odd number of carbons pack differently than those with an even number of carbons,

though this would be a reasonable assumption since self-assembled monolayers had different structures depending if they had odd or even numbers of alkanes [66]. In Chapters 5 and 6 we investigated different alkane/water interfaces in an attempt to understand the effect of the alkyl chain length on width of the alkane/water interface.

### **1.2.3 Ions at Different Interfaces**

To bring insight into many of the aforementioned processes it is necessary to understand the similarities and differences between air/water and hydrophobic/water interfaces. In the studies discussed in subsequent chapters of this dissertation, we attempt to fill part of this void with molecular dynamics studies at the air/water and alkane/water interfaces in the presence of different ionic species (sodium chloride, sodium bromide and sodium iodide). It is fairly well known that interfacial water behaves in a different manner than bulk water. However, it is much more difficult to establish how the specific type of interface influences the behavior of aqueous species. Previous work has found that different hydrophobic/water interfaces may influence ion distributions in a different manner than the air/water interface [33, 67]. However, the only investigation of the behavior of ions at the alkane/water interface was carried out without polarizable potentials [68]. As pointed out in Section 1.2.1, inclusion of polarizability in the molecular model used to study ions at aqueous interfaces was vital [28-33, 69]. For the neat air/water or for alkane adsorption to the surface of water, good models exist without polarizable interactions [54, 56-57], but when ions are present, especially, large halogen, the inclusion of polarizability significantly influences their interfacial behavior. In general, polarizable interactions cause larger, more polarizable anions to have a significant propensity for aqueous interfaces. A specific subset of polarizable potentials

are based on the Dang-Chang water model [25, 70], in which concentrated solutions of NaCl, NaBr, and NaI have enhanced anion concentrations at the air/water interface with respect to the bulk [33]. In these studies, NaI shows the greatest interfacial anion concentration, while NaCl shows the least, but still enhanced with respect to the bulk. In other studies, when carbon tetrachloride or 1,2-dichloroethane were present at the aqueous interface, anion concentrations were usually reduced in comparison with the air/water interface [33, 71-72]. However, these two hydrophobic liquids influenced interfacial ion concentration quite differently. For instance, 1,2-dichloroethane appeared to enhance the propensity of cations to a region near the hydrophobic/water interface, while carbon tetrachloride had little to no effect on NaCl interfacial concentrations [33]. Another point to consider with these cited studies is that they both examined interfaces between water and chlorinated organic liquids. However, the behavior of these ionic species in the presence of only hydrocarbons (like alkanes) may be completely different and this phenomenon needs to be investigated. Chapter 7 includes a study which attempts to shed some light on this topic. That chapter includes a study which examined the propensity of different sodium halides for the air/water interface in comparison to some alkane/water interfaces. In the future, these studies can be extended to include ions at various hydrophobic/water interfaces to provide a more detailed picture.

## CHAPTER 2

### METHODS

#### 2.1 Computer Simulations Techniques

Computer simulation techniques are an indispensable tool presently used as initial or complementary techniques to experiments to gain insight into a range of physical phenomena [1-3]. Computer simulations have evolved over the past decades into an essential branch of science utilized to solve theoretical models beyond certain approximations and to provide a hint to experimentalists for further investigations [1]. Molecular Dynamics (MD) and Monte Carlo are the most common simulation techniques used to study many-body systems—microscopic systems made up of a large number of interacting particles [1-2].

Molecular modeling as a whole is concerned with ways to mimic the behavior and properties of molecules and molecular systems—liquids, solutions, and solids—to study complex processes such as the adsorption of molecules onto surfaces and into solids and to investigate the behavior of macromolecules [2]. Macroscopic systems like these usually contain extremely large numbers of atoms or molecules, which makes it impossible to accurately compute and model properties of interest. However, computer simulation techniques usually consider small replications of the macroscopic system with

manageable number of atoms and molecules making it possible to study these systems and predict relevant properties [2].

Monte Carlo simulations probe the configuration space by trial moves of particles. Each configuration depends only on its predecessor and not upon any other configurations that were previously visited [2]. This method generates configurations randomly and uses the Metropolis algorithm—a special set of criteria used to decide whether or not to accept each new configuration [2]. The energy change from step  $n$  to  $n + 1$  is used as a trigger to accept or reject the new configuration. Paths towards lower energy are always accepted; those to higher energy are accepted with a probability governed by Boltzmann statistics. In that way, properties of the system can be calculated by averaging over all Monte Carlo moves [1].

Molecular Dynamics methods, on the other hand, are governed by the system's Hamiltonian and consequently the Hamilton's equations of motion which are integrated to move particles to new positions and to get new velocities at these new positions. This can be viewed as an advantage of MD simulations with respect to MC since it considers the whole phase space, not only the configuration space, which gives additional information about the dynamics of the system [1].

However, all MD results are only correct with respect to the model used for the simulation [1]. Consequently, simulation results are compared to theoretical predictions and experimental findings. The model is usually refined if the simulation results differ from the *real system* properties or are incompatible with *existing* theoretical manifestations [1]. Molecular dynamics, which is discussed further in this chapter, is the

computer simulation method utilized for the study of interaction potentials of the different interfacial systems included in this dissertation.

## 2.2 Molecular Dynamics

Molecular dynamics (MD) is a deterministic method, which means that the state of the system at any time can be predicted from its current state. Once we have a molecular level understanding of the dynamic behavior of any system, we can easily interpret the "macroscopic" kinetics of the bulk system [73]. MD studies the progression of a molecular system over time as a means of predicting thermodynamic and transport properties directly from the underlying interactions between the atoms and/or molecules [2, 73-74]. As a result, MD methods have been used over the past few decades as a major tool for obtaining information about the thermodynamic, structure, and dynamical properties in condensed matter, which range from simple pure liquids to more complex bimolecular systems in solution [3].

MD is concerned with both the motions within molecules themselves and collisions between different atoms and molecules [73]. The trajectory that specifies how the positions and velocities of the particles in the system vary with time is derived in sequence by solving the differential equations embodied in Newton's second law of motion, which states that force equals the rate of change of momentum ( $F = ma$ ):

$$\frac{d^2x_i}{dt^2} = \frac{Fx_i}{m_i} \quad \text{Eq. 2-1}$$

Equation Eq. 2-1 describes the motion of a particle of mass  $m_i$  along one coordinate ( $x_i$ ) where  $Fx_i$  is the force on the particle in that direction [2, 73].

In realistic models of molecular interactions, the force of each particle changes whenever the particle changes its position, or whenever any of the other particles with which it interacts changes position. Also, the motions of all the particles are coupled together which gives rise to a many-body problem that cannot be solved analytically. Under such circumstances the equations of motion are integrated using the finite difference method [2]. The finite difference methods utilized in this work for solving the equations of motion is described in Sections 2.2.2 and 2.2.3 which follow in this chapter.

The main ingredients required for any molecular dynamics simulation include: (1) a model for the interaction between system constituents —atoms, molecules, surfaces, and so on—(2) an integrator which propagates particle positions and velocities from time  $t$  to  $t + \delta t$ , and (3) a statistical ensemble—where thermodynamic quantities like pressure, temperature or the number of particles are controlled—has to be chosen [73]. Details concerning each model discussed in this dissertation will be presented in related chapters throughout. The molecular model (water model) is explained further in Section A.1. The general principles associated with the integrator and statistical ensembles are presented here in Chapter 2.

### **2.2.1 Numerical Integration Methods**

Finite difference techniques are used to generate molecular dynamics trajectories after solving the Newton's second law of motion introduced in Section 2.2 and presented in Eq. 2-1. The basic idea is that the integration is broken down into small stages, each separated in time by a fixed time  $\delta t$ . The total force on each particle in the configuration at a time  $t$  is calculated as the vector sum of its interactions with other particles. The force is used to determine the acceleration of the particles, which are then combined with

the position and velocities at the time  $t$  to calculate the positions and velocities at the time  $t + \delta t$ . The force on the particles in their new position are then determined, leading to the new positions and velocities at time  $t + 2\delta t$ , and so on. During each time step  $\delta t$ , the force is taken as being constant [2].

Several algorithms are available for integrating the equations of motion using finite difference methods; some are commonly used in molecular dynamics calculations. All of these integrating algorithms assume that the positions and dynamic properties (velocities, accelerations, etc) can be approximated as Taylor series expansions:

$$\mathbf{r}(t + \delta t) = \mathbf{r}(t) + \delta t \mathbf{v}(t) + \frac{1}{2} \delta t^2 \mathbf{a}(t) + \frac{1}{6} \delta t^3 \mathbf{b}(t) + \frac{1}{24} \delta t^4 \mathbf{c}(t) + \dots \quad \text{Eq. 2-2}$$

$$\mathbf{v}(t + \delta t) = \mathbf{v}(t) + \delta t \mathbf{a}(t) + \frac{1}{2} \delta t^2 \mathbf{b}(t) + \frac{1}{6} \delta t^3 \mathbf{c}(t) + \dots \quad \text{Eq. 2-3}$$

$$\mathbf{a}(t + \delta t) = \mathbf{a}(t) + \delta t \mathbf{b}(t) + \frac{1}{2} \delta t^2 \mathbf{c}(t) + \dots \quad \text{Eq. 2-4}$$

$$\mathbf{b}(t + \delta t) = \mathbf{b}(t) + \delta t \mathbf{c}(t) + \dots \quad \text{Eq. 2-5}$$

Where  $\mathbf{v}$  is the velocity (the first derivative of the position  $\mathbf{r}$  with respect to time),  $\mathbf{a}$  is the acceleration (second derivative),  $\mathbf{b}$  is the third derivative and so on [2]. The integration algorithms used for the molecular dynamics simulations presented in this dissertation is discussed briefly in later in Sections 2.2.2 and 2.2.3.

### 2.2.2 The Verlet Algorithm

The Verlet algorithm is the most widely used time integration algorithm available for solving the equations of motion in molecular dynamics simulations [75-76]. It is also one of the integration algorithms employed in the molecular dynamics simulations conducted and reported in this dissertation. The Verlet algorithm uses the positions and acceleration at time  $t$ , and the positions from the previous step,  $\mathbf{r}(t - \delta t)$ , to calculate the

new positions at  $\mathbf{r}(t + \delta t)$  which we have at time  $t + \delta t$ . The relationships that are obtained between these quantities and the velocities at time  $t$  can be represented as:

$$\mathbf{r}(t + \delta t) = \mathbf{r}(t) + \delta t \mathbf{v}(t) + \frac{1}{2} \delta t^2 \mathbf{a}(t) + \dots \quad \text{Eq. 2-6}$$

$$\mathbf{r}(t - \delta t) = \mathbf{r}(t) - \delta t \mathbf{v}(t) + \frac{1}{2} \delta t^2 \mathbf{a}(t) - \dots . \quad \text{Eq. 2-7}$$

Adding Eq. 2-6 and Eq. 2-7 together yields:

$$\mathbf{r}(t + \delta t) = 2\mathbf{r}(t) - \mathbf{r}(t - \delta t) + \delta t^2 \mathbf{a}(t). \quad \text{Eq. 2-8}$$

One problem with the Verlet integration algorithm, which can be observed by looking at Eq. 2-8, is that the velocities are not explicitly generated. The velocities can be calculated in a variety of ways; one of the simpler and most common ways to obtain this quantity is to divide the difference in positions at times  $t + \delta t$  and  $t - \delta t$  by  $2\delta t$ :

$$\mathbf{v}(t) = [\mathbf{r}(t + \delta t) - \mathbf{r}(t - \delta t)]/2\delta t. \quad \text{Eq. 2-9}$$

Another way to estimate the velocities is by using the half-step,  $t + \frac{1}{2}\delta t$ :

$$\mathbf{v}\left(t + \frac{1}{2}\delta t\right) = [\mathbf{r}(t + \delta t) - \mathbf{r}(t)]/\delta t. \quad \text{Eq. 2-10}$$

The Verlet algorithm is usually simple to implement and has moderate storage requirements. However, this algorithm has some disadvantages. The lack of an explicit velocity term in the equation makes calculation of the velocities a bit more challenging [2]. Some variations of the Verlet algorithm which have been developed include: the leap-frog algorithm, the velocity Verlet method, and Beeman's algorithm.

### 2.2.3 The Velocity Verlet Algorithm

This method is a better implementation of the more general Verlet algorithm [77]. The positions, velocities and accelerations at time  $t + \delta t$  are calculated in the following way:

$$\mathbf{r}(t + \delta t) = \mathbf{r}(t) + \delta t \mathbf{v}(t) + \frac{1}{2} \delta t^2 \mathbf{a}(t) \quad \text{Eq. 2-11}$$

$$\mathbf{v}\left(t + \frac{1}{2} \delta t\right) = \mathbf{v}(t) + \frac{1}{2} \delta t \mathbf{a}(t) \quad \text{Eq. 2-12}$$

$$\mathbf{a}(t + \delta t) = -\left(\frac{1}{m}\right) \nabla V \mathbf{r}(t + \delta t) \quad \text{Eq. 2-13}$$

$$\mathbf{v}(t + \delta t) = \mathbf{v}\left(t + \frac{1}{2} \delta t\right) + \frac{1}{2} \delta t \mathbf{a}(t + \delta t). \quad \text{Eq. 2-14}$$

Where  $m$  is the mass of the atom (s) and  $\nabla V \mathbf{r}(t)$  is the total force acting on the atom at time  $t$ , represented as a function of position.

## 2.3 Statistical Ensembles

### 2.3.1 Statistical Mechanics

Statistical mechanics studies macroscopic systems from the microscopic or molecular point of view. The goal of statistical mechanics is to understand and predict macroscopic phenomena and to calculate macroscopic properties from the properties of the individual molecules making up the system [2, 78]. Molecular dynamics simulations generate information at the microscopic level, including atomic positions and velocities. Statistical mechanics is used as a tool to convert this microscopic information to macroscopic observables—thermodynamic properties—such as pressure, energy, heat capacities, and so on [78].

Statistical mechanics usually deals with the physical properties of systems of various gases, liquids, and solids in their various forms, liquid crystals and biological systems which consist of a large number of particles [79-81]. In order to deal with this problem of modeling very large systems, Gibbs first introduced the concept of ensembles

[78]. Where an ensemble is simply a collection of systems (a large number of copies of the system of interest, each prepared in an identical way) put together [82].

Statistical ensembles consider a large number of systems,  $A$ , which are each replicas on a thermodynamics (macroscopic) level of a particular thermodynamic system. Thus, if for instance a system has an isolated system with fixed volume  $V$ , contains  $N$  molecules of a single component, and is known to have energy  $E$ . Then the ensemble would have a volume  $AV$ , contain  $AN$  molecules and have a total energy  $E = AE$  [78].

### **2.3.2 Microcanonical Ensemble (NVE)**

This ensemble is a collection of many systems all with the same volume  $V$ , number of particles  $N$ , and each with the same energy  $E$  [78, 82]. There is a major disadvantage of the microcanonical ensemble since conditions of constant total energy are not those under which experiments are performed. It is, therefore, important to develop ensembles that have different sets of thermodynamic control variables in order to reflect more common experimental setups.

### **2.3.3 Canonical Ensemble (NVT)**

The most commonly used ensemble in statistical mechanics is the canonical ensemble, this ensemble is a collection of many systems all with the same volume  $V$ , number of particles  $N$  and are all connected to the same heat bath (hence each system in the ensemble has the same temperature  $T$ ) [78, 82]. Each system is enclosed in a container of volume  $V$  with heat conducting walls that are impermeable to the passage of molecules [78]. The entire ensemble is placed in a heat bath at temperature  $T$  until equilibrium is reached, and then is isolated from the surroundings. Many of the systems explored in this dissertation were simulated in the  $NVT$  ensemble.

### 2.3.4 Isothermal Isobaric Ensemble (NpT)

This is an ensemble of systems in which the containing walls of each system are heat conducting and flexible, so that each system of the ensemble is described by  $N$ ,  $T$ ,  $p$ . This ensemble plays an important role in chemistry, as chemical reactions in the laboratory usually have experimental conditions which include a fixed pressure  $P$ , temperature  $T$ , and number of atoms  $N$  which can be closely mimicked by the  $NpT$  ensemble [83]. Like the  $NVT$  ensemble, many of the required simulations for the studies documented in this dissertation are conducted using  $NpT$  ensemble conditions.

### 2.3.5 Thermostats and Barostats

The canonical and isothermal-isobaric ensembles are the most commonly used ensemble in molecular dynamics simulations. Particles in the canonical ensemble are required to interact with a thermostat to maintain the required temperature. Likewise, particles in the isothermal-isobaric ensemble are required to interact with a thermostat and barostat in order to maintain constant temperature and pressure respectively. The thermostats and barostats utilized in the molecular dynamics simulations that will be described in the following chapters of this dissertation are:

- *The Berendsen Thermostat.* There are essentially three ways to control the temperature during a molecular dynamics simulation. These include, (1) scaling the velocities, (2) adding stochastic forces and/ or velocities, and (3) using the “extended Lagrangian” formulations. In this dissertation work, the Berendsen thermostat, a velocity scaling method of temperature control is utilized [84]. This thermostat utilizes an algorithm which re-

scales the velocities of the particles involved in the molecular dynamics simulations in order to control the simulation temperature.

- *The Berendsen Barostat.* Similar to the thermostats, there are different classes of pressure control for molecular dynamics simulations. The Berendsen method is considered the length-scaling technique.

To maintain the temperature during simulations, the system is coupled to an external heat bath with fixed Temperature  $T_0$ . The velocities are scaled at each step, such that the rate of change of temperature is proportional to the difference in temperature:

$$\frac{dT(t)}{dt} = \frac{1}{\tau} (T_0 - T(t)), \quad \text{Eq. 2-15}$$

where  $\tau$  is the coupling parameter which determines how tightly the bath and the system are coupled together. This method gives an exponential decay of the system towards the desired temperature. The change in temperature between successive time steps is:

$$\Delta T = \frac{\delta t}{\tau} (T_0 - T(t)). \quad \text{Eq. 2-16}$$

Thus, the scaling factor for the velocities is

$$\lambda = \left[ 1 + \frac{\delta t}{\tau} \left( \frac{T_0}{T(t - \frac{\delta t}{2})} - 1 \right) \right]^{\frac{1}{2}}. \quad \text{Eq. 2-17}$$

In practice,  $\tau$  is used as an empirical parameter to adjust the strength of the coupling and its value needs to be chosen carefully. The large the  $\tau$  the weaker the coupling and the longer it takes for the system to achieve the temperature  $T_0$ . On the other hand, too small values of  $\tau$  will result in unrealistically low temperature fluctuations. In the length-scaling technique used by the Berendsen barostat, the system is weakly

coupled to an external system. An extra term is added to the equations of motion that affect the pressure change:

$$\frac{dP(t)}{dt} = \frac{1}{\tau_p} (P_0 - P(t)), \quad \text{Eq. 2-18}$$

where  $\tau_p$  is the time constant for the coupling and  $P_0$  is the desired pressure. The system pressure is set toward a desired value by changing the dimensions of the simulation cell size during the simulation. The scaling factor (for each dimension) is

$$\mu = \left[ 1 - \frac{\beta \delta t}{\tau_p} (P_0 - P(t)) \right]^{\frac{1}{3}}, \quad \text{Eq. 2-19}$$

where  $\beta$  is the isothermal compressibility of the system [84].

Length scaling at each time step using a global scale factor can lead to violent oscillations of pressure in more ordered systems, and is therefore not usually recommended for production molecular dynamics runs.

## 2.4 Thermodynamics Properties

A wide variety of thermodynamic properties can be calculated from computer simulations. A comparison of experimental and calculated values for such properties is an important way in which the accuracy of the simulation and the underlying energy model can be quantified. Simulation methods also enable predictions to be made of the thermodynamics properties of systems for which there is no experimental data, or for which experimental data is difficult or impossible to obtain [2]. Some of the main thermodynamic properties which are routinely calculated in computer simulations include, energy, heat capacity, pressure, temperature (in the canonical ensemble, this property is some chosen constant value) and radial distribution function. The radial distribution function is one of the main thermodynamic properties that are exploited as a

means of gaining insight about the interaction of molecules in the systems that are studied and reported in subsequent chapters of this dissertation. The radial distribution function will be presented in detail here while other thermodynamic properties will be presented in related chapters.

## 2.5 Radial Distribution Function (RDF)

The radial distribution function (commonly referred to as the paired correlation function) is a useful way to describe the structure of a system, especially in the case of liquid systems like the ones detail in this dissertation. This function is commonly denoted by  $g(r)$  and can be expressed by the equation

$$g(r) = 4\pi r^2 \rho(r), \quad \text{Eq. 2-20}$$

where  $\rho(r)$  is the local number density of atoms at a distance  $r$  from an atom, average with respect to the choice of the atom [85].

The RDF provides a direct physical picture of the spatially averaged structure, although it is merely a one-dimensional representation. The area under the first peak,

$$\int g(r) dr = \int 4\pi r^2 \rho(r) dr = Z, \quad \text{Eq. 2-21}$$

is the first coordination shell surrounding an average atom, assuming no overlap of the second peak. Beyond the first peak which defines the mean nearest neighbor distance and mean coordination number, and the second peak which defines the root mean square (rms) angular deviation, nothing more can be learned reliably from the RDF [85].

If for instance, we have a spherical shell of thickness  $\delta r$  at a distance  $r$  from the chosen atom as shown in Figure 2-1,

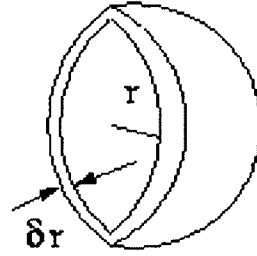


**Figure 2-1:** Showing the spherical shell of thickness  $\delta r$  used to calculate the radial distribution function

and the volume of the shell is given by:

$$V = \frac{4}{3}\pi(r + \delta r)^3 - \frac{4}{3}\pi r^3 \quad \text{Eq. 2-22}$$

$$V = 4\pi r^2 \delta r + 4\pi r \delta r^2 + \frac{4}{3}\pi \delta r^3 \approx 4\pi r^2 \delta r. \quad \text{Eq. 2-23}$$

If the number of particles per unit volume is  $\rho$ , then the total number in the shell is  $4\pi\rho r^2\delta r$  and so the number of atoms in the volume element varies as  $r^2$ . The pair distribution function,  $g(r)$ , gives the probability of finding an atom a distance  $r$  from another atom compared to the probability expected from a completely random distribution at the same density [2, 86]. References to the ‘radial distribution function’ usually refers to the pairwise function, higher orders can be defined but are not usually calculated. The radial distribution function of liquids usually has a small number of peaks at shorter distances and has a steady decay towards a constant value at longer distances.

Figure 2-2 shows the radial distribution function calculated from a molecular dynamics simulation of an aqueous solution.

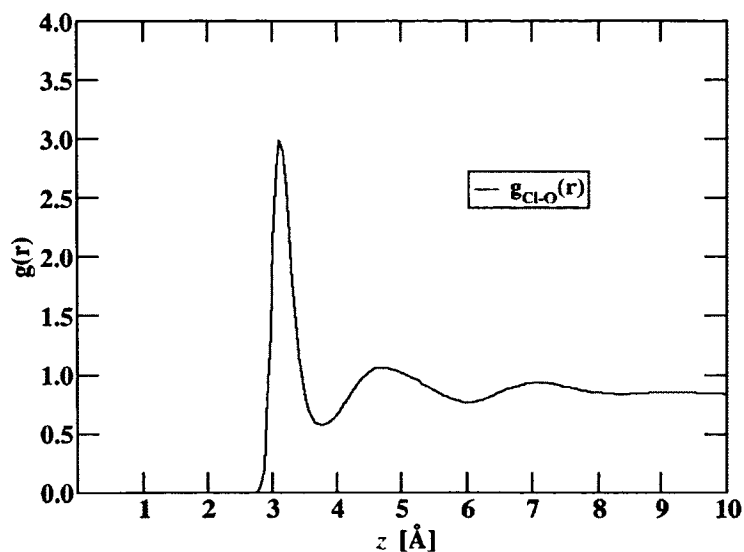


**Figure 2-2:** Radial distribution function determined from molecular dynamics simulation of an aqueous 1M NaCl solution at 298K. The RDF is between the water oxygen and the chloride ion in the NaCl.

For short distances (less than the atomic diameter)  $g(r)$  is zero, this is due to the strong repulsive forces. The first and the largest peak occurs at approximately  $3.2\text{\AA}$  with  $g(r)$  having a value of about 3. This means that it is three more times likely that these two atoms would have this separation than in the ideal gas. The radial distribution function then falls and passes through a minimum at around  $3.8\text{\AA}$ , the chances of finding two atoms with this separation are less than for an ideal gas. At long distances  $g(r)$  tends to the ideal gas value,  $g(r) = 1$ , indicating that there is no long-range order [2].

The RDF is also commonly defined as:

$$g(r) = \frac{N(r)}{4\pi r^2 \rho \delta r}, \quad \text{Eq. 2-24}$$

where  $N(r)$  is the number of atoms in the shell between  $r$  and  $r + \delta r$  around the central atoms and  $\rho$  is the number density of atoms, taken as a ratio of the number of atoms to the

volume of the simulation cell [87], and  $4\pi\rho r^2\delta r$  represents the total number of particles in an ideal gas system [88].

Each peak in the RDF can be identified as the coordination shells for the atoms or molecules. By integrating the RDF under the peak one can obtain the total of bonds between the atoms or molecules of interest [87]. This is what we often refer to as the coordination number. According to RDF, the number of atoms in the first coordination shell, called the coordination number ( $CN$ ), is obtained by taking the integral from the separation distance at which the RDF first increases from zero to the first minimum in  $g(r)$  designated as  $r_{min}$  and shown in Eq. 2-25 [88]

$$CN = \int_0^{r_{min}} 4\pi\rho g(r)r^2 dr = Z. \quad \text{Eq. 2-25}$$

## 2.6 Force Fields

In molecular dynamics a molecule is described as a series of charged points (atoms) linked together by springs (bonds). A force field is used to accurately describe the time evolution of bond lengths, bond angles and torsions, as well as non-bonding—van der Waals and electrostatic—interactions [2]. The force field can be briefly explained as a collection of equations and associated constants designed to reproduce molecular geometry and selected properties of tested structures from both experimental work and quantum mechanical calculations in high level. As such, a force field can be simply described as a mathematical function that describes how atoms/molecules move, stretch, vibrate, rotate and interact with each other [2]. In the force field function, the presence of electrons is generally ignored.

A general form, like the one presented in Eq. 2-26 is used to represent the total energy in a force field,

$$E(r^N) = E_{bond} + E_{angle} + E_{dihedral} + E_{Van\ der\ Waals} + E_{electrostatics}, \quad \text{Eq. 2-26}$$

where  $r^N$  represents the positions of N particles,  $E(r^N)$  indicates the potential energy, it is a function of the positions ( $r$ ) of N particles (usually atoms). The bonded interactions are:  $E_{bond}$  which accounts for the energy associated with bond stretching,  $E_{angle}$  which accounts for the energy associated with bond angle bending, and  $E_{dihedral}$  which accounts for the torsion which is the energy needed to rotate about the bonds. The non-bonded interactions  $E_{Van\ der\ Waals}$  and  $E_{electrostatics}$  account for the energy due to the interactions (attraction or repulsion) between the dipoles and the energy due to interactions between charged atoms respectively [2].

More complicated force fields also contain other terms like out-of-plane bending and cross terms. Out-of-plane bending describes improper torsions and is usually added to the force field to explain the torsion where the angles are not bonded in sequences and cross terms describe coupled motion such as bond stretching-angle bending [2]. Some force fields even take into account solvation and polarization effects

The AMBER (Assisted Model Building and Energy Refinement) force field, which is a family of different variations of a general force field form, was used for this work. The specific forms or modifications adapted will be detailed in the related sections. AMBER force fields consist of more complex force fields forms that can account for solvation and polarization effects.

The functional form of the AMBER force field family is:

$$\begin{aligned}
 E(r^N) = & \sum_{bonds} k_b(l - l_0)^2 + \sum_{angles} k_a(\theta - \theta_0)^2 \\
 & + \sum_{torsions} \frac{1}{2} E_n [1 + \cos(n\omega - \gamma)] \\
 & + \sum_{j=1}^{N-1} \sum_{i=j+1}^N \left\{ \epsilon_{ij} \left[ \left( \frac{r_{0ij}}{r_{ij}} \right)^{12} - 2 \left( \frac{r_{0ij}}{r_{ij}} \right)^6 \right] + \frac{q_i q_j}{4\pi\epsilon_0 r_{ij}} \right\}.
 \end{aligned}
 \tag{Eq. 2-27}$$

Different members of the AMBER force field family which are recognized by different names have different values for the parameters present in Eq. 2-27 [89]. Paralleled to the general form in Eq. 2-26, the first and second terms represent the energy between covalently bonded atoms and the energy due to the geometry of the electron orbitals involved in the covalent bonds respectively. Where  $k_a$  and  $k_b$  are the force constants,  $l_0$  is the equilibrium bond length and  $\theta_0$  is the equilibrium bond angle. The third term represents the energy for twisting a bond due to bond order and neighboring bonds or lone pairs of electrons. These first three terms account for the bonded interactions. The non-bonded interactions are accounted for in the fourth term in Eq. 2-27, which represents both van der Waals and electrostatic energies. The third and fourth terms are expressed differently depending on the specific AMBER force field form used, for which details presented in related sections.

### 2.6.1 Lennard-Jones Potential

As aforementioned, the Lennard-Jones potential can be used to model van der Waals interactions in the model utilizing simple force fields. The best known of the van der Waals potential functions is the “Lennard-Jones 12-6 function” which can be

represented using the following formula, and represents the interaction between two atoms [2]

$$E_{Van\ der\ Waals} = v(r) = 4\varepsilon \left[ \left( \frac{\sigma}{r} \right)^{12} - \left( \frac{\sigma}{r} \right)^6 \right]. \quad \text{Eq. 2-28}$$

The Lennard-Jones potential is characterized by an attractive part that varies as  $r^{-6}$  and the repulsive part that varies as  $r^{-12}$ . This Lennard-Jones parameter contains two adjustable parameters,  $\sigma$  which is referred to as the collision diameter (the separation between the atoms which results in zero energy) and  $\varepsilon$  which is referred to as the well depth.

For the flexible water model used for some of the molecular dynamics studies in this dissertation, the Van der Waals interactions were described with the exponential-6 (exp-6) interaction potential which takes the form

$$E_{Van\ der\ Waals} = \varepsilon \left[ \frac{6}{\lambda} \exp \left( \lambda \left[ 1 - \frac{r}{\sigma} \right] \right) - \left( \frac{r}{\sigma} \right)^6 \right], \quad \text{Eq. 2-29}$$

where  $\lambda=13.5$  for all interactions, while a different  $\sigma$  and  $\varepsilon$  value are used depending on the interaction type (ions-involved in the interaction). The values for  $\sigma$  and  $\varepsilon$  are included in related chapters.

### 2.6.2 Coulomb Potential

In a simple force field the non-bonded term can be modeled using the Coulomb potential term for the electrostatics and the Lennard-Jones Potentials for the van der Waals interactions. Elements attract electrons (with electronegative elements attracting more charge than less electronegative elements) to themselves which gives rise to an unequal distribution of charge in a molecules [2]. One common way of representing this charge distribution in an arrangement of fractional point charges throughout the

molecule. These charges are designed to reproduce the electrostatic properties of the molecule. The electrostatic interaction between two molecules (or between different parts of the same molecule) is calculated as a sum of interaction between pairs of point charges using Coulomb's law and is written as:

$$E_{electrostatics} = V = \sum_{i=1}^{N_A} \sum_{j=1}^{N_B} \frac{q_i q_j}{4\pi\epsilon_0 r_{ij}}, \quad \text{Eq. 2-30}$$

where  $N_A$  and  $N_B$  are the numbers of point charges in the two molecules.

### 2.6.3 Polarizable Interactions and Polarizability

Simple water models (described in appendix A) give very good results for a wide range of properties of pure liquid water [2]. However, these simple models are not always sufficient. As a matter of fact, when ions are present the inclusion of polarizability presents a more accurate picture of the solvent-water interactions [11, 24-26]. Essentially, polarizability is the ability of a molecules, atoms or ions to acquire a dipole moment in the presence of an electric field [90]. In the polarizable models used in the studies in this dissertation, the total electrostatic potential of the systems are written as:

$$\mathbf{E}_{electrostatic} = \sum_{i<j} \left[ \frac{q_i q_j f_0(r_{ij})}{4\pi\epsilon_0} \right] - \frac{1}{2} \sum_i \vec{\mu}_i \mathbf{E}_i^0. \quad \text{Eq. 2-31}$$

Where  $i$  and  $j$  includes the summation over all atoms,  $q_i$  represents the atomic charges,  $\mu_i$  is the dipole of atom  $i$ , and  $\mathbf{E}_i^0$  is the static electric field.

$$\overline{\mu}_i = \alpha_i \mathbf{E}_i, \quad \text{Eq. 2-32}$$

where Eq. 2-32 gives the relationship between the magnitude of the induced dipole moment  $\overline{\mu}_i$ , the electric field  $\mathbf{E}_i$ , and the polarizability  $\alpha_i$  (which is the proportionality constant) of site  $i$ . Furthermore,

$$\mathbf{E}_i = \mathbf{E}_i^0 + \sum_{j \neq i} \mathbf{T}_{ij} \overline{\mu}_j \quad \text{Eq. 2-33}$$

$$\mathbf{T}_{ij} = \frac{1}{r_{ij}^3} \left( f_2(r_{ij}) \frac{3\overline{r}_{ij}\overline{r}_{ij}}{r_{ij}^2} - f_1(r_{ij}) \right) \quad \mathbf{E}_i^0 = \sum_{j \neq i} f_1(r_{ij}) \frac{q_j \overline{r}_{ij}}{r_{ij}^3}. \quad \text{Eq. 2-34}$$

The functions,  $f_i(r_{ij})$  are the damping potentials, which are defined for specific systems in related chapters throughout the dissertation. Polarizability enhances interfacial concentration due to the fact that it allows induced dipoles to form on anions, which are more stable at the air-water interfaces than in the bulk, providing an additional driving force to the air-water interface [69, 91-92]. Polarizable interactions are considered for all the molecular dynamics simulations described in this dissertation.

#### 2.6.4 Always Stable Predictor Corrector (ASPC) Method

In order to handle polarizable interactions in our MD simulations we use the always stable predictor corrector (ASPC) method. Typically, in many MD simulations the self-consistent field (SCF) method is used to handle these polarizable interactions. The SCF method can essentially be *simplified* as an iterative method used to evaluate a property of interest where the stopping conditions for the iteration is self consistency (minor difference between two consecutive iterations). Dang and Chang adapted the SCF method for the induced dipoles in MD simulations using the water model briefly

described in Section A.2 [70]. At each time step, the electric field is computed at a site  $i$ , produced by fixed charges in the system. Then the calculated electric field is used to generate the initial estimate of the induced dipole moments. Both the initial estimates of the induced dipole and the calculated electric field are used to compute the total electric field. These steps are repeated until the difference between the induced dipole of two successive iterations are less than some predetermined tolerance value (approximately  $10^{-5}$  Debye) [70].

These iterations associated with the SCF method can be avoided by using the always stable predictor-corrector (ASPC) method which consists of a predictor and corrector. The predictor is used to predict the electrostatic field on the basis of knowledge from previous steps [93]. The corrector requires one evaluation (only one iteration is required) of induced dipoles per integration step. The corrector is damped by using a relaxation parameter. Specific values of the dampening parameter guarantees stability of the ASPC method; this means that errors are not accumulated as the predictor-corrector steps are repeated.

## CHAPTER 3

# INFLUENCE OF THE COUNTERION ON ANION PROPENSITY FOR THE AIR/WATER INTERFACE

### 3.1 Introduction

As mentioned and described in more detail in Chapter 1, many physical, chemical, atmospheric, and biological processes can benefit from a thorough understanding of the behavior of ions at aqueous interfaces. Factors such as interfacial tension, reactivity of the water surface, and the best method of extracting ions from an aqueous mixture are all factors that can be influenced by the behavior of ions near the interface [9, 22-23]. Previous studies have also established that the distribution of ions can affect the structure and stability of proteins and membranes [10-12]. In the study detailed in this chapter we intend to bring greater insight into many of these areas of study. For instance, if we can establish that an ion has a propensity for the interface, its extraction at the interface would probably happen more readily than otherwise.

Previous studies have also shown that chloride alone had no propensity for the air/water interface [25], while concentrated solutions of sodium chloride using similar models have found that chloride has a propensity for the air/water interface [33-34]. Furthermore, divalent cations are found to significantly enhance this effect [35]. As

aforementioned, this led us to believe that the cation, even if it does not have a propensity for the interface itself, plays a major role in the distribution of ions at the air/water interface.

This study was carried out to investigate the influence of ion pairing on anion propensity for the air/water interface of water. The study was conducted using molecular dynamics simulations with polarizable interactions. Figure 3-1 provides a picture of the molecules interacting in the NaCl systems described in this chapter.

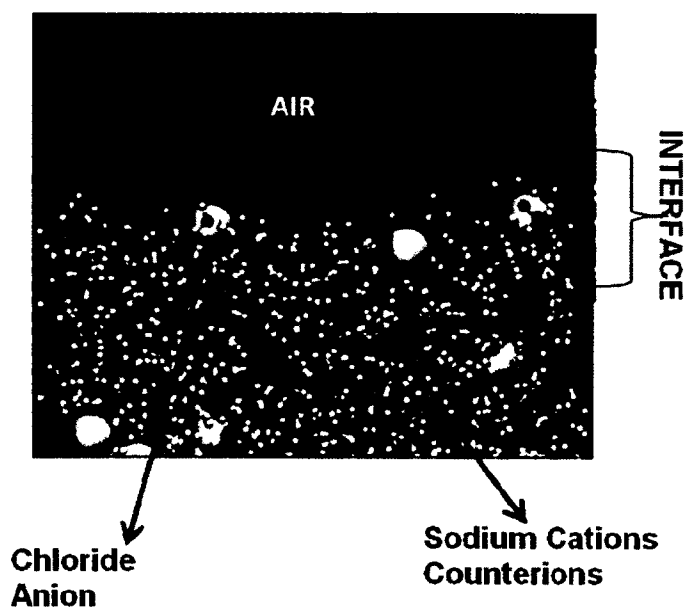


**Figure 3-1:** Showing a snapshot of the air/water interface with NaCl ions

In the aqueous NaCl solution pictured in Figure 3-1, the blue and white molecules represent the liquid water molecules. The yellow atoms represent chloride anions and the green atoms represent the sodium cations which are referred to as the counterions. In this study, the charges on the sodium counterions were varied and included 0.8, 1.0, and 1.2 electron charges. This was done to observe the effect of the varied sodium charges on the chloride anion. Also, the interaction strength between the ions was dampened to test its

effect on the interaction of the ions and propensity for the interface. Additionally, the bond distance between the sodium and chloride ions was varied to investigate the effect of counterion-anion proximity on propensity of the ions for the interface.

## 3.2 Simulation Details

Classical molecular dynamics (MD) simulations were carried out in the NVT ensemble at 298K, with the temperature controlled by the Berendsen thermostat [84]. The Dang-Chang water model was used [70, 94], which has four sites, including a single Lennard-Jones site at the oxygen atomic position, partial positive charges at the hydrogen atomic positions, and both a negative partial charge and point polarizability located at an *m*-site, which is along the bisector of the oxygen-hydrogen bonds. Previously developed polarizable potentials were also used for sodium and chloride [25]. All molecular geometries were kept fixed with the SHAKE and RATTLE algorithms [95]. A Lennard-Jones potential truncation of 9 Å was enforced with analytical tail corrections employed. Long-ranged electrostatics were handled with the particle mesh Ewald summation technique [96].

### 3.2.1 Concentrated Systems

For these systems, 2669 water molecules were placed in a rectangular box of dimensions  $84 \times 44 \times 44$  Å, in which approximately half of the box was occupied with liquid, and the other half with vapor. As a result, two air/water interfaces form bisecting the *z*-axis. Four systems were simulated in this study, which included a number of sodium and chloride ions in addition to the water molecules described. The four systems include ones with a sodium electron charge of 0.8 (Na 0.8), 1.0 (Na 1.0), and 1.2 (Na 1.2). The number of ions was adjusted such that the total system charge was neutral. For

the Na 0.8 charged system, there were 48 sodium and 40 chloride ions, for the Na 1.0 system, there were 48 of both ions, and for the Na 1.2 system, there were 38 sodium and 48 chloride ions. It should be noted that previous work on the concentration dependence of NaCl interfacial distributions found no significant difference in relative interfacial concentration between 1M and 3M systems [97], so the small differences in ion concentrations should not be a factor here. The fourth system (Na 1.0\_damp) had a sodium charge of 1.0, but the electrostatic interactions between NaCl were dampened at short range with a Thole-type damping interaction [98-99]. The total electrostatic interaction a system is given as,

$$E_{ij}^{elec} = \sum_{i<j} \frac{q_i q_j f_0(r_{ij})}{4\pi\epsilon_0} - \frac{1}{2} \sum_i \bar{\mu}_i E_i^0 \quad \text{Eq. 3-1}$$

which is described in detail earlier in Section 2.6.3. The dampening potentials which are the functions  $f_i(r_{ij})$  are presented in Section 2.6.3 are 1.0 for all interactions except between ions in the Na 1.0\_damp system, and only significantly deviate from 1 when the interatomic distance is less than 5 Å. The values for these are given as,

$$f_0(r_{ij}) = \frac{1 - \exp[-0.2(r_{ij}/A)^3] + 0.2^{1/3}(r_{ij}/A)\Gamma(2/3)Q[2/3, 0.2(r_{ij}/A)^3]}{r_{ij}} \quad \text{Eq. 3-2}$$

$$f_1(r_{ij}) = 1 - \exp[-0.2(r_{ij}/A)^3] \quad \text{Eq. 3-3}$$

$$f_2(r_{ij}) = 1 - [1 + 0.2(r_{ij}/A)^3] \exp[-0.3(r_{ij}/A)^3], \quad \text{Eq. 3-4}$$

where  $\Gamma(2/3)$  is the gamma function, and  $Q$  represents the incomplete gamma function, which can be calculated from *Numerical Recipes* [100]. Again, all of these functions are 1 except between NaCl in the Na 1.0\_damp system, and the value for  $A$  for these systems

was set to 1.02 Å. All properties were calculated from 6 ns simulations, following extensive equilibration.

### 3.2.2 Single Ion Pairs

We calculated the potential of mean force (PMF) as a function of  $z$ -position with respect to the Gibbs dividing surface (GDS) of the air/water interface. For these simulations, we had a total of 550 water molecules, and either a single ion (in the case of chloride) or a pair of NaCl with different cation charges. We used umbrella sampling to carry out the calculation [101], in which the  $z$  position of either chloride itself or the center of mass between NaCl had a harmonic biasing potential coupled to it with respect to the water center of mass.

$$U = k_z (z_x - z_0)^2, \quad \text{Eq. 3-5}$$

where  $z_x$  represents the distance between the ion or ion pair center of mass with water center of mass. The value of  $k_z$  was set to 2.0 kcal/mol, and multiple values of  $z_0$  were used. For all systems, the  $z_0$  values were spaced in 1.0 Å increments, covering a range from near the GDS until far enough into the bulk such that the free energy profile flattens out. For the systems with NaCl pairs, a second harmonic umbrella,

$$U = k_r (r_{\text{NaCl}} - r_0)^2 \quad \text{Eq. 3-6}$$

where  $r_{\text{NaCl}}$  corresponds to the NaCl interatomic distance, and  $k_r$  was set to 5.0 kcal/mol. Two different scenarios were investigated for the NaCl pairs, one with  $r_0=2.25$  Å, corresponding with the contact ion pair (CIP), and the other with  $r_0=4.5$  Å, corresponding with the solvent separated ion pair (SSIP), which have been defined in previous work in the bulk [102], and at the air/water interface [13, 103]. As stated earlier, multiple simulations were carried out for each system, each with a different  $z_0$  value spaced in 1.0

Å increments. For each simulation, a weighted (to remove the contribution from the umbrella biasing potential [101]) PMF was calculated, and in regions of overlap, they were matched to create a single PMF. A total of 10 ns for each  $z_0$  position was carried out following 1ns of equilibration.

### 3.3 Results and Discussions

#### 3.3.1 Density Profiles

Figure 3-2 shows the density profiles for sodium and chloride ions for the Na 0.8, Na 1.0, Na 1.2, and Na 1.0\_damp systems with respect to the GDS. The integrated densities for each ion were set to be equal.

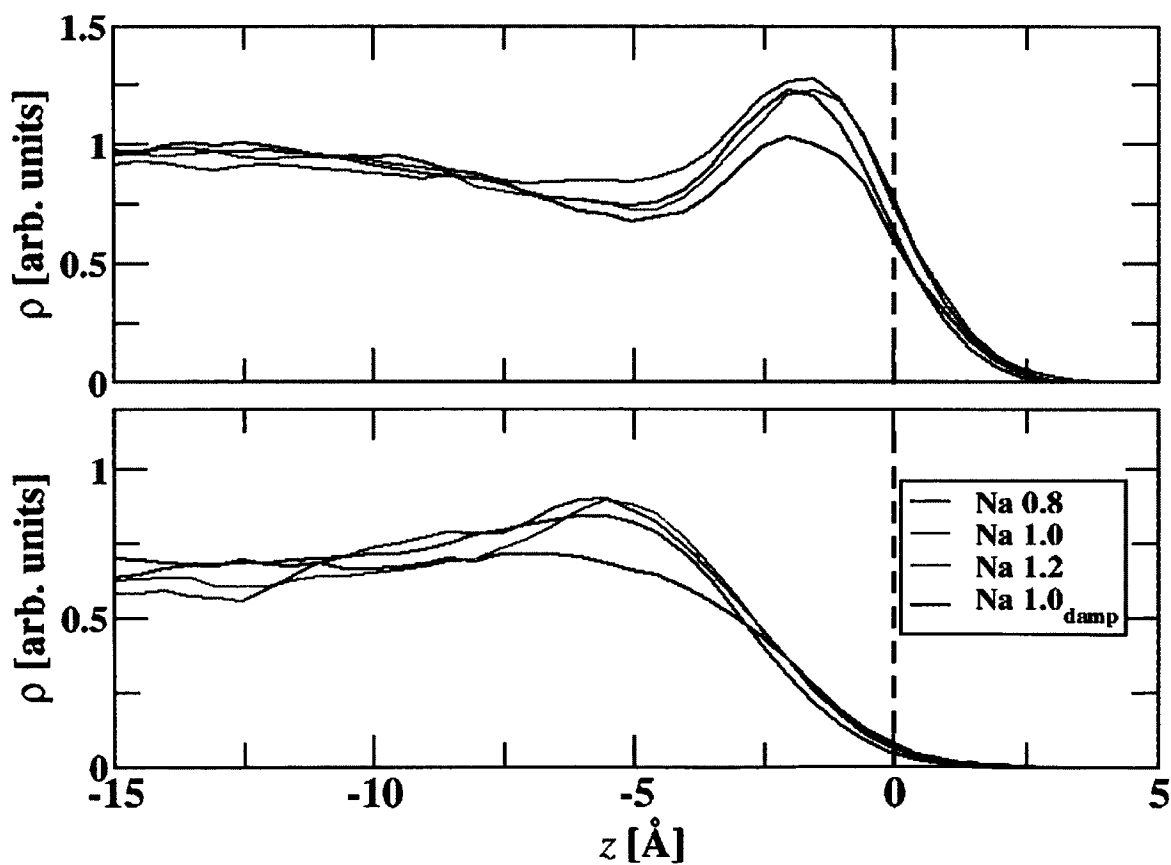


**Figure 3-2:** Density profiles of sodium (bottom) and chloride (top) ions as a function of distance from the GDS.

In Figure 3-2 there is a trend showing more highly charged cations leading to greater ion interfacial density. The difference is much more noticeable between the Na 0.8 and Na 1.0 systems, with only a small difference between the Na 1.0 and Na 1.2 systems. In fact, it can be seen that only for the Na 0.8 system, that the density profile of sodium shows no enhancement near the interface, but monotonically drops towards zero. Damping the interactions between sodium and chloride has a minor effect on the interfacial ion distributions. For the Na 1.0\_damp system, the chloride interfacial density is similar to the Na 1.0 system, but shifted towards the bulk, while there is a small reduction in cation density 5 Å from the GDS.

### **3.3.2 Radial Distribution Functions (RDFs)**

The effect of counterion on anion interfacial behavior is likely due to two effects: the cation-anion interaction strength and the effect of the cation charge itself on interfacial electrostatic properties. To further investigate the former, the NaCl interatomic radial distribution functions (RDFs) were calculated for the different systems, and the results are given in Figure 3-3.

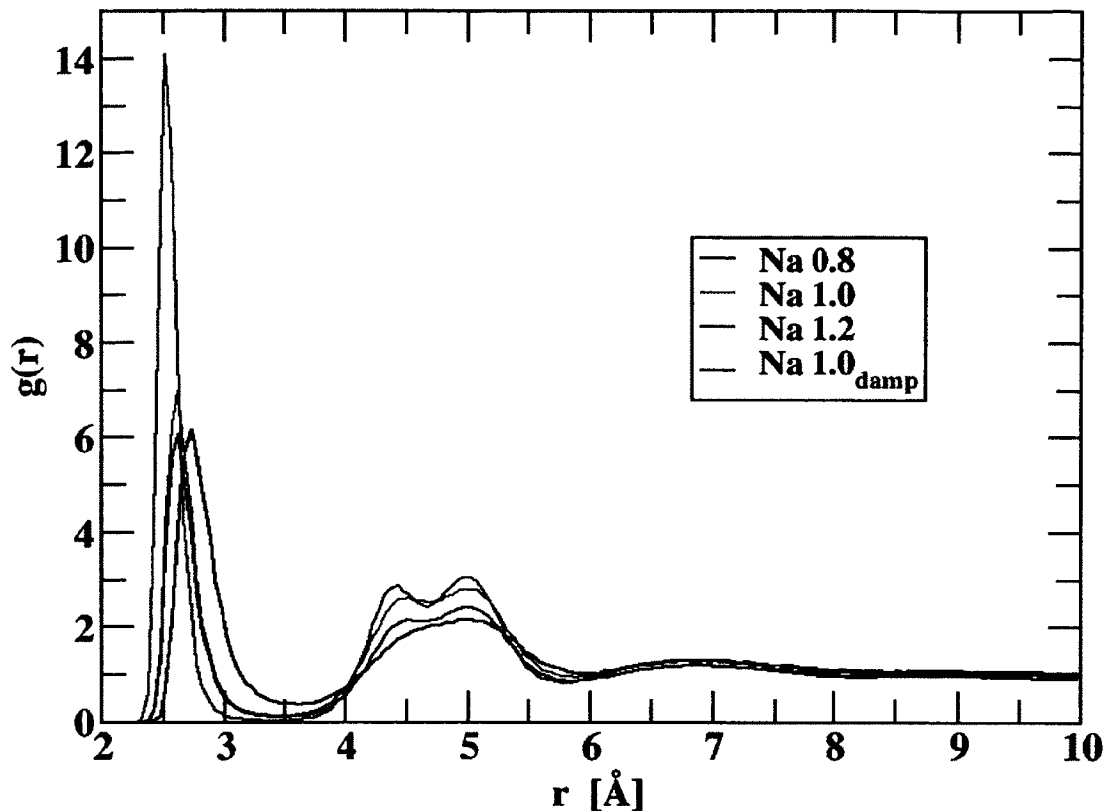


**Figure 3-3:** Sodium-chloride RDFs for the systems investigated

From Figure 3-3, it is evident that higher cation charge causes the ions to interact more strongly with one another, showing a much stronger first RDF peak. The Na 1.0\_damp system has a similar first RDF peak height as the Na 0.8 system, which is lower than the Na 1.0 system. It is interesting to note that higher cation charge also shifts the RDF peak to shorter distances, but damping the NaCl interactions has little effect on the peak position. Moreover, the RDF well between the first and second peaks is lower, and the second RDF peak is higher with higher cation charge, showing greater overall structure. After the second RDF peak, the RDFs all appear to approach one another. In addition to NaCl interactions, cation charge should have an effect on cation-water interactions. Figure 3-4 gives the sodium-oxygen RDFs for the systems investigated.

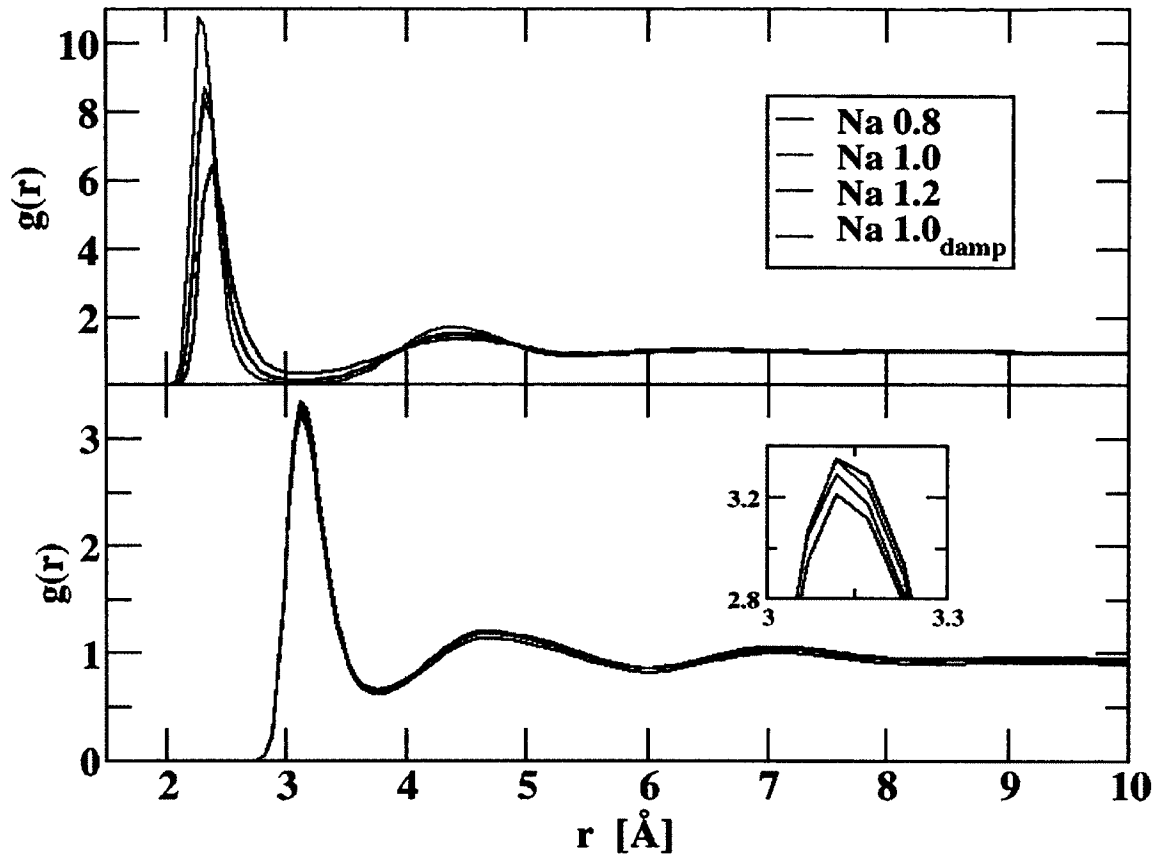


**Figure 3-4:** Sodium-oxygen (top) and chloride-oxygen (bottom) RDFs. The insets showed a closeup of the first peak of the Cl-O RDF.

Higher cation charge clearly causes stronger sodium-oxygen binding, as it increases the first RDF peak significantly. It is interesting to note that the difference in sodium-oxygen peak height between the Na 0.8 and Na 1.0 systems is similar to the height difference between the Na 1.0 and Na 1.2 systems. This type of consistency was not observed for the NaCl RDFs. Also, as with the NaCl RDFs, the first RDF well is lower and the second RDF peak is higher for the Na 1.2 system, showing some enhanced mid-ranged ordering with higher sodium charge. The Na 1.0<sub>damp</sub> system shows a slightly smaller first RDF peak, which is somewhat unexpected, as the Na 1.0<sub>damp</sub> system would have less bonding with chloride ions. This would be expected to enhance

oxygen-chloride binding, due to competition between sodium-chloride and oxygen-chloride interactions. This suggests that anions binding with cations actually enhance cation-water binding. Figure 3-4 also gives the RDFs between chloride and oxygen for the systems investigated. These RDFs show fairly minor differences between the different systems. The first RDF peak for the Na 1.0\_damp system is slightly lower than the rest, suggesting that stronger cation-anion binding itself also enhances anion-oxygen binding, but these are too small to develop a strong basis for them.

### 3.3.3 Induced Dipole

The propensity of anions for the air/water interface has been linked to the anion induced dipole. Figure 3-5 gives the average induced dipole of chloride as a function of position with respect to the GDS.

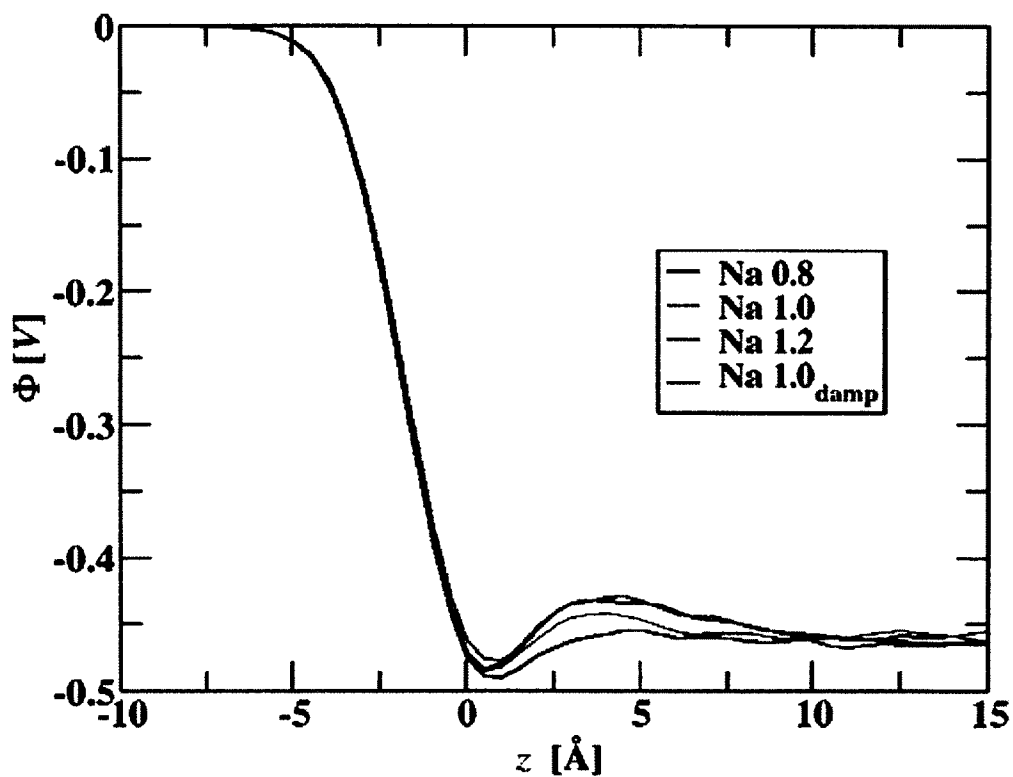


**Figure 3-5:** Average anion induced dipole as a function of position for the systems investigated.

Interestingly, in Figure 3-5 the average induced dipoles in the bulk are all very similar, but the systems with the higher cation charge have greater anion induced dipoles at the air/water interface. The higher anion induced dipoles at the air/water interface would be expected to increase their propensity for that region, which is consistent with the density profiles. The induced dipoles for the Na 1.0\_damp and Na 1.0 systems are very similar, so damping has little effect on interfacial induced dipoles. This allows a picture to be developed as follows. Cation-anion binding has a minor effect on the propensity for the air/water interface, but more highly charged cations result in anions at the air/water interface to have a higher induced dipole. These higher induced dipoles increase the anion propensity for the air/water interface.

### **3.3.4 Free Energy Profiles**

The free energy profiles for a single chloride ion and NaCl contact ions pairs (CIPs) with different cation charges were carried out across the air/water interface, and given in Figure 3-6.

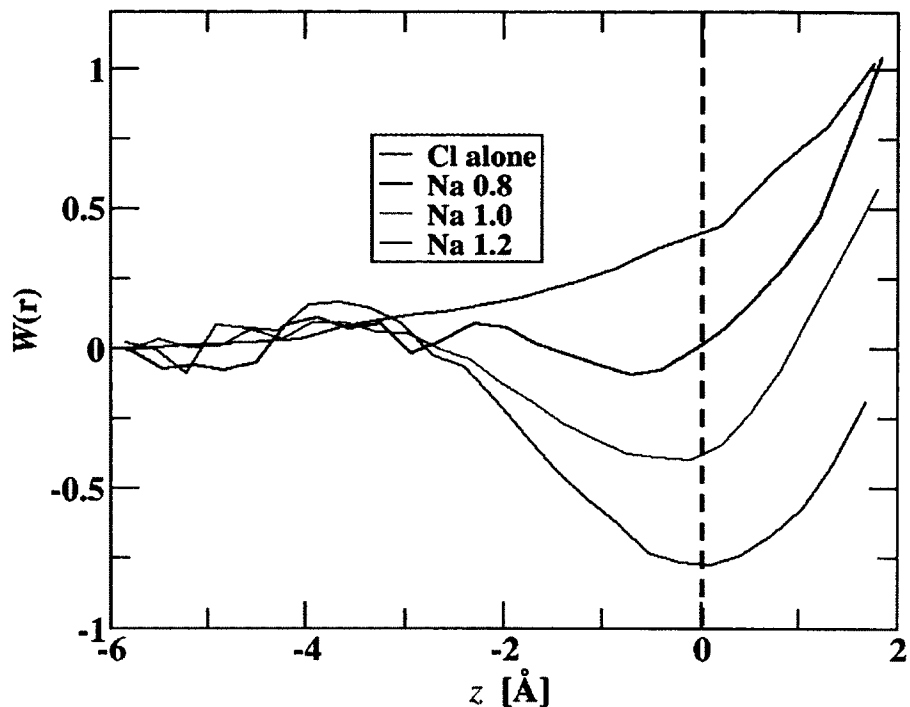


**Figure 3-6:** PMFs for a single chloride and the NaCl pair for the systems investigated with  $r_0=2.25 \text{ \AA}$ .

For the single chloride anion, its free energy is greater at the interface than in the bulk, which is consistent with previous calculations of the same system [25]. All of the NaCl pairs have a lower interfacial free energy than in the bulk. The Na 1.0 pair has an interfacial free energy minimum around  $-0.4 \text{ kcal/mol}$ , showing that NaCl ion pairing decreases the free energy. The Na 0.8 pair has a higher interfacial free energy minimum, while the Na 1.2 pair has a lower free energy. This observation is consistent with the density distributions shown in Figure 3-2, as the Na 1.2 system has the highest interfacial densities, and the Na 0.8 system has the least. Also, the induced dipoles of the anions are greater for the Na 1.2 pair, and least for the Na 0.8 pairs, but these were still higher than the induced dipole of the single chloride anion (results not shown).

One factor that may influence the interfacial behavior of an ion pair may be its orientation with respect to the air/water interface. Figure 3-7 gives the angular distribution of the cation-anion vector with the  $z$ -axis from the ion pair simulations with  $z_0$  at the GDS (or zero).

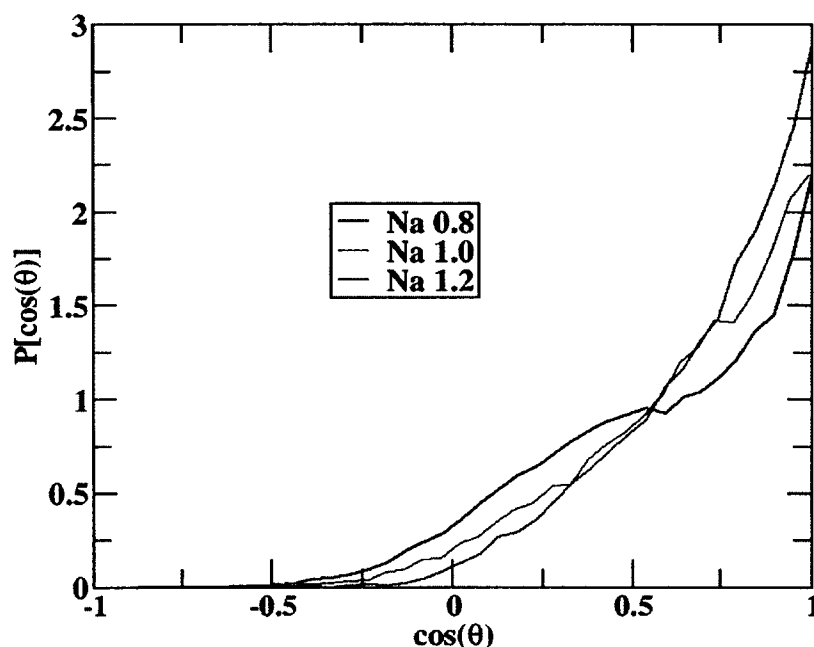


**Figure 3-7:** Angular distribution of NaCl for the different single ion systems investigated.

A  $\cos(\theta)$  value of 1 represents the ion pair perfectly aligned with the  $z$ -axis with chloride oriented towards the air. All ion pairs show strong orientational preference with chloride pointing towards the air. It is interesting to note that a similar analysis of NaOH orientation found a greater preference for the anion (in this case hydroxide) to be oriented towards the air [104]. Greater cation charge increases the orientational preference observed. This allows the following picture to be developed to explain the observed trends. Ion pairing causes a dipole that points towards the air to form, and the higher cation charge increases this dipole due to greater induction of the anion dipole. This

dipole is attracted to the air/water interface, due to attractive interactions with the electric field formed at the air/water interface, which is equivalent to a dipole pointing towards the bulk [105].

To further investigate how the cation-anion distance influences anion interfacial free energy, the free energy profile for NaCl in a (contact ion pair) CIP along in a (solvent separated ion pair) SSIP were calculated and given in Figure 3-8.

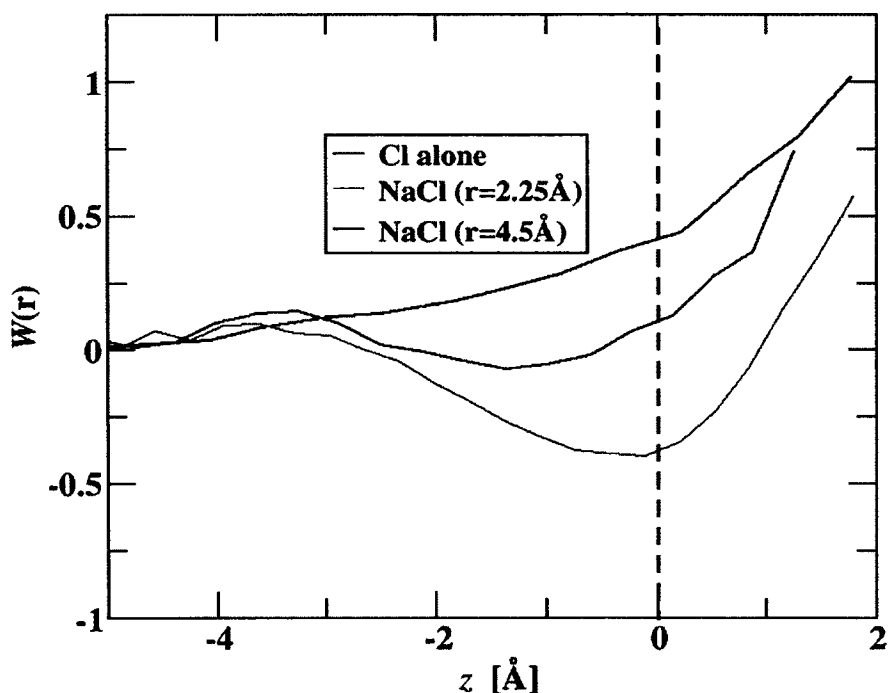


**Figure 3-8:** A comparison of the PMFs for chloride alone and for NaCl with  $r_0=2.25 \text{ \AA}$  and  $r_0=4.5 \text{ \AA}$ .

The CIP has a more negative interfacial free energy than the SSIP. Again, the average chloride induced dipole is on average larger for the CIP than for the SSIP, which is larger than for chloride alone (data not shown), which is likely the reason for the observed trends.

### 3.4 Conclusions

In the study detailed in this chapter, MD simulations were carried out to investigate how ion pairing, counterion charge, and cation-anion interaction strength influenced ion distributions at the air/water interface. The results of this work found that higher cation charge increased the propensity of anions for the air/water interface. Slightly weakening cation-anion interactions had minor effects on ion distributions at the interface, but did not significantly reduce their propensity for the interface. A single ion pair had a significantly lower interfacial free energy than the anion alone, and a CIP had a much lower free energy than a SSIP.

## CHAPTER 4

# EFFECT OF IONS ON SURFACE TENSION OF WATER WITH ELECTROSTATIC DAMPING

### 4.1 Introduction

Chapter 1 provides a more comprehensive overview of interfaces which are potential mediums for a large numbers of chemical reactions which makes it important to study the interfacial environment, including the concentration of species present there. Predicting and controlling behavior of matter at interfaces requires an understanding of what species are present at the related interfaces since these species will influence reaction conditions. The change in surface tension after the addition of solutes has been used as an indicator for solute propensity for the air-water interface [106-109]. For most inorganic salts, it has been established that their addition to water increases the surface tension of the air-water interface [110-114]. The Gibbs surface tension equation links an increase in surface tension to lower interfacial concentration with respect to the bulk, or a negative surface excess [107].

As mentioned in Chapter 1, larger, more polarizable, halide anions have a greater propensity for the air-water interface [24, 27]. Polarizability enhances interfacial concentration due to the fact that it allows induced dipoles to form on anions, which are

more stable at the air-water interfaces than in the bulk, providing an additional driving force to the air-water interface [69, 91-92]. More recently, it has been pointed out that traditional polarizable models often overestimate the induced dipole that forms on an ion in bulk water in comparison with *ab initio* molecular dynamics (AIMD) simulations [115-117]. This work suggested that including electrostatic damping, of the Thole type [98], can bring agreement with anion dipole distributions from classical MD and AIMD. A subsequent study found that the inclusion of electrostatic damping reduces the anion propensity for the air-water interface as a consequence of the lower average induced dipole [118]. However, this study was conducted with single (the same) ions which do not provide an accurate representation of real interfacial environments which have different species present near the interfacial region.

In the study detailed in this chapter, we try to better understand ion distributions at the air-water interface, specifically how the inclusion of electrostatic damping in ionic models influence interfacial properties. We parameterized and studied NaCl, NaBr, NaI, and SrCl<sub>2</sub> aqueous systems, and calculated various thermodynamic properties, which we then compare with experiment.

## 4.2 Model Development

### 4.2.1 Interaction Potential Form

All models used for this work were classical and included a combination of point charges, point polarizabilities, and Buckingham exponential-6 (exp-6) intermolecular interactions. The water model used for this work was flexible and developed previously, as described in detail elsewhere [119]. Briefly, the water model included four interaction sites with a van der Waals site located on the oxygen atomic position, and partial positive

charges located on the hydrogen atomic positions. There was another m-site located along the oxygen-hydrogen bond bisector that included a point polarizability and partial negative charge. The electrostatic charges themselves were dependent on the geometry of the water molecules, with a larger bond angle and long bond lengths corresponding to a more positive hydrogen charge. Previous work has found that this is necessary to reproduce both the gas phase and liquid phase water geometry [120]. While this feature is important for simultaneously capturing the gas and liquid phase water geometry, it does not allow the use of multiple timesteps, since molecular vibrations are related to intermolecular interactions in this model [121]. Because of this, a 0.2 fs timestep is required for all interactions, significantly increasing the computational costs of these simulations.

Van der Waals interactions were described with the exp-6 interaction potential of the form,

$$U_{vdw} = \epsilon \left[ \frac{6}{\lambda} \exp\left(\lambda \left[1 - \frac{r}{\sigma}\right]\right) - \left(\frac{\sigma}{r}\right)^6 \right] \quad \text{Eq. 4-1}$$

where  $\lambda=13.5$  for all interactions, while a different  $\sigma$  and  $\epsilon$  value were used for each interaction type, and are given in Table 4-1.

**Table 4-1:** Showing Force Field Parameters Used to Describe the Ions

Ion	$\sigma$ (Å)	$\epsilon$ (kcal/mol)	$\alpha$ (Å <sup>3</sup> )
Na <sup>+</sup>	2.65	0.2	0.157
Sr <sup>2+</sup>	3.70	0.1	0.860
Cl <sup>-</sup>	4.89	0.1	5.482
Br <sup>-</sup>	5.20	0.1	7.268
I <sup>-</sup>	5.62	0.1	10.275

Unlike interactions were handled with the standard Lorentz-Berthelot combining rules: geometry mean for  $\epsilon$  and arithmetic mean for  $\sigma$ . The ions had integer charges on their atomic positions, along with point polarizabilities taken from *ab initio* derived gas phase values from the literature [122-123], and given in Table 4-1. Polarizable interactions allow induced dipoles to form in response to the electric field. Often times, a self-consistent iterative procedure is used to calculate the induced dipoles of a system, but a more efficient way is used for this work, the always stable predictor corrector method [124]. With regular polarizable interactions, induced dipoles are often overestimated by a significant degree in comparison with *ab initio* molecular dynamics (AIMD) simulations [117]. A way to overcome this is to introduce Thole damping to electrostatic interactions, which has been shown to bring agreement between AIMD and classical simulations [115-118]. The total electrostatic potential of the system is given as a summation over interaction sites,

$$U_{ij}^{\text{elec}} = \sum_{i < j} \left[ \frac{q_i q_j f_0(r_{ij})}{4\pi\epsilon_0} \right] - \frac{1}{2} \sum_i \bar{\mu}_i \mathbf{E}_i^0 \quad \text{Eq. 4-2}$$

where the relevant terms are described earlier in Section 2.6.3. The dampening potentials,  $f_i(r_{ij})$  functions are 1 when  $r_{ij} \geq 5 \text{ \AA}$ , but at shorter distances, they become smaller, dampening the electrostatic interactions,

$$f_0(r_{ij}) = \frac{1 - \exp[-0.44(r_{ij}/A)^3] + 0.44^{1/3}(r_{ij}/A)\Gamma(2/3)Q[2/3, 0.44(r_{ij}/A)^3]}{r_{ij}} \quad \text{Eq. 4-3}$$

$$f_1(r_{ij}) = 1 - \exp[-0.2(r_{ij}/A)^3] \quad \text{Eq. 4-4}$$

$$f_2(r_{ij}) = 1 - [1 + 0.3(r_{ij}/A)^3] \exp[-0.3(r_{ij}/A)^3]. \quad \text{Eq. 4-5}$$

Where  $Q$  is the incomplete gamma function that is calculated from *Numerical Recipes* [100], and  $\Gamma(2/3)$  is the gamma function. For  $A$ , it depends on the polarizabilities between interacting sites, and is given by  $A = \delta(\alpha_i \alpha_j)^{1/6}$  with  $\delta = 1.0$  for all water-water and water-ion interactions. For water itself, there is a single point polarizability located on its  $m$ -site and the hydrogens do not have polarizable interactions themselves. To remedy this, the point polarizabilities from another water model was used *only* to calculate the  $f_i(r_{ij})$  functions, which were  $\alpha_m = 0.837 \text{ \AA}^3$  for the water  $m$ -site and  $\alpha_H = 0.496 \text{ \AA}^3$  for the water hydrogens [125]. Notice however, that there are different prefactors, 0.44, 0.2, and 0.3, used for  $f_0$ ,  $f_1$ , and  $f_2$ , respectively. Another exception to the rules for  $A$  was for iodide. Iodide was found in previous work to not reproduce the dipole distribution in water using its *ab initio* derived gas phase polarizability, but for the calculation of  $A$ , a value of  $1.5 \times \alpha_i$  was used [118].

#### 4.2.2 Ion-Water Interaction Parameterization

The only parameterization that took place for the ion interactions with water was in the  $\sigma$  and  $\epsilon$  values. These were parameterized to reproduce the free energy of

hydration for the ions. The staged free energy perturbation (FEP) method was used to calculate the hydration free energies [126]. In general, staged FEP calculates the free energy difference between two states, state A and state B via  $n-1$  intermediate steps,

$$\Delta G = G_B - G_A = \sum_{i=1}^{n-1} G_{i+1} - G_i \quad \text{Eq. 4-6}$$

where  $G_1 = G_A$  and  $G_n = G_B$ . For each of these steps, the free energy difference between the individual states is given as,

$$G_{i+1} - G_i = -k_B T \ln \left\langle \exp \left( -\frac{U_{i+1} - U_i}{k_B T} \right) \right\rangle_i \quad \text{Eq. 4-7}$$

where  $U_i$  represents the potential energy of state  $i$ , and  $k_B$  Boltzmann's constant. The intermolecular potential energy of each state is defined by the following,

$$U_i = \lambda_{\text{vdW},i} U_{\text{vdW}} + \lambda_{\text{elec},i} U_{\text{elec}} \quad \text{Eq. 4-8}$$

where  $U_{\text{vdW}}$  and  $U_{\text{elec}}$  are the intermolecular van der Waals (exp-6 interaction for this situation) and electrostatic potential energies, respectively. For each state,  $i$ , different  $\lambda$  values were used, with progressively larger values between  $i=1$  and  $i=n$ . For each simulation stage, the forces from the potential energy of state  $i$  in the  $NpT$  ensemble are used to sample configurations of the system, and the difference in energy between state  $i+1$  and state  $i$  is used to calculate the free energy difference as shown in state 9. In total, nine different stages were used, which included  $(\lambda_{\text{vdW},i}, \lambda_{\text{elec},i}) = [(10^{-5}, 0), (10^{-3}, 0), (0.1, 0), (0.5, 0.01), (1, 0.1), (1, 0.4), (1, 0.65), (1, 0.85), (1, 1)]$ . For each stage, a total of 0.4 ns of equilibration preceded a 1.6 ns production run. Further simulation details are given in later Sections of this chapter. All uncertainties were calculated by splitting the simulations into 4 blocks and calculating the standard error of the mean.

### 4.2.3 Ion-Ion Interaction Parameterization

For many models, ion-ion interactions, are not parameterized, and for the current model, the ideal situation would be for no additional parameterization of them to be required. It should be recalled that  $A=\delta (\alpha_i\alpha_j)^{1/6}$  for Equations 4-5 to 4-7 with  $\delta=1.0$  for all ion-water and water-water interactions. If one uses  $\delta=1.0$  for ion-ion interactions, the ions associate to an unphysically strong degree. Because of this,  $\delta$  values less than one were needed, which required an additional parameterization to be included for ion-ion interactions. To be consistent with how we parameterized ion-water interactions (to thermodynamic properties), we sought to parameterize ion-ion interactions to thermodynamic properties as well. Two common ways to describe the difference between ion-ion to ion-water interactions are osmotic and activity coefficients. There are multiple ways to calculate these via molecular simulation, but often require carrying out multiple very long simulations starting out at infinite dilution [127-128]. A very creative way to calculate the osmotic coefficient is to explicitly simulate a system with a semi-permeable membrane and more directly extract the osmotic coefficient [129]. Another approach to estimate the activity coefficients is to use KB integrals [130-132], which are extracted from the ion-ion, ion-water, and water-water radial distribution functions (RDFs),

$$G_{ij}(r) = 4\pi \int_0^r [g(s) - 1] s^2 ds \quad \text{Eq. 4-9}$$

where  $g(s)$  is the RDF. These can be used to determine the change in the activity coefficient as a function of salt concentration,

$$a_{cc} = 1 + \left( \frac{\partial \ln \gamma_c}{\partial \ln \rho_c} \right) = \frac{1}{1 + \rho_c (G_{cc} - G_{cw})} \quad \text{Eq. 4-10}$$

where  $\gamma_c$  is the component activity coefficient and  $\rho_c$  is the component concentration. To determine the value of  $G_{cc}$  and  $G_{cw}$  for a system with ions, the following relations are used for a salt with cations (+) and anions(-),

$$G_{cc} = \left(\frac{n_+}{n}\right)^2 G_{++} + \left(\frac{n_-}{n}\right)^2 G_{--} + \frac{n_+ n_-}{n^2} (G_{+-} + G_{-+}) \quad \text{Eq. 4-11}$$

where  $n_+$  and  $n_-$  are the number of cations and anions, respectively, and  $n$  is the total number of ions. There are ways to relate  $G_{++}$  with  $G_{--}$  by imposing local electroneutrality [133-135]. This approach was already developed for a nonpolarizable aqueous alkali-halide ions, in which  $a_{cc}$  as a function of concentration was compared with experiment [134].

While it would be desired to investigate  $a_{cc}$  at many different concentrations, the fact that such a small timestep, along with the fact that polarizable interactions are used only allows for one point to be used. A fairly high concentration of 3M is used for NaX salts (2.7 for  $\text{SrCl}_2$ ). The reason for this is that the calculation of  $G_{+-}$ ,  $G_{++}$ , and  $G_{--}$  are very slow to converge, and higher concentrations of ions allows a faster collection of statistics. A total of 3.2 ns of simulation time was carried out for each point after extensive equilibration of at least 0.4 ns, with the uncertainties estimated by splitting them into 4 blocks.

### 4.3 Simulation Details

Multiple types of MD simulations were carried out for this work, including simulations to calculate the free energy of solvation, to calculate KB integrals, and interfacial simulations. For all simulations, a timestep of 0.2 fs was used, and the temperature was set at 298K with the Berendsen thermostat [136]. As described

previously, polarizable interactions are handled with the always stable predictor-corrector algorithm [124], which is more efficient than typical self-consistent field approaches. A potential truncation of 12 Å is enforced for van der Waals interactions, with analytical tail corrections, and the particle mesh Ewald summation technique is used to handle long-ranged electrostatics [96]. The Amber10 simulation package was used for the calculations [137], and was modified to handle the exp-6 potential, Thole damping, Morse potentials, geometry-dependent charges, and the always stable predictor-corrector algorithm.

The simulations to calculate the free energies of solvation included 1000 water molecules in a cubic box and a single ion. These were carried out in the *NPT* ensemble with the pressure controlled with the Berendsen barostat [136]. The staged FEP method was used to calculate the free energies of ion solvation, which is described, along with more simulations details, in later Sections. For the calculation of  $a_{cc}$ , a total of 2669 water molecules were placed in a cubic box with the specified concentration of ions. These included 144 ion pairs for the 3M NaCl, NaBr, and NaI systems, and 130 SrCl<sub>2</sub> ion sets for the 2.7 SrCl<sub>2</sub> simulations. All of these were in the *NPT* ensemble, in which 3.2 ns was used to calculate the KB integrals. Since these simulations were used to parameterize the model, multiple different simulations were carried out in total for each system.

The third type of simulation, at the air-water interface, was carried out in the *NVT* ensemble. For these systems, both 1M and 3M concentrations were simulated for NaCl, NaBr, and NaI, while 1M and 2.7M was used for SrCl<sub>2</sub>. The configurations from the simulations to calculate the KB integrals were used as starting points for the air-water interfacial simulations. These equilibrated and isotropic systems had their boxlength

extended in the  $z$ -dimension by a factor of 3, giving approximate dimensions of  $45 \times 45 \times 135$  Å. The molecular coordinates were not extended with the boxlength, resulting in a third of the box, approximately, being occupied by liquid, and the rest by vacuum. As a consequence, two air-water interfaces formed bisection the  $z$ -axis. For the 1M simulations, the coordinates from the 3M simulations were extracted, following by the removal of a third of the ions at random, enforcing neutrality. Then, further NPT simulations were carried out for 1 ns, followed by the same procedure for forming air-water interfaces as described for the 3M and 2.7M systems. These air-water systems were equilibrated for a total of at least 1 ns, and production runs of 4ns were carried out following them.

## 4.4 Results and Discussions

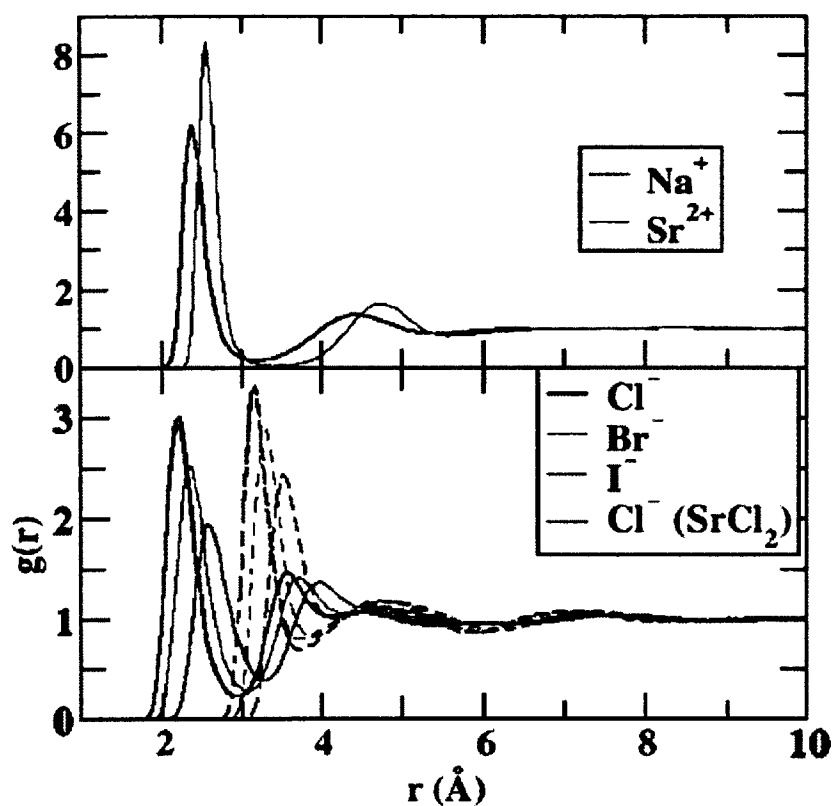
### 4.4.1 Single Ion Solvation

Table 4-2 gives the free energies of hydration that were calculated from the staged FEP method, along with comparisons with the experimental work of Marcus [138], which was used due to the fact that it does not include surface potential contributes (see the recent work by Beck for a more thorough description) [139].

**Table 4-2:** Showing a Comparison of the Free Energy of Hydration for the Ions Investigated

Ion	$\Delta G$ (kcal/mol)	
	Simulation	Experiment <sup>[138]</sup>
Na <sup>+</sup>	-85.56±0.5	-87.2
Sr <sup>2+</sup>	-342±1.5	-330
Cl <sup>-</sup>	-81.8±0.9	-81.3
Br <sup>-</sup>	-77.8±1.1	-75.3
I <sup>-</sup>	-69.6±1.4	-65.7

The agreement between simulation and experiment is reasonable for these. Also, to compare the interaction with water, the RDF between the different ions and water molecules was calculated from the bulk 3M (2.7M for SrCl<sub>2</sub>) aqueous simulations, and is given in Figure 4-1.



**Figure 4-1:** Cation-oxygen (top), anion-oxygen (bottom, dashed lines), and anion-hydrogen (bottom, solid lines) RDFs from the 3M NaX systems and the 2.7M  $\text{SrCl}_2$  system

The halide-water RDFs are similar to what has been reported elsewhere, showing strongest binding between water and chloride, weaker between bromide and water, and the weakest between water and iodide. What is particularly interesting is the strong interaction between water and strontium, which is expected, due to the fact that it is a divalent cation.

#### 4.4.2 Concentrated Bulk Aqueous Solutions

The cation-anion RDFs obtained from the 3M (2.7 M for  $\text{SrCl}_2$ ) bulk simulations are shown in Figure 4-2.

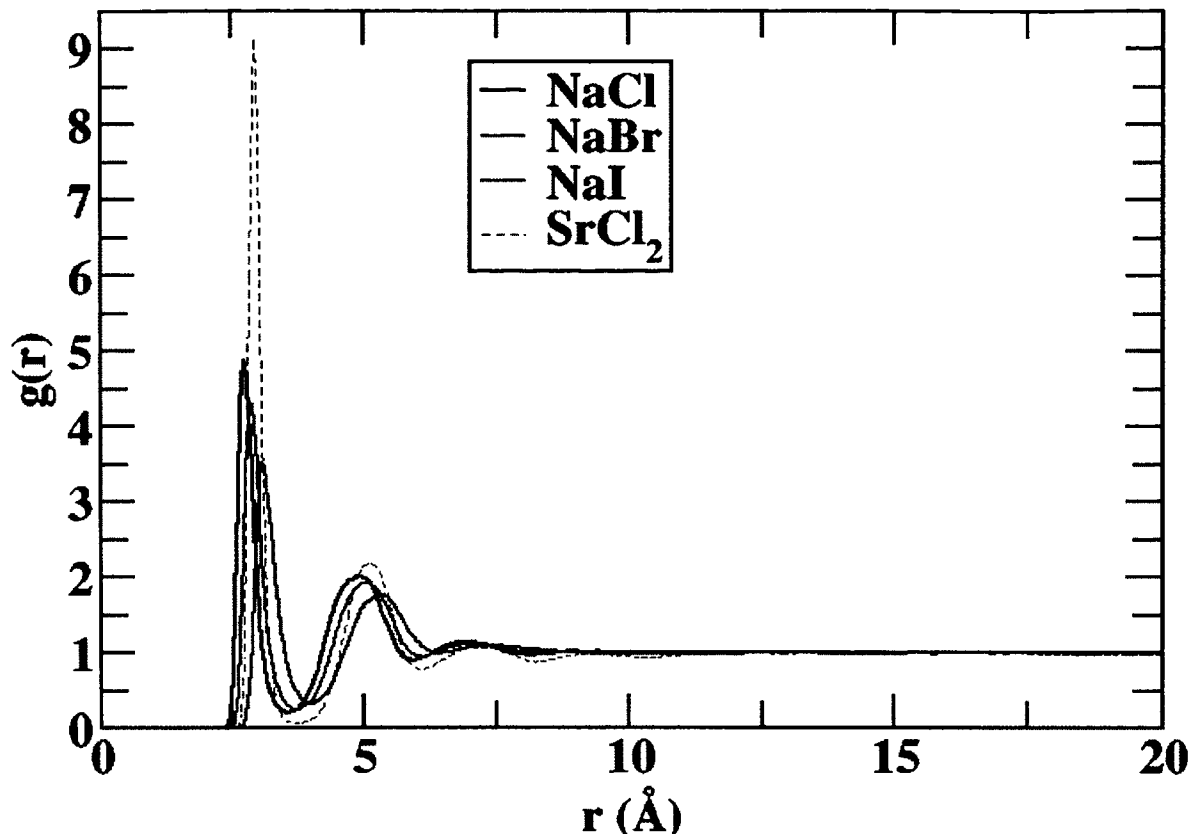


**Figure 4-2:** Cation-anion RDFs for the 3M NaX and 2.7 M SrCl<sub>2</sub> systems

For the sodium halides, there is the expected behavior of the NaCl interaction being the strongest and the NaI interaction being the weakness. It should be pointed out, that this interaction was parameterized too, but not the RDFs specifically, but to the  $a_{cc}$  values extracted from Eq. 4-12. The SrCl interactions have varied significantly in the literature, ranging from very strong, to very weak [35, 140-141]. The SrCl RDF in this work is between that of the previously referenced work, stronger than any of the sodium-halides. It should also be pointed out that the RDFs are shown out to a distance of 20 Å, and the RDF becomes fairly flat after around 12.5 Å in all cases, which is important to extract a KB integral. The KB integrals extracted from the RDFs are given in Figure 4-3.

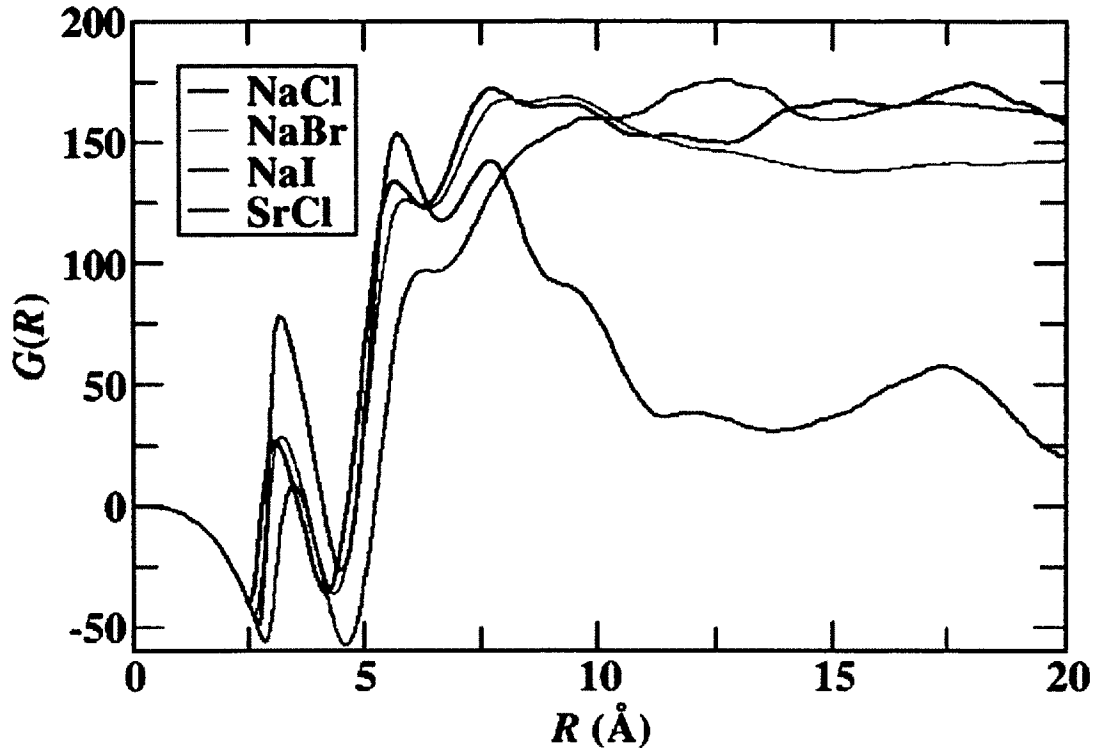


**Figure 4-3:** KB integrals as a function of integration distance obtained from the 3M NaX and 2.7M SrCl<sub>2</sub> systems

It can be observed that they oscillate to some degree until they reach near  $r=12$  Å, after which they are fairly constant. KB integrals were extracted from all RDFs between different ions and ion-water, but cation-anion were the most difficult to converge. It can also be observed that despite the fairly long simulation times (3.2 ns), that there are still significant oscillations in the cation-anion KB integrals.

The KB integrals were used to extract  $a_{cc}$  via Eq. 4-12. The uncertainties were calculated by breaking the simulations into four 0.8 ns blocks. The experimental values were extracted from the activity coefficients in ref. [142], which are given as a function of concentration. Eq. 4-12 shows that the change in the logarithm of the activity coefficient as a function of the logarithm of concentration can be used to extract  $a_{cc}$ . To do this, a cubic spline interpolation was used to determine the derivative of the logarithm

of the activity coefficient at the 3 M concentration for NaX and 2.7 M for SrCl<sub>2</sub>. The value for  $\gamma$  in  $A=\delta(\alpha_i\alpha_j)^{1/6}$ , which is used to determine the degree of electrostatic damping at short ranges in Equations 4-5 to 4-7, was modified until reasonable agreement between simulation and experiment for  $a_{cc}$  was achieved. The value arrived at for  $\gamma$  is given in Table 4-3 also.

**Table 4-3:** The Value of  $\delta$  used and a Comparison of the  $a_{cc}$  Values Calculated from Simulation and Experimental Activity Coefficients According to Eq 4-12

Ion	$\delta$	Simulation	Experiment
NaCl	0.74	1.12±0.1	1.24
NaBr	0.75	1.20±0.1	1.36
NaI	0.74	1.38±0.2	1.54
SrCl <sub>2</sub>	0.85	2.58±0.2	2.45

Due to the long simulation time required to get good estimates of  $a_{cc}$ , perfect agreement was not achieved, but the agreement in the end is still reasonable, as shown in Table 4-3. It can also be observed, that the  $\delta$  values are almost identical for the monovalent cation-anion interactions, while higher for the divalent cation-anion interaction, showing some consistency. It should be noted that the ion-ion RDF is quite sensitive to the value of  $\delta$ , in which if NaBr had  $\delta=0.74$  instead of 0.75, its first peak would be lower than the first NaI RDF peak.

#### 4.4.3 Interfacial Ion Distributions

Figure 4-4 shows the density profiles for the NaX systems investigated, which included concentrations of both 1M and 3M.

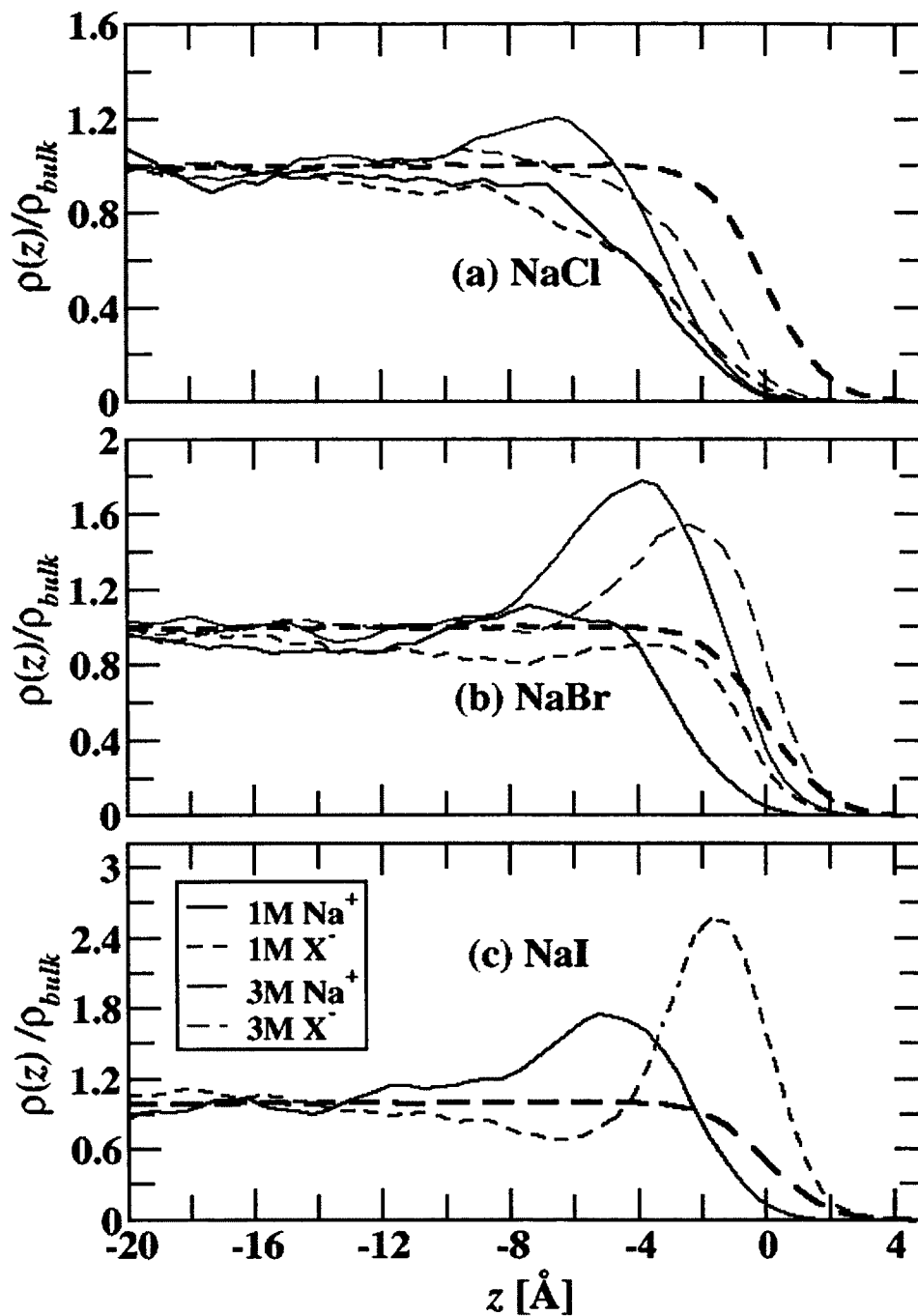


**Figure 4-4:** Density profiles of 1M (blue lines) and 3M (red lines) NaX systems.

The 3M NaI results are not included as there were issues in equilibrating them, and potentially major system size effects, in which rather large systems are required when ion interfacial concentration is large [143]. The plots are scaled by the average bulk

concentrations, and zero in  $z$  represents the GDS, which was fit to a hyperbolic tangent function [70]. NaCl shows a very weak double layer, as it can be observed that for both concentrations, as the chloride density is somewhat shifted towards the air, in comparison with sodium. In addition, NaCl ions are repelled from the air-water interface, as their concentration at the GDS is less than 0.2 with respect to bulk. NaBr shows a more significant double layer than NaCl, but still not any significant interfacial propensity. This is consistent with previous work that shows NaBr having a higher interfacial concentration than NaCl, but much lower than previous results with polarizable potentials [11, 24, 26]. NaI shows both a significant double layer and significant ion interfacial concentration. In summary, ion interfacial behavior, including the trends with respect to large anions, is consistent with previous work utilizing polarizable potentials, but with significantly reduced interfacial concentration [11, 24, 26].

Most previously developed polarizable models do not include the effect of electrostatic damping, and have shown significant ion propensity for the air-water interface [11, 24, 26]. To better study this, Figure 4-5 gives a comparison of our work with previous work by one of us to investigate ion propensity for the air-water interface using the Dang-Chang (DC) class of polarizable models [33, 91], which utilize a rigid water model and ions with integer charges and point polarizabilities [25, 70, 94, 105].

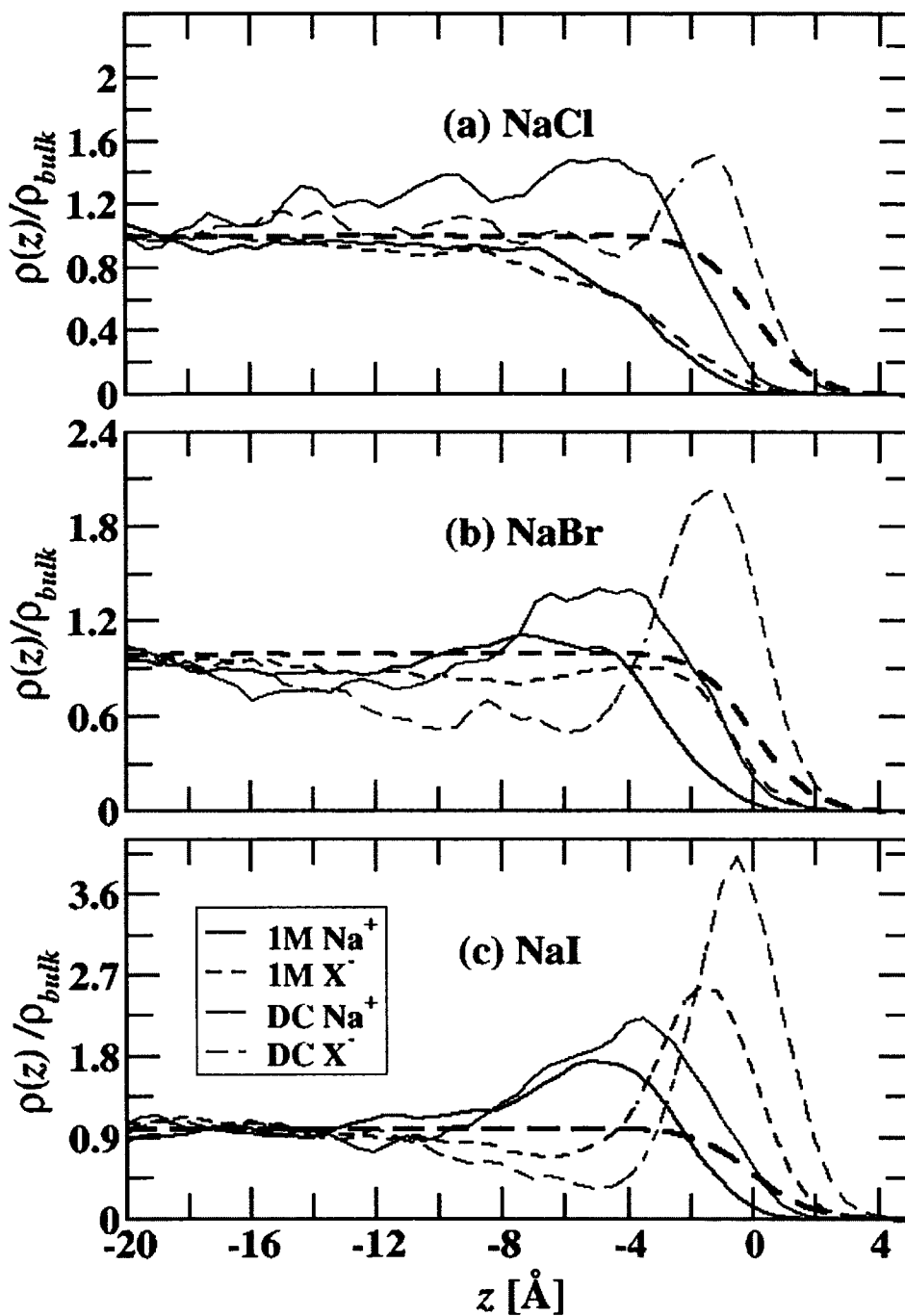


**Figure 4-5:** Density profiles of 1M NaX systems comparing our model (solid lines) with the D-C model (dashed lines).

From the results in Figure 4-5, it is clear that the DC models have a much greater propensity for the air-water interface than the ones simulated for the current work.

Specifically, the DC model shows a chloride propensity for the air-water interface, a strong surface density enhancement of bromide, and iodide interfacial concentration that peaks at approximately to four times the bulk concentration. This is in obvious contrast to the results from the current work, which shows little to no ion propensity for NaCl and NaBr, and about half the height in concentration peak as the DC model results. Previous studies have found that models that do not include electrostatic damping overestimate the average anion induced dipole in bulk water [115-118]. When electrostatic damping has been included in the models, the average anion induced dipole is lowered and shows agreement with AIMD simulations [115-118]. Moreover, a higher induced dipole has been linked to a greater anion propensity for the air-water interface [91, 118]. which is consistent with these results. One should also note that ion-ion interactions have a modest effect on alkali-halide propensity for the air-water interface, making ion size and polarizability the most likely major driving forces for ion propensity for the air-water interface [144].

Figure 4-6 gives the interfacial ion distributions for the SrCl<sub>2</sub> system. It is clear that there is a double layer forming, as the chloride density profile is shifted more toward the air, and this effect is greater than for NaCl.

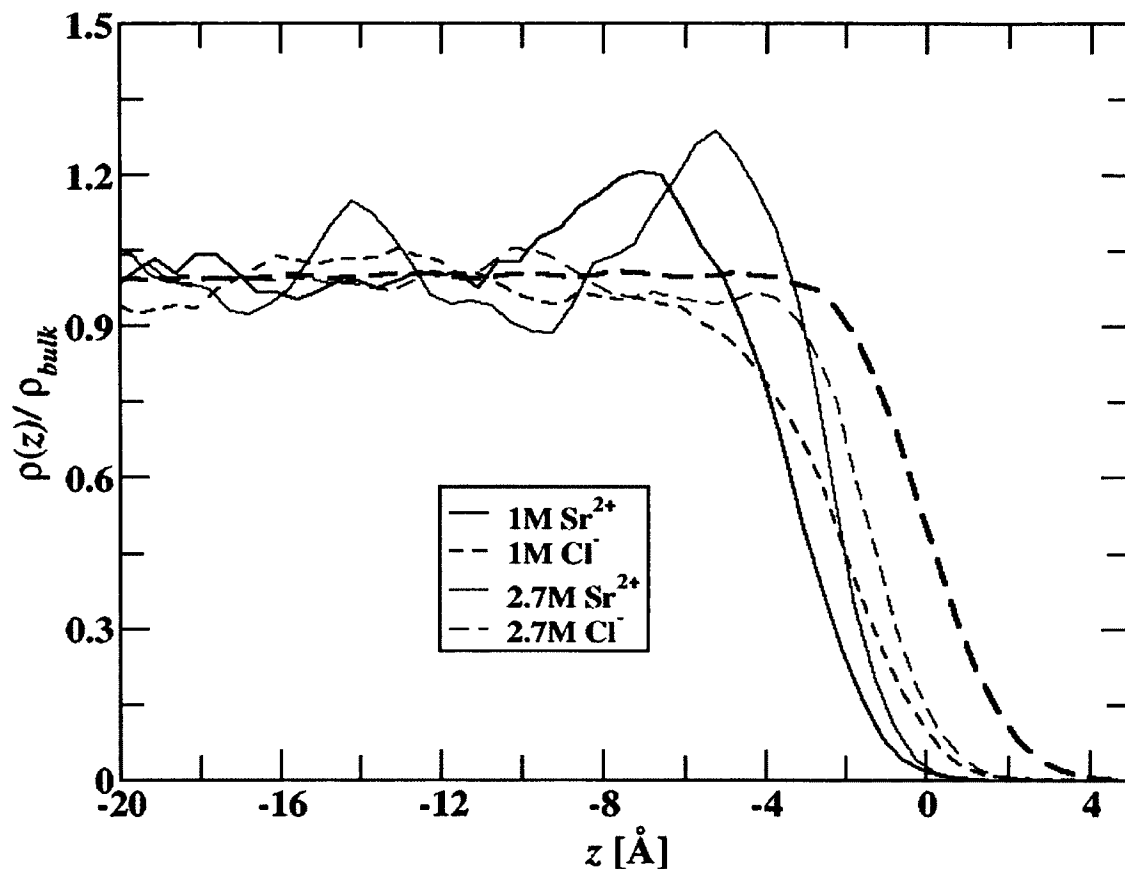


Figure 4-6: Density profiles of the 1M and 2.7M SrCl<sub>2</sub> solutions

Moreover, there is a peak in strontium density 4-6 Å from the GDS, showing a propensity for the region near the air-water interface. A previous study of SrCl<sub>2</sub> at the air-water interface had a very large peak in ion density [35], but this was found to be attributed to the overbinding of strontium and chloride [141]. The latter study showed very weak binding between ions in water, and a strong double layer formed at the air-water interface utilizing the DC model. The current work has moderate binding between ions, and a minor double layer forms. The reason for the lack of a strong double layer, in comparison with previous work, is likely because the weaker propensity the chloride ion has for the air-water interface as also shown in Figure 4-5 for NaCl. It is still of high

interest that the presence of a divalent cation appears to result in a buildup of cation density near the air-water interface. Very recent experimental work has found that divalent magnesium ions build up at the surface of salt particles (see supporting information in ref. [145]). It should also be noted that the type of divalent cation has been known to play a role in the interfacial structure [146], and will be the subject of future work.

#### 4.4.4 Surface Tensions and Excesses

Surface tension is a common way to compare interfacial properties between simulation and experiment. A common way to calculate it is to use the pressure tensor from the MD simulations [147]. However, the uncertainty in these values scale with the system size, and for the present systems the uncertainty is too large to get a quantitative calculation of the difference in surface tensions. Another way to estimate the change in surface tension with the addition of solutes is to first calculate the surface excess [11, 107],

$$\Gamma_s = \int_{-\infty}^{z_{\text{GDS}}} [\rho_s(z) - \rho_{sb}] dz + \int_{z_{\text{GDS}}}^{+\infty} \rho_s(z) dz \quad \text{Eq. 4-12}$$

where  $\rho_s(z)$  is the density profile of the solute and  $\rho_{sb}$  is the density of the solute in the bulk of the solution,  $z_{\text{GDS}}$  is the GDS, negative values represent bulk liquid, and positive values towards the air. Gibbs' thermodynamic theory of interfaces links the change in surface tension with respect to the logarithm of activity with the surface excess [148],

$$\Gamma_s = -\frac{1}{RT} \left( \frac{\partial \gamma}{\partial \ln a_s} \right)_T \quad \text{Eq. 4-13}$$

where  $R$  is the molar gas constant,  $\gamma$  is the surface tension, and  $a_s$  is the activity of the solute. Using thermodynamic tables for the solute activities and surface tensions, the surface excess at a specified concentration can be calculated. We estimated the values for experimental surface excess from Eq. 4-15 using experimental solute activities and surface tensions with respect to concentration [110, 142]. Moreover, we used Eq. 4-14 to calculate surface excess values from our simulation data at 1M and 3M (2.7M for  $\text{SrCl}_2$ ), and also from the 1M NaX solutions for the DC model ( $\Gamma_{\text{DC}}$ ).

Table 4-4 compares simulation results for the surface excess with those derived from experimental surface tensions.

**Table 4-4:** Showing Computed versus Experimental Surface Excesses

System	$\Gamma_{\text{comp}}(\text{nm}^{-2})$	$\Gamma_{\text{exp}}(\text{nm}^{-2})^{[107]}$	$\Gamma_{\text{DC}}(\text{nm}^{-2})$
1M NaCl	-0.49±0.1	-0.405	-0.359
3M NaCl	-2.4±0.3	-1.253	
1M NaBr	-0.37±0.1	-0.321	-0.281
3M NaBr	-1.3±0.4	-0.969	
1M NaI	-0.33±0.1	-0.255	-0.180
1M $\text{SrCl}_2$	-0.91±0.03	-0.805	
2.7M $\text{SrCl}_2$	-1.9±0.2	-2.346	

Surface excess values computed from the activity dependence of experimental surface tension data[107].

The uncertainties from the simulations were estimated by splitting them into 4 1ns blocks, while the DC results were taken from previously calculated density profiles [33], so no uncertainty was allowed to be calculated. There is a negative surface excess for all

models investigated, in qualitative agreement with experiment. The degree of negative surface excess, though, is greater for the new models than the DC models, which is consistent with the density profiles that show weaker ion propensity for the air-water interface for the new models. In comparison with experiment, it appears that the DC model underestimates the degree of surface excess, while the new model overestimates it somewhat for NaCl and NaBr. There may be many reasons for this overestimation. One potential cause is the fact that the new model does not incorporate charge transfer. Recent studies have found that there is appreciable charge transfer between water molecules [149-154], which only has modest effects on the interfacial properties of neat water [155]. However, one of the effects that work to repel ions for the air-water interface are their image charge repulsion [156-157]. If charge transfer were included in the models, it should slightly enhance their propensity for the air-water interface due to a reduction in image-charge repulsion. This is part of an ongoing investigation. For the 1M and 3M NaI solutions, though, there appears to be fairly good agreement between simulation and experiment for the surface excess predicted by the new model. The SrCl<sub>2</sub> systems also predict surface excesses that are close to experiment, showing that the model development works reasonably well for divalent cations.

#### 4.5 Conclusions

We carried out molecular dynamics simulations to examine the interfacial properties predicted by a model that includes both a flexible water model and electrostatic damping. The ion-water interactions were parameterized to reproduce the Gibbs free energy of solvation, while the ion-ion interactions were parameterized to reproduce the change in activity coefficient with respect to concentration at 3M. The

resulting models had a reduced ion propensity for the air-water interface, in comparison with previously developed polarizable models. For NaI, there was a significant anion propensity for the air-water interface, which is consistent with previous work, but this was reduced in comparison. Of particular interest is that SrCl<sub>2</sub> aqueous solutions had a cation propensity for the air-water interface, in which the strontium density peaked at 1.3 times the bulk average value near the interface. The salt surface excess was computed from the simulation and experimental data, showing that our model slightly overestimated the degree of negative surface excess in comparison with experiment, predicted by our model for NaCl and NaBr systems. For SrCl<sub>2</sub>, our model predicted surface excesses that were in good agreement with experiment.

## CHAPTER 5

# EXPLORATION OF PROPERTIES OF THE N-ALKANE/WATER INTERFACE

### 5.1 Introduction

As emphasized in Chapter 1, alkane/water interfaces are considered a prototypical system for studying the interaction of water with hydrophobic liquid surfaces [4], particularly because their molecular structure can be easily modified by varying chain length and their degree of branching. One aspect of the alkane/water interface that may play a fundamental role in its ability to influence interfacial properties is the interfacial width. Previous experimental studies using x-ray reflectivity have found that the interfacial width may increase with *n*-alkane chain length [46, 55, 59]. However, further studies are required to gain a better understanding of why this phenomenon exists; since even if these findings are true, the reason for this occurrence is still not well understood. In this chapter, we examine the *n*-alkane/water interface and the effect of the alkane chain length on the interfacial width. These studies were conducted using molecular dynamics simulations with polarizable interactions. We examined systems of linear alkanes of different chain lengths which included *n*-hexane/water, *n*-heptane/water, *n*-octane/water, and *n*-nonane/water. Figure 5-1 shows a snapshot of the system simulated.

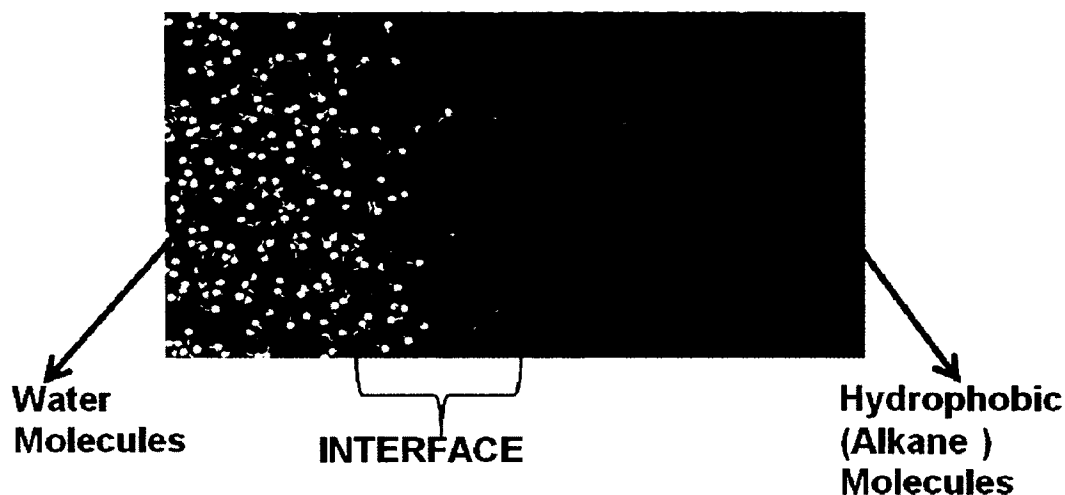


**Figure 5-1:** Showing a snapshot of the alkane/water interface

Figure 5-1 shows a snapshot of one of the *n*-alkane/water systems simulated. The red and white ball and stick representation is of the water molecules (red oxygens and white hydrogens) while the blue and white stick representations is of the alkane chains. A new polarizable force field was developed for *n*-alkanes which gave good agreement with experiment for liquid densities and heats of vaporization for different *n*-alkanes at different temperatures. Also, good agreement with experiment was found for alkane/water interfacial tensions for a variety of alkanes.

## 5.2 Simulation Details

### 5.2.1 Molecular Models

Polarizable molecular models were used for all simulations. For water, the rigid Dang-Chang (D-C) water model was used, which is a 4-site model with a single Lennard-Jones (LJ) site located at the oxygen atomic position. Also, there are partial positive charges located on the water hydrogen positions, and an *m*-site located along the oxygen-hydrogen bisector that has a partial negative charge and a point polarizability [70].

Polarizable ions were used in some simulations, which included single atomic sites with a LJ interaction, integer charge, and point polarizability [25]. A new alkane force field was developed for this work. The model included LJ, point charges, and point polarizabilities on all atomic sites. The model had similar (but differing in charges) parameters for the methyl and methylene carbons, and the same parameters for all hydrogen atoms. The charges were taken from the OPLS-AA force field [158], and all intramolecular bonded interactions (harmonic bond bending, dihedral potentials, and bond stretching) were taken from the GAFF force field [159]. Each atom had a point polarizability, which were taken from the work of Applequist [160]. The LJ parameters were then fitted by carrying out a series of classical molecular dynamics simulations of bulk *n*-hexane at 250 and 298 K and *n*-dodecane at 298 K and 350 K. The values for the intermolecular interaction parameters that were arrived at are given in Table 5-1.

**Table 5-1:** Intermolecular Parameters Used for the Alkane Force Field

Atom	$\sigma$ [Å]	$\epsilon$ [kcal/mol]	$q$ [ $e$ ]	$\alpha$ [Å <sup>3</sup> ]
<b>C(methyl)</b>	3.457	0.058	-0.18	0.878
<b>C (methylene)</b>	3.457	0.058	-0.12	0.878
<b>H</b>	2.486	0.0358	0.06	0.135

During the parameter optimizations, we calculated the thermodynamic properties of bulk liquids including enthalpies of vaporization and densities, and compared them to experiments. The final potential parameters were obtained when the potential model adequately reproduced the experimental values. Table 5-2 gives a comparison between

simulation and experiment [161] for the bulk properties calculated for *n*-hexane and *n*-dodecane, and the agreement with experiment is excellent.

**Table 5-2:** Comparison between Simulation and Experiment for the Bulk Densities and Heats of Vaporizations for the Bulk Alkane Systems Investigated

system	T [K]	$\Delta H_{\text{vap}}$ [kcal/mol]		$\rho_{\text{liq}}$ [g/cm <sup>3</sup> ]	
		sim	exp <sup>a</sup>	sim	exp <sup>a</sup>
<i>n</i> -hexane	250	8.23	8.30	0.704	0.698
	298	7.21	7.64	0.652	0.654
<i>n</i> -dodecane	298	14.86	14.42	0.75	0.745
	350	13.32	13.54	0.702	0.708

### 5.2.2 Simulation Details

The bulk systems were simulated in cubic boxes in the *NPT* ensemble, with the temperature and pressure fixed with the Berendsen thermostat and barostat, respectively [136]. One of the bulk systems included 200 molecules of *n*-hexane and the other had 200 *n*-dodecane molecules. The pressure was set to be 1 atm for all simulations, and the temperatures specified in the previous Section were used. Moreover, four alkane/water systems were simulated, all with 2000 water molecules and 200 *n*-alkane molecules. The interfacial systems simulated included *n*-hexane-water (HEX), *n*-heptane-water (HEP), *n*-octane-water (OCT), and *n*-nonane-water (NON). The interfacial systems were placed in

rectangular boxes in which the  $x$  and  $y$  dimensions were shorter and identical at around 38 Å for all, while the  $z$  dimension was longer, and was around 80 Å. These dimensions were somewhat larger for the NON system than the HEX system due to the fact that the NON system had more atoms. Due to the extended length in the  $z$  dimension, two alkane/water interfaces formed in the systems bisecting the  $z$  axis. The alkane/water systems were all simulated at 298K. Standard Lorentz-Berthelot combining rules were used for the LJ interactions (geometric mean for  $\epsilon$  and the arithmetic mean for  $\sigma$ ). A potential truncation of 12 Å was enforced with analytic tail corrections, and the particle mesh Ewald summation technique used to calculate long-ranged electrostatic interactions [96]. Due to the fact that an interface is present, analytic tail corrections may not be adequate, so different cutoffs were investigated and the results described in Section 5.3.1. The point polarizabilities allow induced dipoles to form at their positions. The determination of the magnitude for these dipoles is a many-body problem, in which self-consistent procedures are often used. For the described work, the always stable predictor corrector algorithm was used, which requires only one evaluation of energy per timestep [124]. A 1 fs timestep was used for the calculations, and 800 ps of production was used for the calculations for each bulk system with uncertainties calculated from 200 ps blocks, while for the interfacial systems, 5 ns of production was used with uncertainties calculated from 500 ps blocks, all of these after extensive equilibration.

### 5.3 Results and Discussions

#### 5.3.1 Density Profiles, Interfacial Tensions and Widths

The interfacial tensions were calculated from the pressure tensors,

$$\gamma = \frac{L_z}{2} \left[ \frac{P_{xx} + P_{yy}}{2} - P_{zz} \right] \quad \text{Eq. 5-1}$$

where  $L_z$  is the boxlength in the  $z$ -direction. Table 5-3 gives a comparison with experiment for the interfacial tensions [162] of the alkane/water interfaces for the systems investigated.

**Table 5-3:** Showing a Comparison of the Simulation and Experimental Interfacial Tensions

<b>SYSTEM</b>	<b>Simulation</b>	<b>Experiment<sup>[162]</sup></b>
<b>HEX</b>	50.3±0.8	50.0
<b>HEP</b>	51.2±1.2	50.3
<b>OCT</b>	48.9±1.1	50.7
<b>NON</b>	51.9±0.9	51.2

The surface tension data in Table 5-3 show that the agreement of our simulation results with experiment is very good. Figure 5-2 gives the density profiles for water and the alkanes for the HEX, HEP, OCT, and NON systems with zero representing the Gibbs dividing surface (GDS) of water.

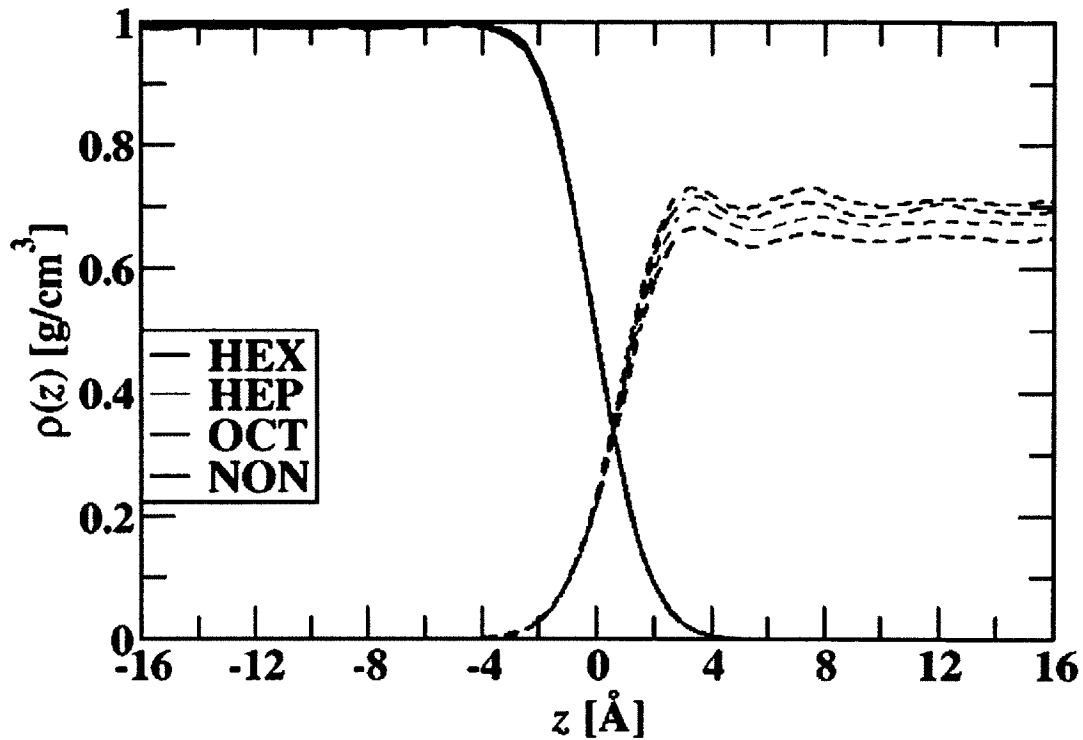


**Figure 5-2:** Density profiles for water (solid lines) and alkanes (dashed lines) for the systems described. The GDS of water is represented as zero.

It should be noted that the GDS for water is approximately 0.5 Å from the GDS of the alkane for the alkane/water systems. The experimental liquid densities for pure *n*-hexane, *n*-heptane, *n*-octane, and *n*-nonane are 0.654, 0.684, 0.703, and 0.718 g/cm<sup>3</sup>, respectively [161]. These are in excellent agreement with the alkane liquid densities away from the alkane/water interface. Furthermore, the bulk *n*-hexane density is very similar to its value in the interfacial system (0.65 g/cm<sup>3</sup>). It is interesting to note that the water density reaches an average value around 5 Å from the GDS with little fluctuation greater than this distance from the GDS. In contrast, the alkane densities show significant fluctuations with density peaks at 3 Å, 7.5 Å, and a much smaller peak around 12 Å from the GDS. These are all approximately 4 Å from one another, which corresponds with the position of the minimum energy for the carbon LJ potential ( $\sigma \times 2^{1/6}$ )

of 3.88 Å. This shows that alkane density fluctuations do not dissipate until far from the alkane/water interface, and that small potential system size effects may be present for the alkane phase.

The interfacial widths were calculated by fitting a hyperbolic tangent function [70] to the water and alkane density profiles and are given in Table 5-4.

**Table 5-4:** Interfacial Widths (in Å) of the Water and Alkane Phases as Fit by a Hyperbolic Tangent Function, Along with the Distance Between the Gibbs Dividing Surfaces (GDS) of the Alkane and Water Phases.

System	Water	Alkane	Intrinsic
HEX	3.46±0.02	3.00±0.02	0.498±0.006
HEP	3.42±0.02	2.98±0.03	0.522±0.005
OCT	3.39±0.04	2.87±0.04	0.528±0.008
NON	3.36±0.03	2.90±0.03	0.534±0.006

Additionally, the distance between the GDS for water and the alkane systems, sometimes referred to as the intrinsic width, are given in Table 5-4. The interfacial widths for both water and the alkanes decrease with increasing alkane chain length. This may be expected as the alkane phases become denser with increasing chain length, which decreases the difference in density between the aqueous and the alkane phases. However, x-ray reflectivity experiments found the opposite trend, that increasing the alkane chain length increased the interfacial width [59]. This discrepancy may be due to many factors. For instance, capillary wave action of a macroscopic interface cannot be completely captured in the simulations [163-165]. There may also be other system size effects in the simulations, and the experiments are related to electron densities and not specific

densities. Finally, the results of Table 5-4 show that the intrinsic width for the alkane/water systems appears to slightly increase with chain length in contrast to the water and alkane density widths. This may explain part of the reason that longer alkane chain lengths appear to expand the interfacial width in contrast with experiments [59] as in principle, the intrinsic width should not depend on system size while the interfacial widths of the alkane and water phases will due to capillary waves. We are currently investigating this and the general interfacial width in detail to better understand this.

Two things were examined to see their effects on interfacial tension. One of these was the cutoff, and the other was how the barostat was applied. To test these, the HEX system simulations were extended 2 ns utilizing one of three simulation protocols. The first one had a regular (12 Å) LJ cutoff and 1 atm barostat (the 3-d barostat), the second had a longer cutoff of 17 Å and 3-d barostat, and the third had the regular cutoff and a barostat of 1 atm in only the  $z$ -dimension keeping the interfacial area constant. The interfacial tensions with uncertainties calculated from five 400 ps blocks for these systems were  $48.7 \pm 1.3$  dyn/cm,  $48.1 \pm 1.5$  dyn/cm, and  $51.4 \pm 1.4$  dyn/cm, respectively. These are fairly close to one another, and near the limits of uncertainty.

### 5.3.2 Interfacial Structural Expansion and Contraction

An important feature of water structure at the air/water interface was the fact that the average distance between first solvation shell neighbors was larger than in the bulk [166]. Simulations only showed this feature with the addition of dipole polarizability or via *ab initio* MD [91, 167-168]. This has not been investigated at alkane/water interfaces, though, and it would be interesting to determine if there is an expansion of water structure as it approaches an alkane phase, which is dense, but has no hydrogen-

bonding interactions. Figure 5-3 shows the average distance between first solvation shell water molecules as a function of  $z$ -position of its center of mass with respect to the GDS of water for the alkane/water systems, along with the results for the air/water [91].

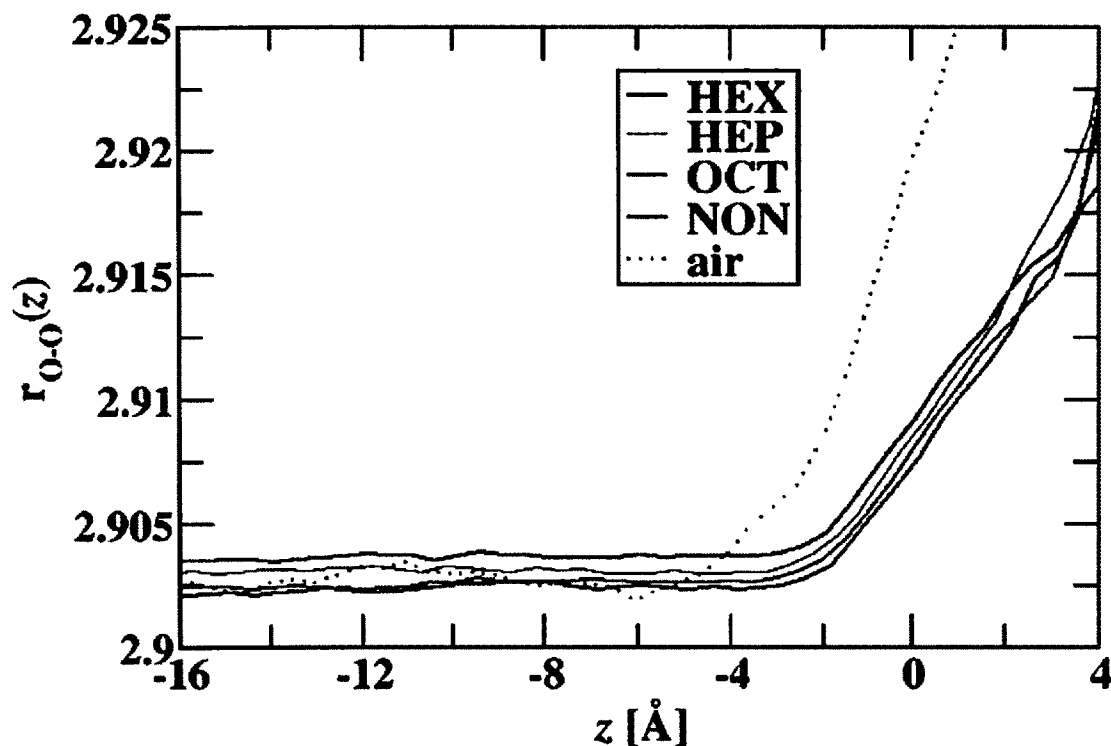


**Figure 5-3:** Average distance between water oxygens in first solvation shell as a function of water center of mass position.

In the bulk, there is slight variability of this average distance, which is probably due to statistics or system size effects, but this difference is small, around 0.03%. What is evident is that as the water molecules approach the alkane/water interface, there is an expansion of their structure. The air/water interface shows a greater expansion than the alkane/water interface, and the expansion at the air/water interface stretches farther away from the GDS. To further understand this difference, Figure 5-4 illustrates the average

induced dipole of water as a function of its center of mass  $z$ -position for the alkane/water systems investigated and the air/water interface.

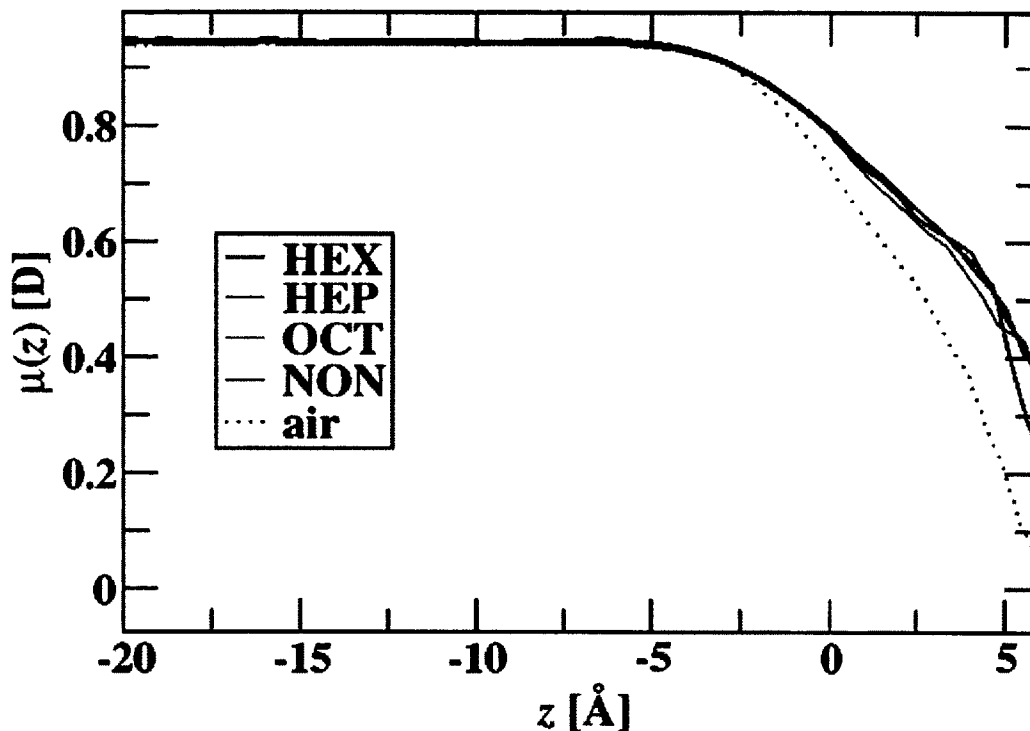


**Figure 5-4:** Average induced dipole of water as a function of center of mass position

The average induced dipole drops off more towards the bulk at the air/water interface than at the alkane/water interfaces, with little change for the different alkane systems. This is not unexpected, as the alkane phases have small electrostatic interactions with the water phase, which should also cause water to have small induced dipoles in response to these interactions.

Unlike water, the alkanes simulated are present next to a phase with a greater density than its own and water-alkane interactions are similar to alkane-alkane interactions (mostly London forces with weak dipole-induced dipole interactions). This would be expected to result in the interface having a significantly different influence on

alkane structure than water structure. To investigate this, Figure 5-5 gives the average distance between *intermolecular* methylene groups of nearest neighbor alkanes as a function of  $z$ -position for the alkane center of mass.

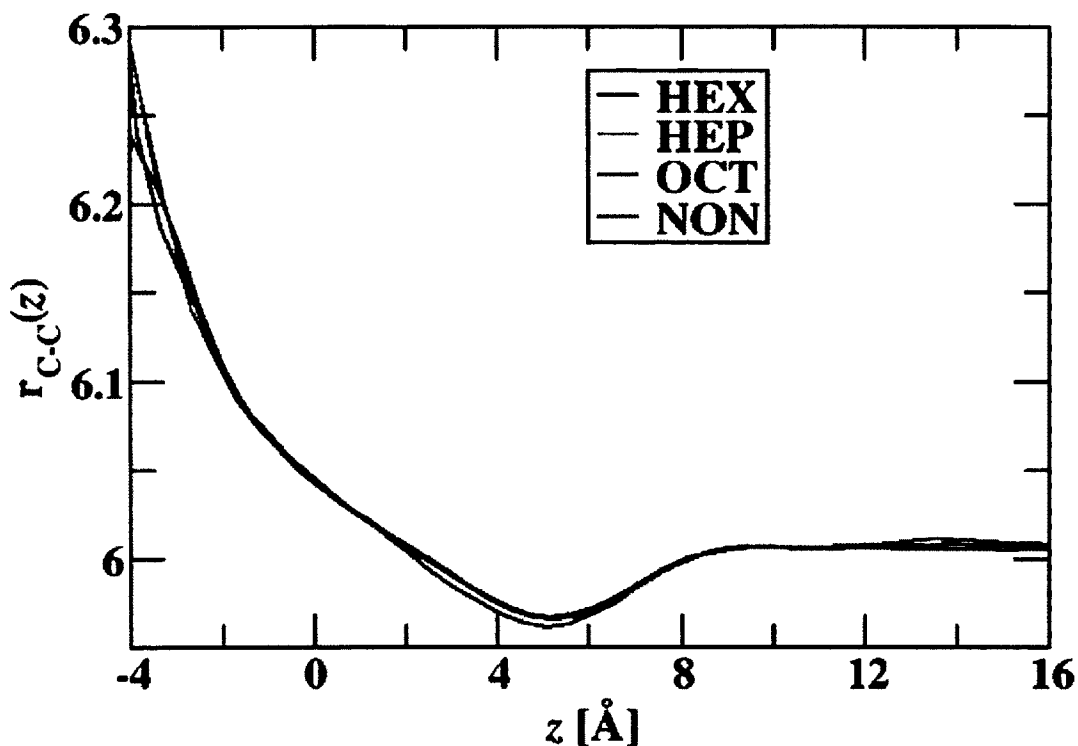


**Figure 5-5:** Average distance between carbons of different molecules in first solvation shell as a function of carbon atomic positions.

It should be noted that the longer alkanes would have fewer intermolecular nearest neighbors, due to the increased likelihood that one of their nearest neighbors are intramolecular. Nevertheless, the average distance between the nearest intermolecular neighbor does not appear to depend on chain length significantly, and is around 6.0 Å. One should also notice that the scale of Figure 5-5 is an order of magnitude greater than that of Figure 5-3 due to larger variability in alkane intermolecular distance. As the alkanes approach the alkane/water interface around the region of 3-8 Å from the GDS

towards the alkane bulk, there is a contraction in intermolecular distance of around 0.03 Å, which is greater than the expansion observed for water as it approaches the alkane/water interface. This region aligns with the region between the two peaks in alkane density profile. Comparing this with the average induced dipole profile for the whole alkane molecule, which is given in Figure 5-6, the average alkane induced dipole increases as the alkane center of mass approaches 8 Å from the GDS, corresponding with the region in which the alkane-alkane contraction is observed.

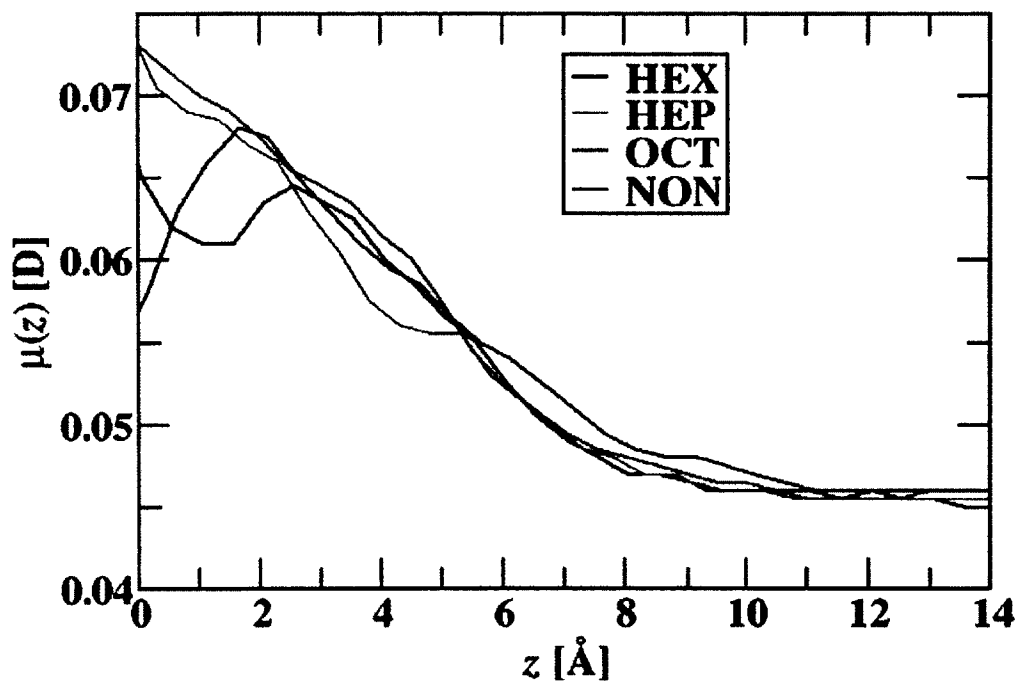


**Figure 5-6:** Average induced dipole of alkane molecules as a function of alkane center of mass position

Just as with the water structure, in which lower induced dipoles leads to expansion, the higher alkane induced dipole appears to lead to its contraction. It should also be noted that Figure 5-4 shows that the alkane structure expands as it crosses the GDS towards the water, in comparison with bulk alkane structure. The average alkane

induced dipole appears to still be higher than the bulk near the GDS, so this is likely not related to the induced dipole. However, near the GDS, there is a lot of water present, which could disrupt the alkane-alkane interactions, leading to the expansion.

The end-to-end distance ( $r_{\text{end}}$ ) squared for the alkanes was calculated as a function of the  $z$ -position of the alkane center of mass, and this property divided by the number of carbons squared is given in Figure 5-7.

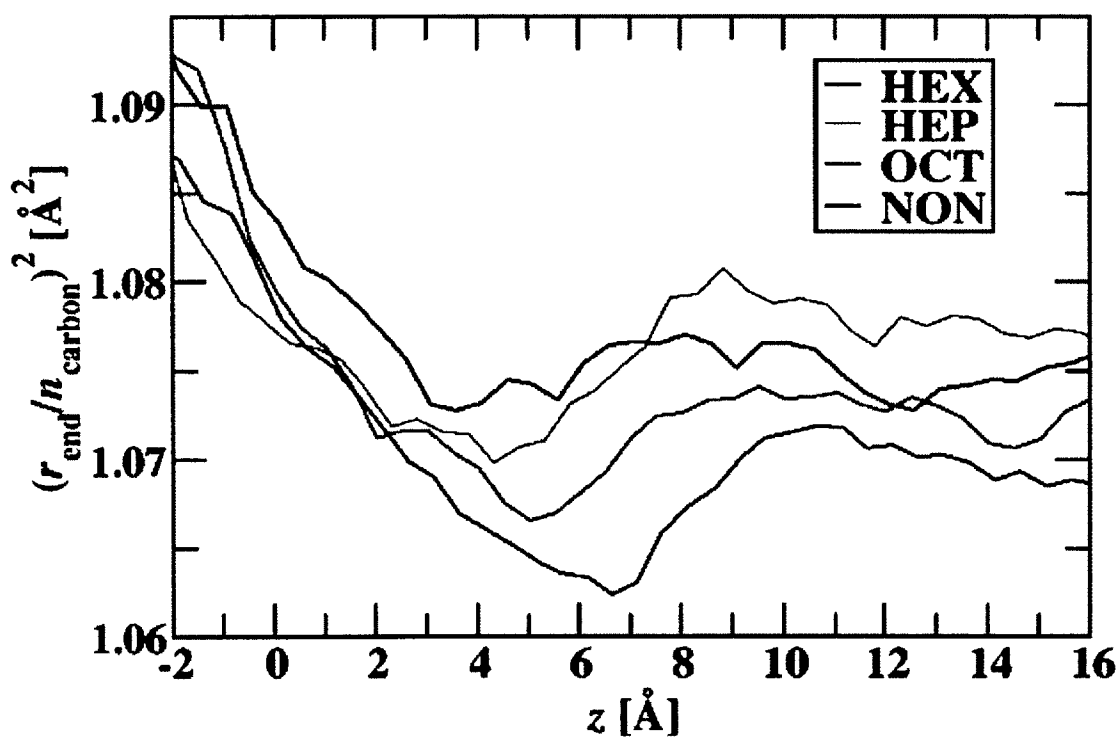


**Figure 5-7:** Alkane end to end distance squared divided by the number of carbons squared as a function of alkane center of mass position.

For all cases,  $r_{\text{end}}$  is higher at the GDS than in the bulk, due to the chains lying somewhat flat on the surface of water, which will be discussed in greater detail later. What is of further interest is that NON, HEP, and OCT show a decrease in  $r_{\text{end}}$  around 6 Å, 5 Å, and 4 Å from the GDS, respectively. In contrast, HEX shows little to no decrease

in  $r_{\text{end}}$  near the interface. It is evident that longer alkyl chain length causes a contraction in  $r_{\text{end}}$  farther away from the GDS. This trend is not unexpected as the longer NON molecule will have parts of it influenced by the interface when its center of mass is farther away from the GDS. The reason for this trend may be related to the apparent stronger interactions with other alkane molecules in this region (4-8 Å from the GDS).

### 5.3.3 Molecular Orientation.

To understand how the alkane/water interfaces affects the orientation of the alkane chains, the angle between the vector connecting adjacent carbon atoms and the  $z$ -axis ( $\theta_z$ ) was calculated as a function of the carbon pair center of mass  $z$ -position. From this angle, the following order parameter was calculated

$$P_2 = \frac{1}{2} (3 \cos^2(\theta_z) - 1) \quad \text{Eq. 5-2}$$

$P_2$  will approach  $-1/2$  when the carbon-carbon vector is parallel to the alkane/water interface, 1.0 when the vector is perpendicular to the interface, and 0.0 when there is no orientational preference. Figure 5-8 displays the average value of  $P_2$  with respect to  $z$ -position for the alkanes studied.

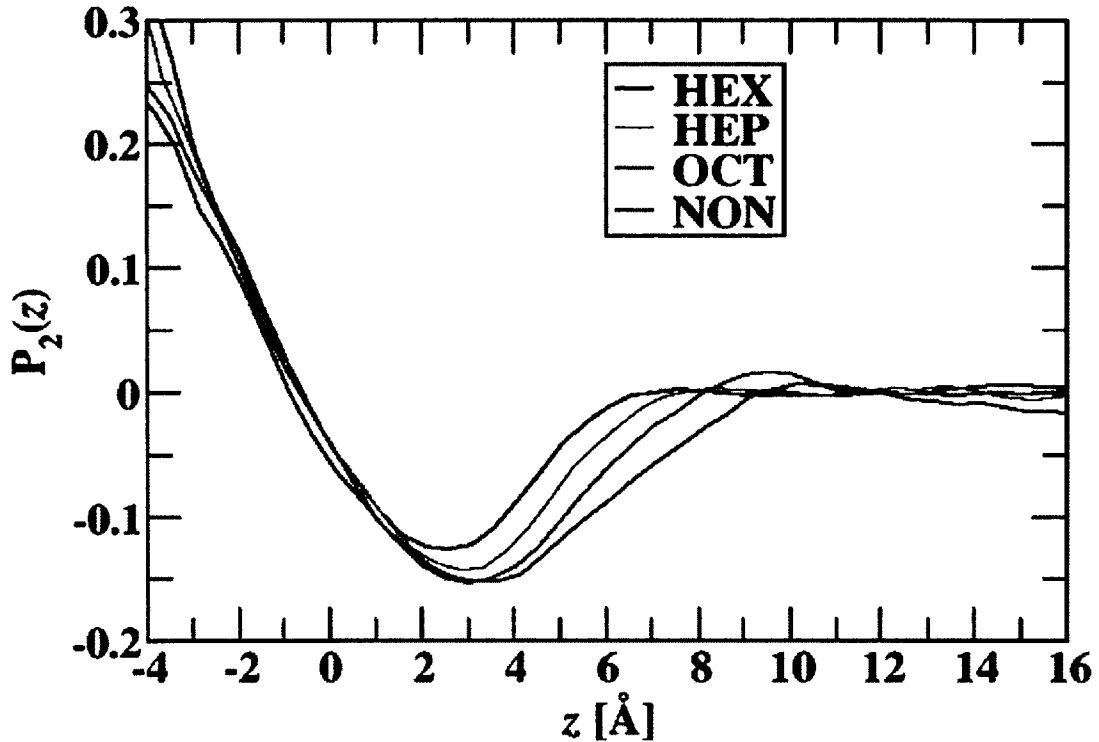


**Figure 5-8:** Profile of average orientational order from the angle of the vector between adjacent carbons and the  $z$ -axis as a function of atomic position.

This orientational preference is present farther away from the GDS the as the length of the alkane chain increases. In fact, NON has a nonzero  $P_2$  average 16 Å from the GDS, which could be indicative of some small system size effects for NON. In the region 0-6 Å from the GDS towards the alkane bulk, there is a strong orientational preference for the carbon-carbon vector to be parallel to the alkane/water interface. This implies that the alkanes lay somewhat flat against the water surface. It is not unexpected that alkanes in contact with a phase in which they are immiscible would lay flat on the surface to maximize contact with the surface while minimize penetration into the water phase. As the alkane position ventures into the aqueous phase in the -4 to 0 Å region (or the region on the water side of the GDS), the alkane carbon-carbon vector is oriented perpendicular to the air/water interface, and this effect is greater the farther from the GDS

the carbons are. This again is not unexpected as the parts of an alkane that ventures into the aqueous phase are likely to have some part of them still in the alkane phase, which would require the carbons penetrating the water phase to orient perpendicular to the interface.

### 5.3.4 Electrostatic Potential

The electrostatic potential as a function of  $z$ -position was calculated for the alkane/water interface using the atomic approach [45, 105, 169]. For our polarizable potential model, the total electric potential difference across the interface is calculated from the partial charges and induced dipoles,

$$\Delta\phi_q(z) = \phi_q(z) - \phi_q(z_0) = -\int_{z_0}^z E(z')dz' \quad \text{Eq. 5-3}$$

$$\Delta\phi_{\mu}^{\text{ind}}(z) = \frac{1}{\epsilon_0} \int_{z_0}^z \langle \rho_{\mu}^{\text{ind}}(z') \rangle dz' \quad \text{Eq. 5-4}$$

$$E_z(z) = \frac{1}{\epsilon_0} \int_{z_0}^z \langle \rho_q(z') \rangle dz' \quad \text{Eq. 5-5}$$

Here,  $E(z)$  is the electric field along the surface normal direction,  $\epsilon_0$  is the dielectric permittivity in vacuum, and  $z_0$  is a reference point that is selected as a point far from the interface in the bulk liquid.  $\langle \rho_q(z) \rangle$  is the ensemble averaged charge density profile, which was evaluated in slabs of 0.25 Å thickness along the  $z$  direction, and  $\rho_{\mu}^{\text{ind}}(z)$  is the  $z$  component of the averaged induced dipole moment. The contributions from water molecules were calculated separate from the contributions from alkanes to compare how they individually affect the electrostatic potential. Figure 5-9 presents the electrostatic potential as a function of position for the whole system and individual contributions from water and alkane molecules as a function of  $z$  position across the

alkane/water interface, along with results from the air/water interface from previous work [33].

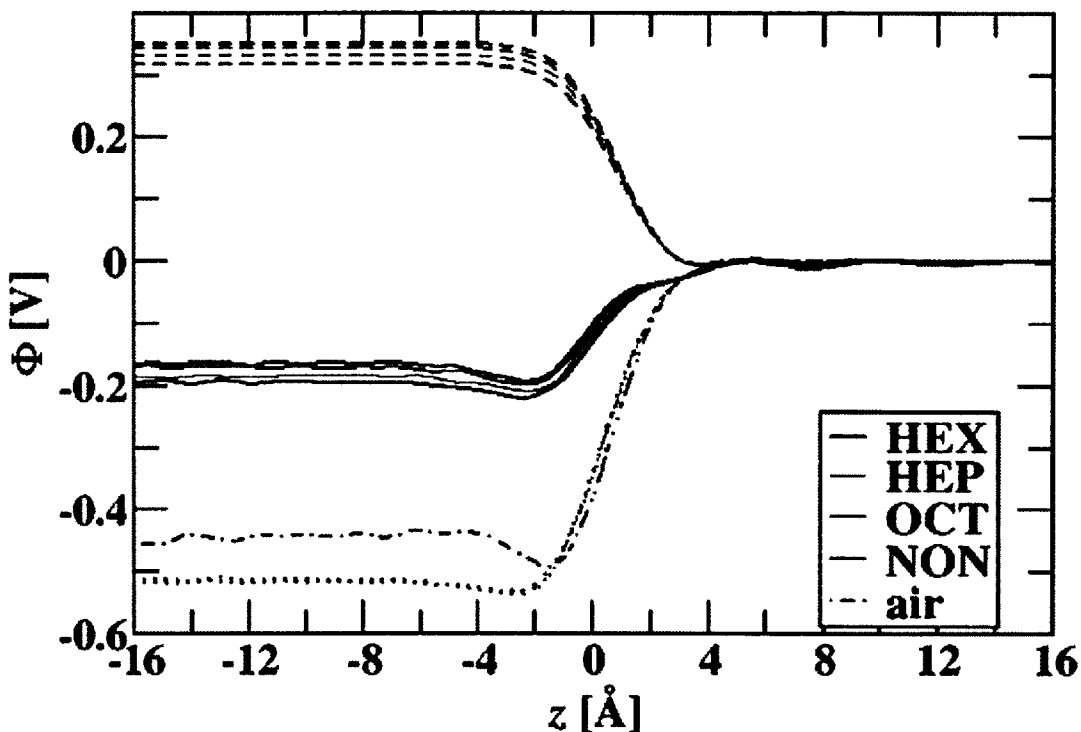


**Figure 5-9:** Electrostatic potential as a function of position for the whole system (solid lines), from water molecules alone (dotted lines), and from alkane molecules alone (dashed lines).

The surface potential itself is the value present at negative  $z$  values when a steady value is reached. A negative surface potential coincides with positive charge orienting towards the air and negative charge orienting towards the bulk.

The overall surface potential drop for the alkane/water systems is significantly reduced in comparison with the air/water interface, being around  $-0.18$  V for the alkane/water interfaces and  $-0.45$  V for the air/water. The  $-0.18$  V value compares with  $-0.38$  V obtained from a fluctuating charge model and  $-0.11$  V for a non-polarizable model [49]. These have been compared with experimental results for the potential

difference between water and a lipid bilayer of -0.4 to -0.6 V [170-171], which is greater in magnitude than the results shown here. However, a recent investigation has put to doubt the viability of making direct comparisons between simulation results and those with electrodes for surface potentials in systems without ions present [172]. On the other hand, surface potentials from simulations provide useful information on the orientation and induced dipoles of the species present. The electrostatic potential from the water structure alone shows a greater drop at the alkane/water interface than at the air/water interface. This is in contrast to what is observed for the total potential. However, the fact that the electrostatic potential from the alkane phase increases as the water phase is approached would create an electric field that should increase the orientation of water molecules. The observed increase in alkane surface potential is the result of an electric field with a negative charge pointing towards the alkane phase and a positive charge pointing towards the water phase. Water molecules should respond to this field by having greater orientational preference for their hydrogens pointing towards the alkane phase, which is indeed the result. The reason the alkane phase has the described electric field is because its hydrogens are positively charged and its carbons are negatively charged. Since the hydrogens surround the carbons, any alkane surface will contain a slight positive charge.

#### 5.4 Conclusions

This study looked at molecular dynamics simulations with polarizable potentials which were carried out to investigate different *n*-alkane/water interfaces. A new polarizable alkane model was developed for this work which gave good agreement with experiment for liquid densities, heats of vaporization, and alkane/water interfacial

tensions. No structural or interfacial differences were observed when the number of alkane carbons was odd versus even as has been found experimentally [47]. With higher alkane molecular weight, though, it was found that the interfacial width decreased in contrast to trends observed from x-ray reflectivity experiments [55, 59]. Furthermore, there was an expansion in water structure at the alkane/water interface, which was linked to a lower water induced dipole at the interface. However, the lower induced dipole and expanded structure at the alkane/water interface was not as significant as at the air/water interface. The alkane structure showed a contraction near the alkane/water interface, which was linked to larger alkane induced dipoles in this region.

## CHAPTER 6

# THE EFFECT OF ALKYL CHAIN LENGTH ON ALKANE/WATER INTERFACIAL WIDTH

### 6.1 Introduction

As aforementioned in this dissertation, a detailed understanding of alkane/water interfaces would greatly advance our understanding of the less studied hydrophobic/water interface which are linked to many important processes [4-6, 8, 60, 62-63]. Alkane/water interfaces are particularly important because their molecular structure can be easily modified by varying the length of the alkane chain and the degree of branching [4]. Because of this feature they are considered a prototypical system for studying the interaction of water with hydrophobic liquid surfaces [4]. The interfacial width of alkane/water interfaces are of interest to researcher because it may play a fundamental role in the ability of the interface to influence interfacial properties [4].

In this chapter we further examine the interfacial width, in an effort to clarify the results we obtained for interfacial width in our study in Chapter 5, which contradict with the finding of experimental results [46, 55, 59]. Previous experimental studies using x-ray reflectivity have found that the interfacial width may increase with *n*-alkane chain length [46, 55, 59]. However, our results in Chapter 5 show that the longer the *n*-alkane chain

length, the smaller the interfacial width [173]. In these studies, however, we explored the separate water and alkane interfacial widths which are based on specific densities while experiments are based on electron density and not the electron density [46, 55, 59]. Additionally, due to the finite size of the simulation system, it does not fully account for how capillary waves may influence interfacial width [174-178], which exist in reality and could potentially be the reason for the qualitative differences between the two results. In this study, the electron densities were extracted from simulation data and a structure factor was calculated based on them. This information was then used to make direct comparisons with experimental (x-ray reflectivity) data [179]. Also, in our interfacial width calculation, we accounted for the capillary wave action which is expected to cause broadening of the interfacial width.

Here we investigate whether qualitative agreement can be brought between our simulation results and x-ray reflectivity experiments for the effect of chain length on interfacial width. The studies are conducted using molecular dynamics simulations with polarizable interactions. We examined systems of *n*-hexane/water and *n*-nonane/water, and also investigated the effect of doubling the size of the alkane region, and quadrupling the entire system size.

## 6.2 Simulation Details

Water was simulated using the rigid Dang-Chang water model [70, 94], which has four sites, including a single Lennard-Jones (LJ) site at the oxygen atomic position. There are also partial positive charges at the hydrogen atomic positions, and both a negative partial charge and point polarizability located at an *m*-site, which is along the bisector of the oxygen-hydrogen bonds. Alkanes were simulated using a previously

developed polarizable model [173]: the model included LJ, point charges, and point polarizabilities on all atomic sites. The model had similar parameters (with differing charges) for the methyl and methylene carbons and the same parameters for all hydrogen atoms. The charges were taken from the OPLS-AA [180] force field, and all intramolecular bonded interactions (harmonic bond bending, dihedral potentials, and bond stretching) were taken from the GAFF force field [181]. Each atom had an associated point polarizability taken from the work of Applequist [182].

MD simulations were carried out for the alkane/water interfacial systems in the NpT ensemble, with the temperature (298 K) and pressure (1 atm) controlled by the Berendsen thermostat and barostat, respectively [136]. A total of six systems were investigated, which included two different types of *n*-alkanes: *n*-hexane and *n*-nonane. The smallest of the *n*-hexane/water interfacial system is denoted 1HEX and the smallest *n*-nonane-water system denoted 1NON, which both had 2000 water molecules and 200 *n*-alkane molecules. The approximate dimensions of these systems were  $36 \times 36 \times 80$  Å, with the 1NON system being somewhat longer in the *z*-dimension. Because the system was elongated in the *z*-dimension, two alkane/water interfaces formed bisecting the *z*-axis. Water occupied approximately 45 Å of the box while alkane occupied the remaining. A second type of system had 400 *n*-alkane water molecules and the same number of water molecules (2000), which is denoted 2HEX and 2NON. This particular system was more elongated in the *z*-dimension with the water phase the same size and the alkane phase twice as long in the *z*-dimension, but with the same approximate *x* and *y* dimensions. Finally, a third set of systems were simulated with 8000 water molecules and 800 *n*-alkane molecules, denoted 4HEX and 4NON. These systems had the same *z*-

dimension as the 1HEX and 1NON systems, but were replicated in the  $x$  and  $y$  dimensions, creating systems four times larger. As a result, the systems were twice as large in both the  $x$  and  $y$  dimensions. A total of 4 ns of production were carried out for each system, following extensive equilibration of at least 1 ns with a timestep of 1 fs. The alkane carbon-hydrogen bond lengths and the water geometries were kept rigid with the SHAKE and RATTLE algorithms [95]. A Lennard-Jones potential truncation of 12 Å was enforced with analytical tail corrections employed. Long-ranged electrostatics were handled with the particle mesh Ewald summation technique [96].

## **6.3 Results and Discussions**

### **6.3.1 Density Profiles**

Figure 6-1 shows the density profiles for the different alkane/water systems with zero representing the Gibbs dividing surface (GDS) of water.

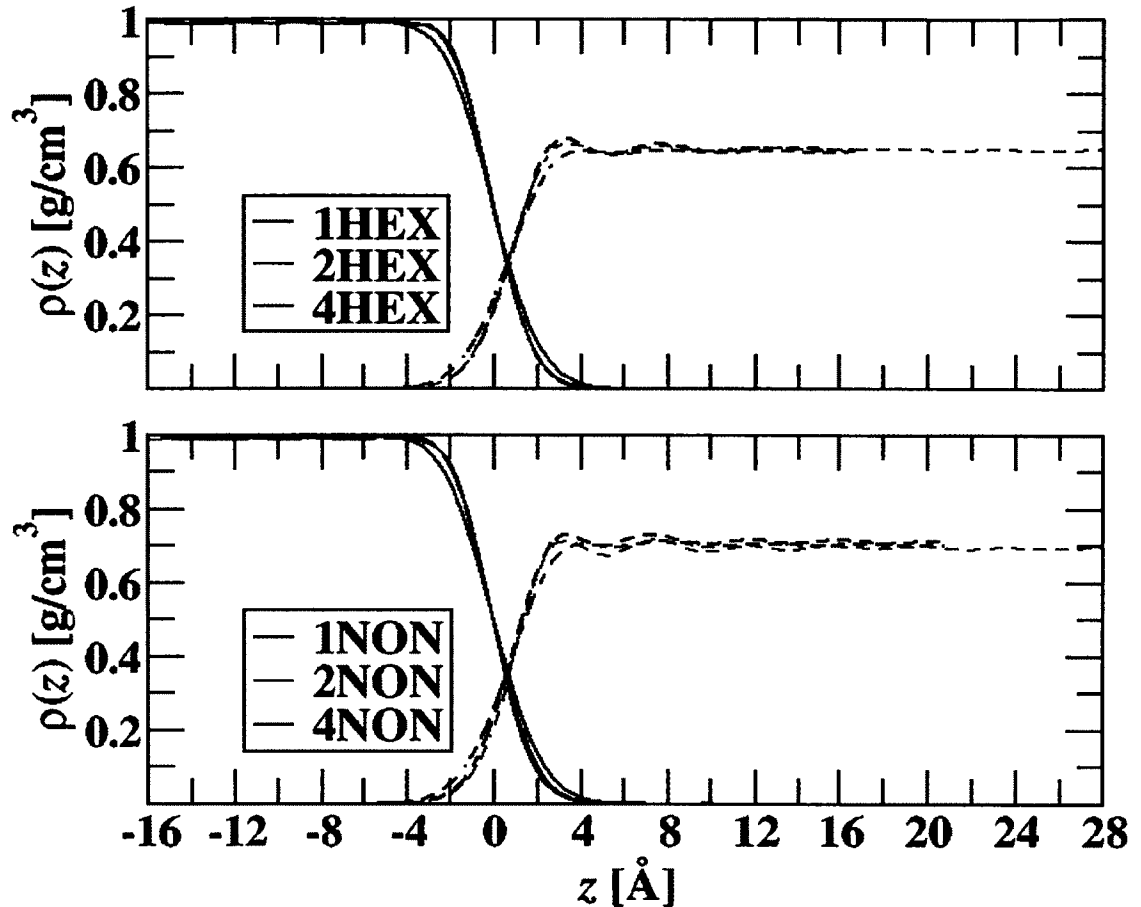


**Figure 6-1:** Density profiles for water (solid lines) and alkanes (dashed lines) for the systems described. The GDS for the water is represented as zero.

The GDS of the alkane phases are shifted to greater  $z$ -coordinate than the GDS of water, with the distance often being referred to as the intrinsic length. The experimental bulk densities for  $n$ -hexane and  $n$ -nonane are 0.654 and 0.718  $\text{g}/\text{cm}^3$  respectively [183], corresponding closely to the liquid densities away from the GDS. It can also be observed that the systems have very similar bulk densities despite the different system sizes, except the 2NON system has a slightly lower density than the 1NON and 4NON systems. This may be a systems size effect due to the interfacial width in the  $z$ -direction, but as can be observed it is rather small. There are density oscillations present near the interface for

the alkane phases, as described in our previous work [173]. We are particularly interested in how the different systems behave at the interface. While the 1HEX and 2HEX, along with the 1NON and 2NON systems have similar density oscillations at the interface, the 4HEX and 4NON systems behave quite differently, having much broader interfacial density profiles and smaller oscillations at the interface. They still have density oscillations in phase with those of the 1 and 2 sized systems, but they are much smaller. If we take a model of an intrinsic width, broadened by capillary waves, the interfacial width should become broader with a greater lateral boxlength [174-178] due to capillary waves, consistent with our results. This will be discussed in greater detailed later.

### 6.3.2 Electron Density Profiles and X-ray Reflectivity

To be able to make comparisons with experimental x-ray reflectivity experiments, the electron density needs to be computed [179, 184]. The total electron density was computed from the sum over the product of atomic number density  $n^i(z)$  along the surface normal direction multiplied by the atomic number,  $Z_i$  of each atomic species  $i$  [35, 179, 184]

$$\rho_e(z) = \sum_{i=1}^n n^i(z)Z_i \quad \text{Eq. 6-1}$$

The atomic density was calculated in a histogram with bins of 0.25 Å in length. The electron density profiles computed across the alkane/water interface for the different systems investigated are shown in Figure 6-2.

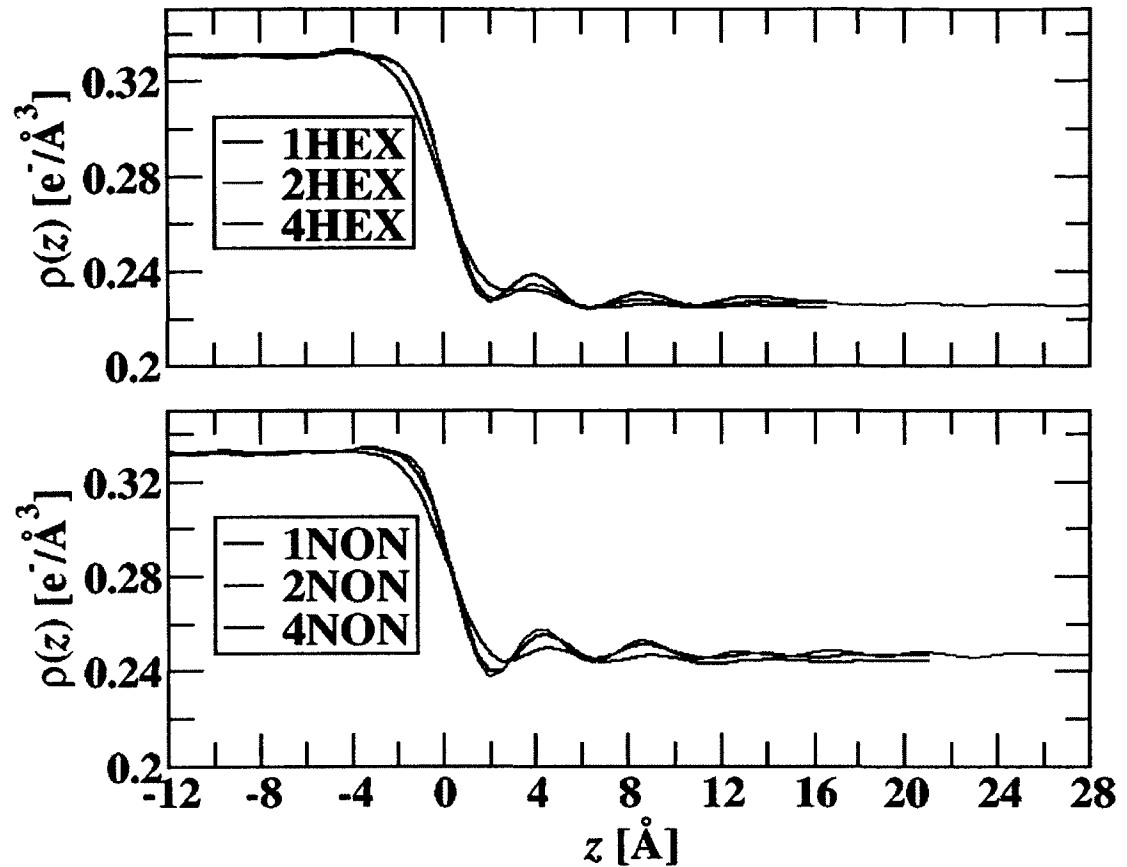


**Figure 6-2:** Electron density profiles for the *n*-alkane/water systems studied. The GDS for the water is represented as zero.

There are noticeable oscillations in the electron density profiles, just as in the specific density profiles, while the 4HEX and 4NON systems are more smeared out due to capillary waves. A simple model has been used for electron density to estimate the interfacial width of the alkane/water interface [10],

$$\langle \rho(z) \rangle = \frac{1}{2}(\rho_w + \rho_a) + \frac{1}{2}(\rho_w - \rho_a) \operatorname{erf}(z/\sigma\sqrt{2}), \quad \text{Eq. 6-2}$$

where  $\sigma$  is the interfacial width,  $\rho_w$  and  $\rho_a$  are the electron densities of the water and alkane phases, respectively. To be able to estimate the x-ray reflectivity, the structure

factor needs to be calculated by making the Fourier transform of the position dependent derivative of the electron density [35, 179, 184], [184]

$$\Phi(q_z) = \frac{1}{\rho_w} \int_{-\infty}^{\infty} \left[ \frac{d\rho_e(z)}{dz} \right] \exp(iq_z z) dz \quad \text{Eq. 6-3}$$

where  $\rho_w$  is the bulk electron density of water. This can be used to estimate the x-ray reflectivity [10],

$$R(q_z) = R_F(q_z) |\Phi(q_z)|^2 \quad \text{Eq. 6-4}$$

$$R(q_z) = R_F(q_z) \exp(-q_z q_z^T \sigma^2) \quad \text{Eq. 6-5}$$

where Eq. 6-5 is valid if the electron density follows Eq. 6-2,  $R_F(q_z)$  is the Fresnel reflectivity (reflectivity calculated for an ideal interface),  $\sigma$  is the interfacial width from Eq. 6.2, and  $q_z^T = \sqrt{q_z^2 - q_c^2}$  with  $q_c$  being the critical wave vector transfer for total reflection of the x-rays from the lower phase, which is defined in previous work [59]. If the electron density follows Eq. 6-2, a plot of  $\log[R(q_z)/R_F(q_z)]$  versus  $q_z q_z^T$  will yield a straight line with a slope of  $-\sigma^2$ .

The electron density profiles obtained from our simulation results can be used to calculate the reflectivity by utilizing Eq. 6-3 on the derivative of the electron density profile with respect to  $z$ -position. Then, the reflectivity can be calculated using Eq. 6-4 [35, 179, 184]. To make direct comparisons between simulation and experiment, a correction is required which will be described later, but it is instructive to compare the reflectivity of the raw simulation data. Figure 6-3 gives  $\log[R(q_z)/R_F(q_z)]$  versus  $q_z q_z^T$  for the systems investigated.

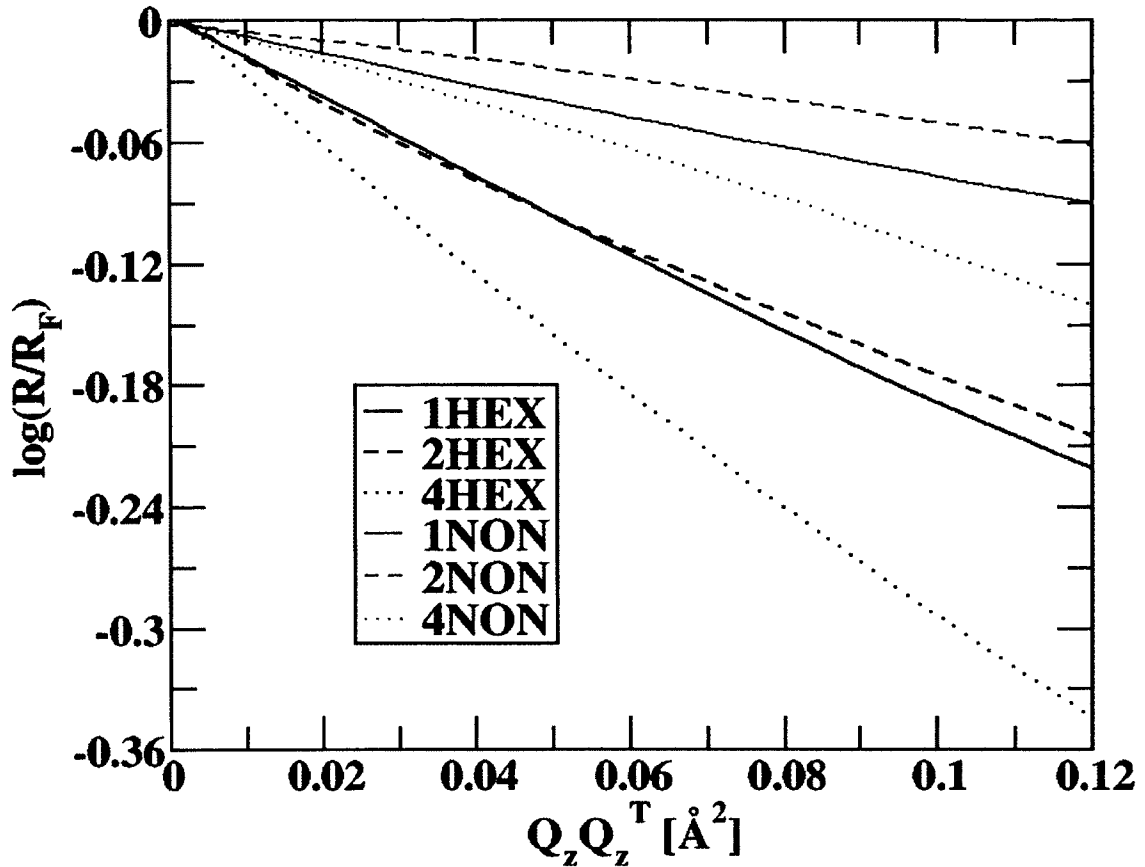


**Figure 6-3:** Logarithm of x-ray reflectivity, normalized to Fresnel reflectivity  $R_F(q_z^T)$ , as a function of  $q_z q_z^T$ , for the *n*-alkane/water systems obtained from the raw electron density data.

The slope of these lines coincides with  $-\sigma^2$ , assuming the electron density reasonably follows Eq. 6-2. Table 6-1 gives the value of  $\sigma$ , extracted from the slopes in Figure 6-3 under ‘Raw’. It can be observed that going from the 1 to the 4 sized systems, there is a significant increase in interfacial width, which is consistent with the specific density profiles in Figure 6-1. The 2 systems have a slightly smaller interfacial width than the 1 systems, showing some effect due to more alkane phase. However, it is clear that the interfacial width extracted from the simulated x-ray reflectivity is smaller for the NON systems than the corresponding HEX systems for all cases, in contrast to experiment [59].

**Table 6-1:** Interfacial Width in Å of the *n*-Alkane Water Systems Studied, Including a Fit to the Raw Data (Raw), the Values Extracted from Eq. 6.6 ( $\sigma_{cw}$ ), and the Results From a Fit to the Raw Data Convolved With a Gaussian of Width  $\sigma_{cw}$  (Conv). The uncertainties for all numbers were between 0.02 to 0.03 Å.

SYSTEM	Raw	$\sigma_{cw}$	Conv
1HEX	1.37	2.92	3.13
2HEX	1.32	2.92	3.12
4HEX	1.50	2.76	3.17
1NON	0.87	2.87	2.91
2NON	0.71	2.87	2.86
4NON	1.15	2.71	2.94

### 6.3.3 Capillary Wave Theory

As stated previously, the simulation data has to be corrected to make more direct comparisons with experiment. One of the most important corrections is to account for capillary waves, which increase the interfacial width. Capillary wave theory allows the estimation of the additional interfacial width due to capillary waves,  $\sigma_{cw}$ , beyond the box length [59]

$$\sigma_{cw} = \frac{k_B T}{2\pi^2 \gamma} \log\left(\frac{q_{max}}{q_{min}}\right). \quad \text{Eq. 6-6}$$

Where  $q_{max} = \pi/L_{||}$ , with  $L_{||}$  being the box length parallel to the interface, and  $q_{min} = (2\pi/\lambda)\Delta\beta\sin\alpha$ , where  $\lambda=0.825\text{Å}$ ,  $\Delta\beta=8.88\times 10^{-4}$ , and  $\alpha=0.94^\circ$  which gives a  $q_{min}$  value of  $\pi*3.53\times 10^{-5}$ . Also,  $k_B$  is the Boltzmann constant and  $\gamma$  is the interfacial tension. We used the interfacial tension calculated from the work in Chapter 5, which are very similar between *n*-hexane/water and *n*-nonane/water, but slightly higher for the *n*-nonane/water

system, as is found experimentally [162]. Table 6-1 gives the values extracted from Eq. 6-6 for  $\sigma_{cw}$ . For the 1HEX and 2HEX systems, the  $\sigma_{cw}$  are nearly identical, as can be observed for the 1NON and 2NON systems, since they have the same  $L_{||}$ . Furthermore, the  $\sigma_{cw}$  values are slightly smaller for the NON systems than their corresponding HEX systems due to the fact that the NON systems have a slightly higher interfacial tension, to which Eq. 6-6 shows  $\sigma_{cw}$  is inversely proportional.

In order to account for capillary wave contributions to the interfacial width, the electron density profile was convoluted with a Gaussian function with a standard deviation of  $\sigma_{cw}$ . A plot of  $\log (R(q_z)/R_F(q_z))$  against  $q_z q_z^T$  is shown in Figure 6-4 taken from this convoluted electron density, and the corresponding interfacial widths extracted from the slopes (denoted Conv) are given in Table 6-1.

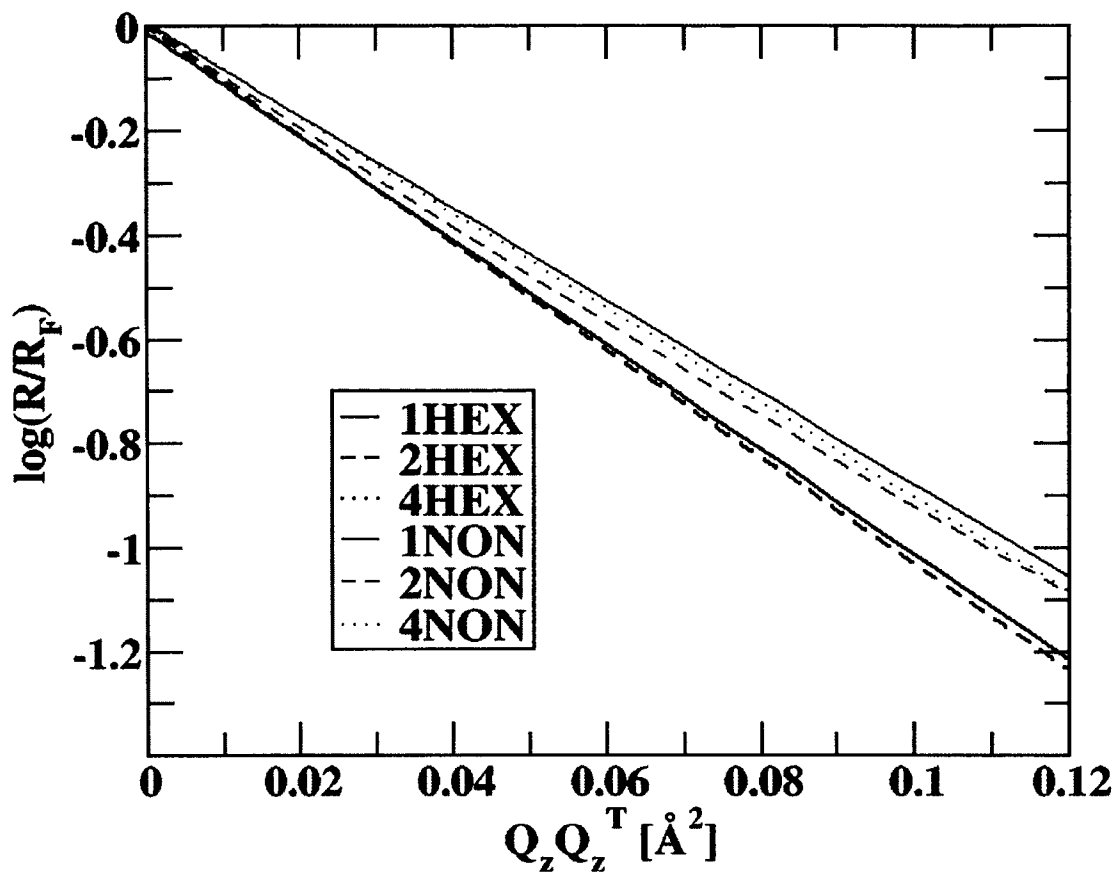


**Figure 6-4:** Logarithm of x-ray reflectivity, normalized to Fresnel reflectivity  $R_F(q_z^T)$ , as a function of  $q_z q_z^T$ , for the *n*-alkane/water systems obtained from the electron density data convoluted using the capillary wave theory.

It is clear that the slopes are much more negative in Figure 6-4 when compared to Figure 6-3. Consequently, the interfacial widths are significantly larger for the Conv results than the Raw results. It can also be observed that the Conv results for the 1HEX, 2HEX, and 4HEX are very similar, while those for the 1NON, 2NON, and 4NON systems are similar also. However, the interfacial widths for the NON systems are consistently smaller than for the HEX systems, showing no qualitative differences between the trends shown in the Conv and Raw results. To check the viability of the convolution strategy, we convoluted the 1HEX and 1NON systems with a Gaussian with a more narrow distribution to

account for doubling its  $L_{\parallel}$ . This was achieved by setting  $q_{\min} = \pi/L_{\parallel}$  with  $L_{\parallel}$  taken from the 4HEX and 4NON systems to convolute the 1HEX and 1NON systems respectively ( $L_{\parallel}$  for  $q_{\max}$  was taken from their respective 1HEX or 1NON box lengths). Then,  $\sigma_{\text{cw}}$  was extracted from Eq. 6-6 and the 1HEX and 1NON electron densities were convoluted with a Gaussian with this width. Convoluting the 1HEX and 1NON system, we estimated an interfacial width of 1.49 Å and 1.11 Å, respectively, which compares with the raw 4HEX and 4NON widths of 1.50 Å and 1.15 Å, respectively, showing reasonable agreement. Experimentally, the interfacial widths calculated for the *n*-hexane/water and *n*-nonane/water interfaces are 3.5 Å and 4.5 Å, respectively. We underestimate the interfacial width modestly for the HEX systems, but to a much more significant degree for the NON systems. It is clear that for the *n*-nonane/water interface, there is something missing from the comparison with experiment, which will be discussed later. It is not surprising that including results of capillary wave theory do not change the qualitative differences between the HEX and NON systems. The interfacial tension is greater for the NON system than the HEX system, which results in a smaller  $\sigma_{\text{cw}}$  for the NON system and thus a smaller Conv result.

#### 6.3.4 Distribution of Carbons

It is clear that the simulation results do not agree with the experimental results for the effect of longer *n*-alkane chain length on interfacial width, even with the correction for capillary waves. It should be noted, though, that since the simulation results investigate atoms and not electrons, there are potentially different electronic effects not taken into account in the simulations. To better understand the differences between the NON and HEX systems, we calculated the profile of the ratio of methyl to methylene

carbons for the different systems as a function of position. Figure 6-5 shows the distribution of the ratio of methylene versus methyl carbons of the systems studied. Both the HEX and NON systems have higher methylene ratios near the interface than in the bulk.

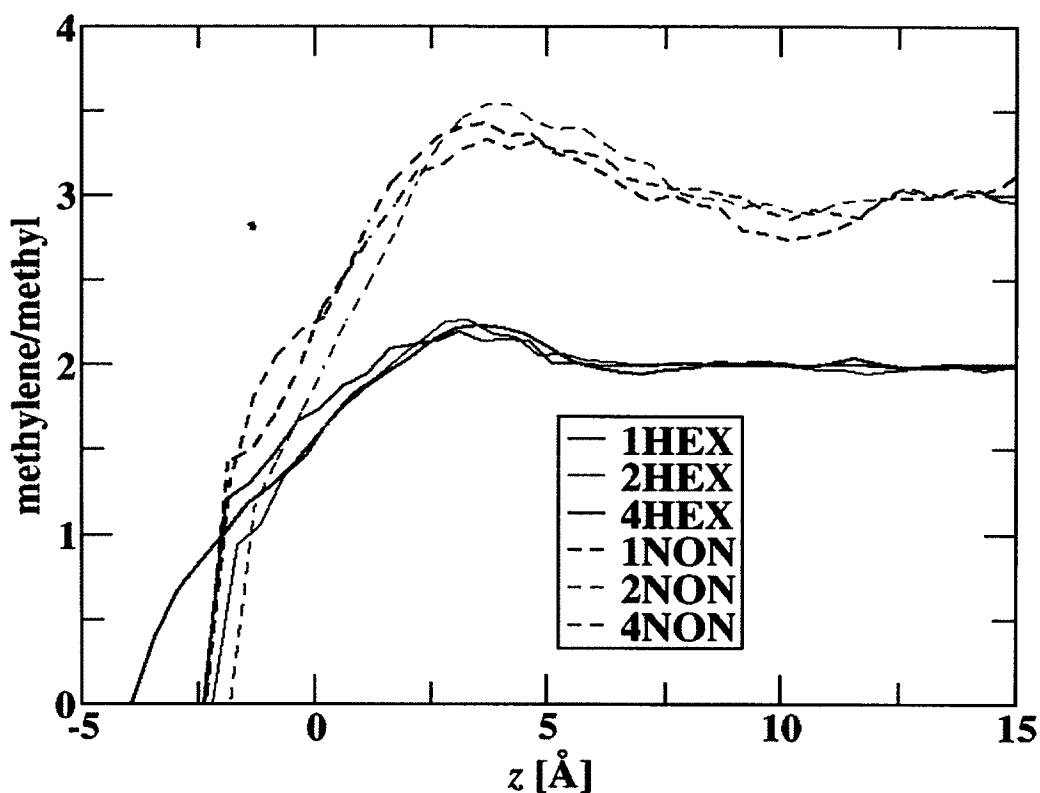


**Figure 6-5:** The distribution of methylene carbons compare to methyl carbons in the *n*-hexane-water (solid lines) and *n*-nonane-water (dashed lines) systems studied. The GDS for the water is represented as zero

It is interesting to observe that the NON systems have higher methylene ratios over a much broader range than the HEX systems. In fact the NON systems do not reach bulk ratios until around 7.5 Å from the GDS, while the HEX systems reach bulk values around 6 Å from the GDS. This shows that for a true bulk region, 6 Å to 7.5 Å away from the GDS has to be reached, pointing to a fairly large interfacial region. The electron distribution surrounding methyl groups will be somewhat different than that surrounding

methylene groups. Furthermore, unlike protons and neutrons, which the atomic density profiles show, electrons are somewhat smeared over a region of space. This smearing may affect how the electrons distribute in a system. To gauge this better, we carried out DFT calculations of *n*-hexane with the m06 functional [185] and the aug-cc-pvdz basis set and created a Gaussian cube electron density profile with a grid size of 0.1 Å in each dimension carried out with the NWChem package [186]. Using the cube file, the electron density surrounding each atom as a function of distance was calculated. Figure 6-6 gives the electron density as a function of distance from the atomic center of methyl and methylene carbons and hydrogens. Both types of hydrogens behave in a similar manner.

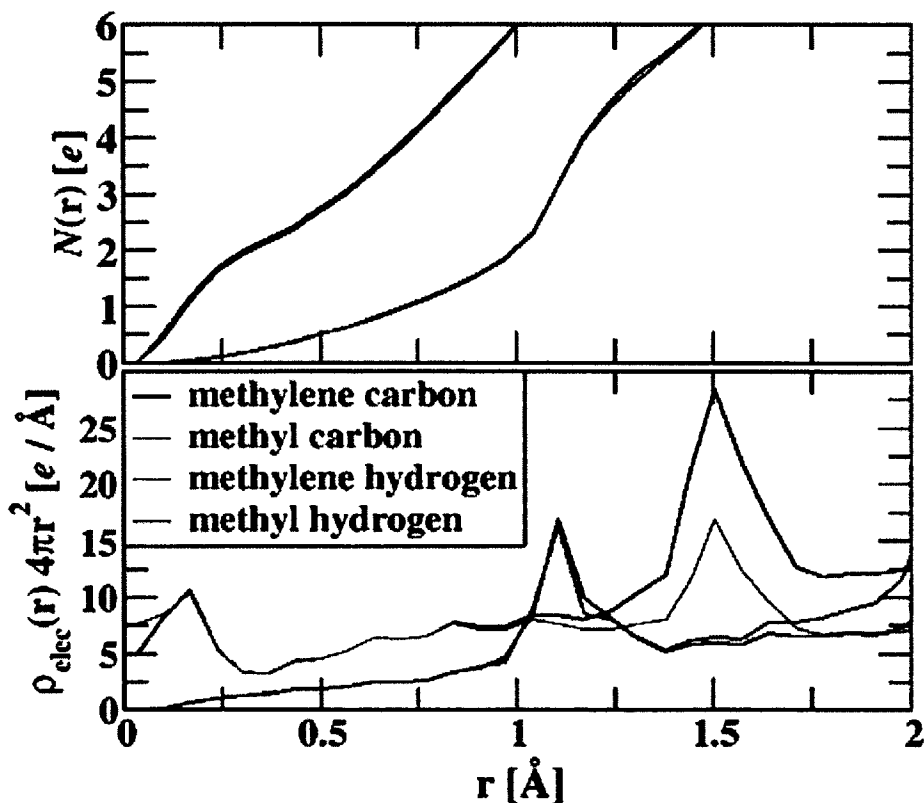


**Figure 6-6:** The electron density of methyl and methylene carbons and hydrogens (bottom) and integral of these electron density profiles (top) as a function of distance from the atom centers

There is a peak just greater than 1 Å corresponding to the carbon position. Methyl and methylene carbons have very similar electron density profiles also with only small differences. The integral of these profiles as a function of distance from the atom centers are also given in Figure 6-6. Hydrogens have one electron, and the integral for all hydrogens reaches one at 0.75 Å, while carbons contain 6 electrons, in which the integral reaches six at 1.0 Å. These could be used to slightly smear the electron density profiles in Figure 6-2, but they had no impact on the qualitative differences between the *n*-hexane/water and *n*-nonane/water systems (results not shown). There are other aspects that may influence the electron density, for instance, intermolecular charge transfer. We carried out *ab initio* calculations with the same level of theory as described previously for a single propane molecule with a water molecule. Using the ESP charges, we calculated a molecular charge of 0.03 for propane and -0.03 for water, showing some intermolecular charge transfer, but again small in comparison to the total atomic charges. There may be other effects of electron density in solution, and the only way to account for them would be to carry out *ab initio* molecular dynamics simulations of the alkane/water interface, as has been carried out for the air/water interface [187].

#### **6.4 Conclusion and Future Work**

In this study, we examined systems of *n*-hexane/water and *n*-nonane/water using molecular dynamics simulations to investigate how the alkyl chain length affects the interfacial width of *n*-alkane/water systems. The electron density profile across the *n*-alkane/water interface was calculated and used and estimated the resulting reflectivity. Our simulation results found the opposite trend to experiment. We found that as the *n*-alkane chain length increases, the interfacial width decreases, while experiment finds that

the interfacial width increases. Corrections to the electron density to account for capillary waves had no significant impact on our qualitative results. Our results also showed that methylene carbons are more likely to be found in a region near the interface than in the bulk, and that the *n*-nonane/water interface has a much broader region of methylene enhancement. Ultimately, our molecular dynamics simulations simulate atoms and atomic densities, while experiment investigates electrons. This difference may be why there are disagreements between simulation and experiment, although investigating electron density surrounding methyl and methylene carbons and hydrogens with gas phase *ab initio* calculations of *n*-hexane found little difference between methyl and methylene atoms.

## CHAPTER 7

# A COMPARISON OF IONS AT THE AIR/ WATER AND *N*-ALKANE/WATER INTERFACES

### 7.1 Introduction

As discussed in earlier chapters of this dissertation, to better understand a wide range of chemical, industrial, biological and other processes it is necessary to understand the similarities and differences between air/water and hydrophobic/water interfaces. We know that interfacial water behaves in a different manner than bulk water. However, we do not have a thorough understanding of how the specific type of interface influences the behavior of aqueous species. Previous work has found that different hydrophobic/water interfaces may influence ion distributions in a different manner than the air/water interface [33, 67]. However, the only investigation of the behavior of ions at the alkane/water interface was carried out without polarizable potentials [68]. Including polarizability in the molecular model has been found to be particularly important when studying the behavior of ions at aqueous interfaces [28-32, 69].

In this chapter we attempt to fill part of this void with a comparison of molecular dynamics studies conducted at the air/water and alkane/water interfaces in the presence of

different ionic species (sodium chloride, sodium bromide and sodium iodide). In this study, molecular dynamics simulations with polarizable potentials were carried out to investigate the sodium-halide ion distributions. Sodium-halide concentrated solutions at the *n*-octane/water interface were simulated and compared to the air/water interface.

## 7.2 Simulation Details

### 7.2.1 Molecular Models

Polarizable molecular models were used for all simulations. For water, the rigid Dang-Chang (D-C) water model was used, which is a 4-site model with a single Lennard-Jones (LJ) site located at the oxygen atomic position. Also, there are partial positive charges located on the water hydrogen positions, and an *m*-site located along the oxygen-hydrogen bisector that has a partial negative charge and a point polarizability [70]. Polarizable ions were used in some simulations, which included single atomic sites with a LJ interaction, integer charge, and point polarizability [25]. A new alkane force field was developed for this work which is discussed in more detail in Chapter 6. The model included LJ, point charges, and point polarizabilities on all atomic sites. The charges were taken from the OPLS-AA force field [158], and all intramolecular bonded interactions (harmonic bond bending, dihedral potentials, and bond stretching) were taken from the GAFF force field [159]. Each atom had a point polarizability, which were taken from the work of Applequist [160].

### 7.2.2 Simulation Details

The interfacial alkane/water systems simulated consisted of 2000 water molecules and 200 *n*-octane molecules. Furthermore, 36 NaX ion pairs were added to the *n*-

octane/water (OCT) system, having three systems, NaCl, NaBr, and NaI with aqueous concentrations of 1M. The interfacial systems were placed in rectangular boxes in which the  $x$  and  $y$  dimensions were shorter and identical at around 38 Å for all, while the  $z$  dimension was longer, and was around 80 Å. Due to the extended length in the  $z$  dimension, two octane/water interfaces formed in the systems bisecting the  $z$  axis. The octane/water systems were all simulated at 298K. Standard Lorentz-Berthelot combining rules were used for the LJ interactions (geometric mean for  $\epsilon$  and the arithmetic mean for  $\sigma$ ). A potential truncation of 12 Å was enforced with analytic tail corrections, and the particle mesh Ewald summation technique used to calculate long-ranged electrostatic interactions [96]. The point polarizabilities allow induced dipoles to form at their positions. The determination of the magnitude for these dipoles is a many-body problem, in which self-consistent procedures are often used. For the described work, the always stable predictor corrector algorithm was used, which requires only one evaluation of energy per timestep [124]. A 5ns production was used with uncertainties calculated from 500 ps blocks, all of these after extensive equilibration. The air/water systems used here as a comparison were taken from previous work by Wick and Dang [33].

### 7.3 Results and Discussions

Figure 7-1 gives the density profiles of NaCl, NaBr, and NaI at the OCT and air/water interfaces with zero representing the GDS of water.

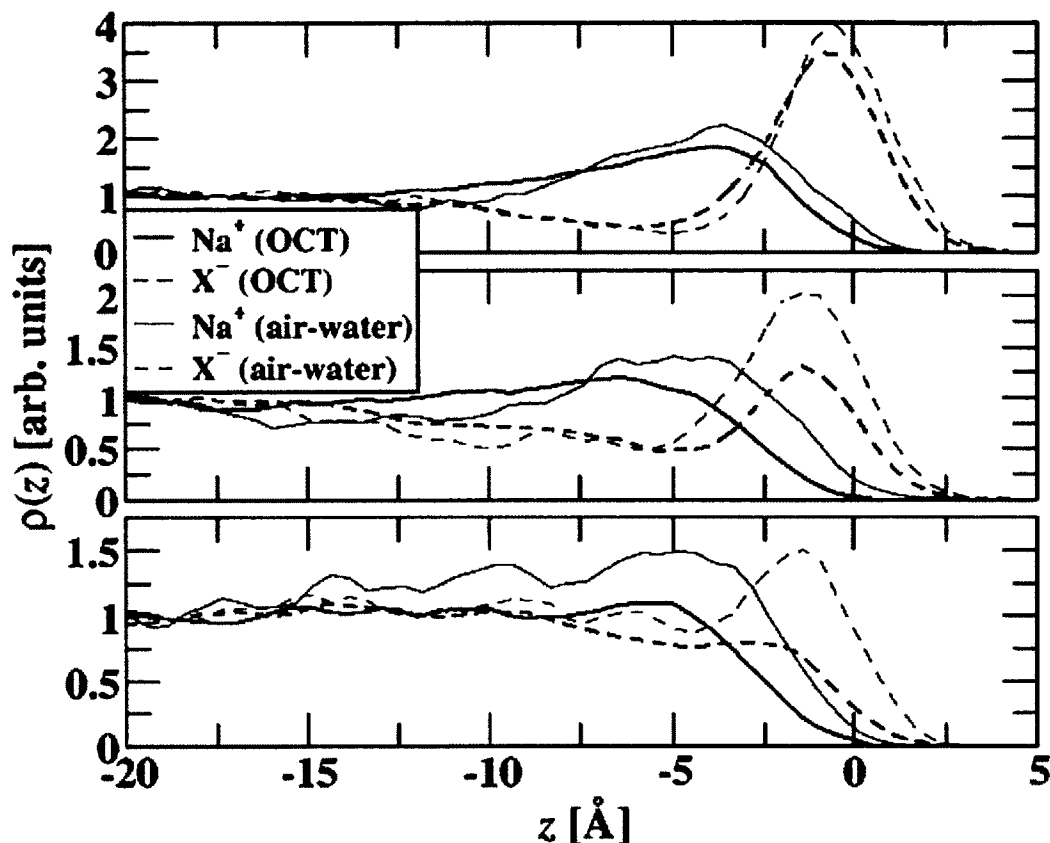


**Figure 7-1:** Distribution of NaX ions as a function of position for the OCT system and the air/water interface with  $\text{X}^-$  being chloride (bottom figure), bromide (middle figure), and iodide (top figure).

The results from the air/water interface were taken from previous work done by Wick and Dang [33], and all density profiles are scaled to be 1 for their bulk density. At the air/water interface, all anions show a propensity for the air/water interface. At the OCT interface, though, chloride is repelled from the interface, while bromide has a lower interfacial concentration than at the air/water interface. Iodide shows similar interfacial concentrations at the air/water and OCT interfaces, while the iodide is somewhat lower at the OCT interface.

In a plot of the electrostatic potential (not shown here) there is a significantly smaller drop at the octane/water interfaces than at the air/water interface. The

electrostatic potential pictured here, was discussed in more detail in Chapter 5 which includes a more detailed view of the electrostatic potential of different alkane/water systems and is pictured in Figure 5-9. A drop in electrostatic potential means that there is an electric dipole with its positive pole pointing away from bulk water. This should cause ions to form a double layer in response to this electric field in an opposite manner: positive charge towards the bulk and negative charge towards the air or organic. This can be seen in the density profiles shown in Figure 7-1. Since the potential drop is greater for the air/water interface, this effect would be expected to be bigger at the air/water than the organic/water interfaces, and is consistent with the density profiles for NaBr and NaCl. For NaI, though, this effect is not as strong, as there is little difference in interfacial iodide concentrations between the air/water and OCT systems. Iodide is the most hydrophobic of the anions, so it would be expected that it would have potentially favorable interactions with the alkane phase, especially considering that the positive pole of the iodide dipole is pointing towards the alkane phase. This will cancel the electrostatic interaction from the negative charge of iodide to a degree in this region, which should increase the hydrophobicity of this region.

The interfacial tensions of the NaX solutions are shown in Table 7-1, in which NaCl increases the interfacial tension, NaBr increases it, but within the statistical uncertainty, and NaI decreases the interfacial tension.

**Table 7-1:** Showing a comparison of the Simulation and Experimental Interfacial Tensions

<b>SYSTEM</b>	<b>Simulation</b>	<b>Experiment<sup>[162]</sup></b>
<b>OCT</b>	48.9±1.1	50.7
<b>NaCl</b>	52.7±0.7	N/A
<b>NaBr</b>	50.2±0.8	N/A
<b>NaI</b>	47.3±0.9	N/A

To our knowledge, no experimental results are given for the effect of NaX salts on alkane/water interfacial tension, but examples of the influence of alkali-halides on the interfacial tensions of other aqueous/hydrophobic interfaces have been measured. For instance, NaCl has been shown to increase the interfacial tension of water-lysozyme interfaces, NaBr shown to slightly decrease it, and NaI shown to moderately decrease the interfacial tension [188]. Furthermore, KCl has been shown to increase the interfacial tension of the water-dekalin and water-*n*-dodecane interfaces, while KI has been shown to decrease it [189-190]. These are in contrast with the air/water interface, in which NaCl, NaBr, NaI, KCl, KBr, and KI increase its surface tension [157, 190-191]. These experimental results are consistent with our simulation results, showing iodide reduces the interfacial tension, showing mild sorption to the aqueous-hydrophobic interface, while chloride increases the surface tension, showing similar behavior as at the air/water interface. It should also be noted that a degree of sorption to the interface can correspond to a negative surface tension increment, which has been discussed in detail elsewhere [11, 143, 192]. Chapter 4 of this dissertation is a detailed molecular dynamics simulation study of the effect of NaCl, NaBr, and NaI on the surface tension and excess of the

air/water interface. In that study, we found correlation between our simulation and experimental surface excess. Results of this study suggested that sodium chloride cause the greatest surface tension increase while sodium iodide caused the smallest increase in surface tension.

#### 7.4 Conclusions

This chapter detailed molecular dynamics simulations with polarizable potentials which were carried out to investigate the *n*-octane/water interfaces. A new polarizable alkane model was developed for this work which gave good agreement with experiment for liquid densities, heats of vaporization, and alkane/water interfacial tensions. These are discussed in more detail in Chapter 5. NaCl, NaBr, and NaI ion distributions at the *n*-octane-water interface were compared with the air/water interface. Chloride was repelled from the *n*-octane-water interface, even though it has a propensity for the air/water interface. Bromide's interfacial concentration was significantly reduced at the *n*-octane-water interface in comparison with the air/water interface, while iodide had similar concentrations at both interfaces. The behavior of iodide was attributed to favorable hydrophobic interactions between iodide and alkanes that was not present for the more hydrophilic bromide and chloride anions.

## **APPENDIX A**

### **THE WATER MODEL**

## A.1 The Water Model

Water models are used in the molecular simulation of liquid water and aqueous solutions. Water models can be divided into three main types:

- (1) Simple Interaction-site Models: in this situation each water molecule is maintained in a rigid geometry and the model relies on non-bonded interactions. The pairwise Coulombic expression describes electrostatic interactions and Lennard-Jones expressions describe dispersion and repulsion forces (explained in Chapter 2) [193].
- (2) Flexible Models: in these models, internal changes in the conformation of the molecule are allowed.
- (3) Polarizable Models: models that have been developed to explicitly include the effects of polarization and many body effects.

A variety of models exist; they can be classified by the number of points used to define the model (atoms plus dummy sites), whether the structure is rigid or flexible, and whether the model includes polarization effects [2].

### A.1.1 The Simple Interaction-site Models

These models usually have between three and six interaction sites and rigid water geometry.

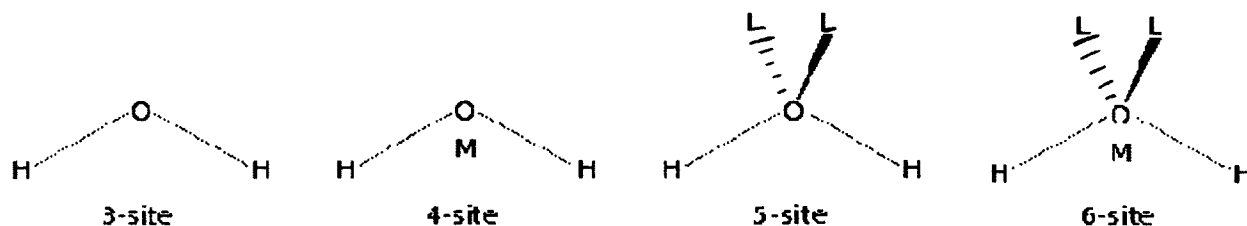


**Figure A-1:** Snapshot of the possible geometries for the rigid water model ranging from three to six interaction sites

Three-site models have three interaction sites, corresponding to the three atoms of the water molecule. Each atom gets assigned a point charge, and the oxygen atom also gets the Lennard-Jones parameters. The 4-site models place the negative charge on a dummy atom (labeled  $M$  in the figure) placed near the oxygen along the bisector of the HOH angle. This improves the electrostatic distribution around the water molecule. The 5-site models place the negative charge on dummy atoms (labeled  $L$ ) representing the lone pairs of the oxygen atom, with a tetrahedral-like geometry. A 6-site model that combines all the sites of the 4- and 5-site models was developed by Nada and van der Eerden [194]. Flexibility is usually included in a model by “grafting” bond-stretching and angle-bending terms onto the potential function for a rigid model.

### A.2 The Dang-Chang Water Model

The Dang-Chang Water Model is a rigid polarizable model used for the many of the studies in this dissertation [70, 94]. The Dang-Chang water model has *four* sites, including a single Lennard-Jones site at the oxygen atomic position, partial positive charges at the hydrogen atomic positions, and both a negative partial charge and point polarizability located at the  $M$ -site, which is along the bisector of the oxygen-hydrogen bonds.

### A.3 The Flexible Water Model

The previously developed flexible water model was also used for studies included in this dissertation and is described in detail elsewhere [119]. In summary, the water model included four interaction sites with a van der Waals site located on the oxygen atomic position, and partial positive charges located on the hydrogen atomic positions. There was another  $M$ -site located along the oxygen-hydrogen bond bisector that included

a point polarizability and partial negative charge. The electrostatic charges themselves were dependent on the geometry of the water molecules, with a larger bond angle and long bond lengths corresponding to a more positive hydrogen charge.

## **APPENDIX B**

### **EXPLANATION OF TERMINOLOGY**

## B.1 SHAKE and RATTLE

The SHAKE algorithm is designed for use with the Verlet integrators while the RATTLE algorithm is formulated for use with the velocity Verlet integrator [88]. The SHAKE algorithm [195] has become the standard approach for doing molecular dynamics (integrating the equations of motion) with fixed bond lengths. This algorithm can also be used to hold angles fixed, however, this practice is less common. SHAKE is a modification of the Verlet algorithm for integrating the equations of motion for the Cartesian coordinates degrees of freedom in a molecular system. Atomic velocities are first calculated for the unconstrained system then modified to meet each constraint. An iterative process is required to meet all the constraints concurrently [196]. The SHAKE algorithm works well for systems with timesteps of up to 5 fs. This in turn enables a speedup in computational time as long as the process of iteratively solving the constraint equations does not consume too much time [2].

The RATTLE algorithm is similar to SHAKE and calculates the positions and velocities at the next time from the positions and velocities at the present time step, without requiring information about the earlier history. RATTLE guarantees that the coordinates and velocities of the atoms in a molecule satisfy the internal constraints (bond lengths and angles) at each time step. RATTLE has two advantages over SHAKE. It provides higher precision than SHAKE on computers of fixed precision. And since it deals directly with the velocities, it is easier to modify RATTLE for use with the recently developed NVT and NpT molecular dynamics methods like the ones addressed in this dissertation [197].

## B.2 Potential Mean Force (PMF)

When looking at our simulation results, we may be interested in examining the manner in which the free energy changes as a function of intermolecular or intramolecular coordinates. These can range from the distance between two atoms to the torsion angle of a bond within a molecule. The free energy surface along a specific coordinate is referred to as the potential mean force (PMF) [2]. Various methods have been proposed for calculating potentials of mean force. The simplest method of calculating the PMF is the free energy change as the separation between two particles change. One way to calculate the PMF is by using the radial distribution function and the following expression from Helmholtz free energy [2]:

$$A(r) = -k_B T \ln g(r) + \text{constant} \quad \text{Eq. B-1}$$

The constant is often chosen so that the most probable distribution corresponds to a free energy of zero. The primary drawback of employing this method is that molecular dynamics simulations often do not sample regions where the radial distribution function differs drastically from the most likely value. This can then result in inaccurately calculated potential mean force.

Similarly, the PMF, which is essentially the free energy, can be defined from the average distribution function  $P(r)$  as [198],

$$A(r) = -k_B T \ln P(r) + \text{constant} \quad \text{Eq. B-2}$$

where the average distribution function along the coordinate  $r$  is obtained from a Boltzmann weighted average. It is usually impractical to compute the PMF or the distribution function directly from a MD simulation. As a result, special techniques like umbrella sampling are used to calculate the PMF from molecular dynamics results.

Umbrella sampling is a method used to overcome the sampling problem. The potential function is modified so that unfavorable states are sampled sufficiently. This method can be effectively used with molecular dynamics simulations, which are employed in this dissertation [2]. The modified (biased) potential energy function can be written as [198],

$$V'(\mathbf{r}^N) = V(\mathbf{r}^N) + W(\mathbf{r}^N) \quad \text{Eq. B-3}$$

where  $W(\mathbf{r}^N)$  is a weighting function which often takes the form:

$$W(\mathbf{r}^N) = k_W(\mathbf{r}^N - \mathbf{r}_0^N)^2. \quad \text{Eq. B-4}$$

The biased distribution function is given by:

$$\langle P(\mathbf{r}^N) \rangle = e^{-W(\mathbf{r}^N)/k_B T} \langle P(\mathbf{r}^N) \rangle (e^{-W(\mathbf{r}^N)/k_B T})^{-1}. \quad \text{Eq. B-5}$$

In order to obtain the PMF over a range for a number of biased simulations are performed at different intervals (windows). These results at these different windows are then unbiased and combined to obtain the final PMF,  $A(r)$ .

### **B.3 Potential Truncation and Analytical Tail Corrections**

The interactions between pairs or atoms or molecules that are separated by large distances can typically be truncated. These approximations are only appropriate for *non-bonded* interaction and can never be used for *bonded* interactions. Many non-bonded pairwise potentials decay rapidly with separation distance which allows us to ignore interactions between pairs of atoms or molecules that are separated by large distances. For instance, with the Lennard-Jones (LJ) potential initial described in Section 2.6.1:

$$v(r) = 4\varepsilon \left[ \left( \frac{\sigma}{r} \right)^{12} - \left( \frac{\sigma}{r} \right)^6 \right] \quad \text{Eq. B-6}$$

A typical cutoff distance is  $2.5\sigma$  beyond which the potential is chosen to be zero .

Truncating pair interactions systematically removes a contribution to the overall potential energy and pressure. For moderate cutoffs, such as  $2.5\sigma$  for the LJ system, this contribution can constitute a nontrivial fraction of the totals. For interactions that are cut but not shifted (another possibility that is not detailed here) the interactions beyond  $2.5\sigma$  can be approximately added back into the total energy expression.

$$U_{total} = U_{pair} + U_{tail} \quad \text{Eq. B-7}$$

Where  $U_{tail}$  is the tail correction, and can be evaluated analytically [199].

#### B.4 Particle Mesh Ewald Summation Technique

Electrostatic energy consist of both short range and long range interactions. The Lennard-Jones potential decays strongly with distance (as  $r^{-5}$ ), which allows us to cut off the interaction at moderate distances and if desired add a correction factor in molecular simulations. Coulomb interactions, on the other hand, decay much slower (as  $r^{-1}$ ) and as a result, a correction factor cannot be computed. This causes the results of the calculation of electrostatics to diverge in molecular simulations. One of the most common methods used to deal with the long range electrostatic interactions is the Ewald Summation method [2]. The Ewald summation method splits the electrostatics into two portions, where the short range electrostatic interactions are summed in “real-space” and the long range electrostatic interactions are summed in “Fourier-space”. Generally, Ewald summation can be represented as:

$$E_{electrostatics} = \sum_{i,j} [short\ range(real\ space) + long\ range(fourier\ space)] \quad \text{Eq. B-8}$$

The particle mesh Ewald summation which is used in the simulations detailed in this dissertation is a modification of the Ewald summation. The particle mesh Ewald summation replaces the direct summation of short range and long range electrostatic

interactions with two summations, a direct summation of short range interactions in space and a summation of the long range interactions in Fourier space represented as:

$$E_{electrostatics} = \sum_{i,j} [short\ range(real\ space)] + \sum [long\ range(fourier\ space)] \quad \mathbf{Eq. B-9}$$

## BIBLIOGRAPHY

- [1] D. M. J. Grotendorst, A. Muramatsu, "Quantum simulations of complex many-body systems: from theory to algorithms," in *NIC Series* vol. 10, ed Jülich: Johnvon Neumann Institute for Computing, 2002, pp. pp. 211-254.
- [2] A. R. Leach, *Molecular Modelling: Principles and Applications*: Prentice Hall, 2001.
- [3] P. B. Balbuena and J. M. Seminario, *Molecular Dynamics: from Classical to Quantum Methods*: Elsevier, 1999.
- [4] M. G. Brown, *et al.*, "Vibrational sum-frequency spectroscopy of alkane/water interfaces: Experiment and theoretical simulation," *Journal of Physical Chemistry B* vol. 107, pp. 237-244, 2003.
- [5] D. S. Walker, *et al.*, "Evidence for a diffuse interfacial region at the dichloroethane/water interface," *Journal of Physical Chemistry B*, vol. 108, pp. 2111-2114, Feb 2004.
- [6] D. S. Walker, *et al.*, "Vibrational sum frequency spectroscopy and molecular dynamics simulation of the carbon tetrachloride-water and 1,2-dichloroethane-water interfaces," *Journal of Physical Chemistry C*, vol. 111, pp. 6103-6112, Apr 2007.
- [7] V. S. J. Craig, *et al.*, "The effect of electrolytes on bubble coalescence in water," *The Journal of Physical Chemistry*, vol. 97, pp. 10192-10197, 1993.
- [8] A. Chakma, "Interfacial phenomena in petroleum recovery, edited by Norman R. Morrow, 1991, Marcel Dekker Inc., New York, Book Review," *The Canadian Journal of Chemical Engineering*, vol. 71, pp. 493-494, 1993.
- [9] O. T. Cummings and C. D. Wick, "Computational study of cation influence on anion propensity for the air–water interface," *Chemical Physics Letters*, vol. 500, pp. 41-45, 2010.
- [10] D. M. Mitrinovic, *et al.*, "X-ray reflectivity study of the water–hexane interface," *The Journal of Physical Chemistry B*, vol. 103, pp. 1779-1782, 1999.

- [11] P. Jungwirth and D. J. Tobias, "Specific ion effects at the air/water interface," *Chemical Reviews*, vol. 106, pp. 1259-1281, Apr 2006.
- [12] T. L. Majewski J Fau - Kuhl, *et al.*, "X-ray and neutron surface scattering for studying lipid/polymer assemblies at the air-liquid and solid-liquid interfaces," *Journal of Biotechnology* vol. 74, pp. 207-31, 2000.
- [13] C. D. Wick, "NaCl dissociation dynamics at the air-water interface," *The Journal of Physical Chemistry C*, vol. 113, pp. 2497-2502, 2009.
- [14] S. McLaughlin, "The electrostatic properties of membranes," *Annu Rev Biophys Chem*, vol. 18, pp. 113-36, 1989.
- [15] B. H. Honig, *et al.*, "Electrostatic interactions in membranes and proteins," *Annual Review of Biophysics and Biophysical Chemistry*, vol. 15, pp. 163-193, 1986.
- [16] E. M. Knipping, *et al.*, "Experiments and simulations of ion-enhanced interfacial chemistry on aqueous NaCl aerosols," *Science*, vol. 288, pp. 301-306, 2000.
- [17] W. R. Haag and C. C. David Yao, "Rate constants for reaction of hydroxyl radicals with several drinking water contaminants," *Environmental Science and Technology*, vol. 26, pp. 1005-1013, 1992.
- [18] J. Vande Vondele and M. Sprik, "A molecular dynamics study of the hydroxyl radical in solution applying self-interaction-corrected density functional methods," *Physical Chemistry Chemical Physics*, vol. 7, pp. 1363-1367, 2005.
- [19] M. Roeselová, *et al.*, "Hydroxyl radical at the air-water interface," *Journal of the American Chemical Society*, vol. 126, pp. 16308-16309, 2004.
- [20] Y. Xie and H. F. Schaefer Iii, "Hydrogen bonding between the water molecule and the hydroxyl radical ( $\text{H}_2\text{O} \cdot \text{HO}$ ): The global minimum," *The Journal of Chemical Physics*, vol. 98, pp. 8829-8834, 1993.
- [21] M. Roeselová, *et al.*, "Impact, trapping, and accommodation of hydroxyl radical and ozone at aqueous salt aerosol surfaces. A molecular dynamics study," *Journal of Physical Chemistry B*, vol. 107, pp. 12690-12699, 2003.
- [22] I. Benjamin, "Theoretical study of ion solvation at the water liquid--vapor interface," *The Journal of Chemical Physics*, vol. 95, pp. 3698-3709, 1991.

- [23] K. Schweighofer and I. Benjamin, "Ion pairing and dissociation at liquid/liquid interfaces: Molecular dynamics and continuum models," *The Journal of Chemical Physics*, vol. 112, pp. 1474-1482, 2000.
- [24] P. Jungwirth and D. J. Tobias, "Ions at the air/water interface," *Journal Of Physical Chemistry B*, vol. 106, pp. 6361-6373, Jun 27 2002.
- [25] L. X. Dang, "Computational study of ion binding to the liquid interface of water," *Journal Of Physical Chemistry B*, vol. 106, pp. 10388-10394, Oct 10 2002.
- [26] T. M. Chang and L. X. Dang, "Recent advances in molecular simulations of ion solvation at liquid interfaces," *Chemical Reviews*, vol. 106, pp. 1305-1322, Apr 2006.
- [27] S. Ghosal, *et al.*, "Electron spectroscopy of aqueous solution interfaces reveals surface enhancement of halides," *Science*, vol. 307, pp. 563-566, Jan 28 2005.
- [28] B. L. Eggimann and J. I. Siepmann, "Size effects on the solvation of anions at the aqueous liquid-vapor interface," *The Journal of Physical Chemistry C*, vol. 112, pp. 210-218, 2007.
- [29] M. Fyta, *et al.*, "Ionic force field optimization based on single-ion and ion-pair solvation properties," *The Journal of Chemical Physics*, vol. 132, pp. 024911-10, 2010.
- [30] P. Jungwirth and D. J. Tobias, "Chloride anion on aqueous clusters, at the air-water interface, and in liquid water: solvent effects on Cl<sup>-</sup> polarizability," *The Journal of Physical Chemistry A*, vol. 106, pp. 379-383, 2001.
- [31] L. X. Dang and T.-M. Chang, "Molecular mechanism of ion binding to the liquid/vapor interface of water," *The Journal of Physical Chemistry B*, vol. 106, pp. 235-238, 2001.
- [32] P. Jungwirth and D. J. Tobias, "Specific ion effects at the air/water interface," *Chemical Reviews*, vol. 106, pp. 1259-1281, 2005.
- [33] C. D. Wick and L. X. Dang, "Recent advances in understanding transfer ions across aqueous interfaces," *Chemical Physics Letters*, vol. 458, pp. 1-5, 2008.
- [34] G. L. Warren and S. Patel, "Comparison of the solvation structure of polarizable and nonpolarizable ions in bulk water and near the aqueous liquid-vapor interface," *Journal of Physical Chemistry C*, vol. 112, pp. 7455-7467, 2008.

- [35] X. Sun, *et al.*, "Computational studies of aqueous interfaces of SrCl<sub>2</sub> salt solutions," *The Journal of Physical Chemistry B*, vol. 113, pp. 13993-13997, 2009.
- [36] V. P. Sokhan and D. J. Tildesley, "The free surface of water: molecular orientation, surface potential and nonlinear susceptibility," *Molecular Physics*, vol. 92, pp. 625-640, Nov 1997.
- [37] H. Wang, *et al.*, "Polarity of liquid interfaces by second harmonic generation spectroscopy," *Journal of Physical Chemistry A*, vol. 101, p. 713, 1997.
- [38] G. L. Richmond, "Molecular bonding and interactions at aqueous surfaces as probed by vibrational sum frequency spectroscopy," *Chemical Reviews*, vol. 102, pp. 2693-2724, Aug 2002.
- [39] Q. Du, *et al.*, "Vibrational spectroscopy of water at the vapor water interface," *Physical Review Letters*, vol. 70, pp. 2313-2316, Apr 1993.
- [40] E. A. Raymond and G. L. Richmond, "Probing the molecular structure and bonding of the surface of aqueous salt solutions," *Journal Of Physical Chemistry B*, vol. 108, pp. 5051-5059, Apr 22 2004.
- [41] S. Gopalakrishnan, *et al.*, "Vibrational spectroscopic studies of aqueous interfaces: Salts, acids, bases, and nanodrops," *Chemical Reviews*, vol. 106, pp. 1155-1175, Apr 2006.
- [42] P. B. Petersen and R. J. Saykally, "On the nature of ions at the liquid water surface," in *Annual Review of Physical Chemistry* vol. 57, ed, 2006, pp. 333-364.
- [43] K. B. Eisenthal, "Second harmonic spectroscopy of aqueous nano- and microparticle interfaces," *Chemical Reviews*, vol. 106, pp. 1462-1477, 2006.
- [44] Y. R. Shen and V. Ostroverkhov, "Sum-frequency vibrational spectroscopy on water interfaces: polar orientation of water molecules at interfaces," *Chemical Reviews*, vol. 106, pp. 1140-1154, 2006.
- [45] M. A. Wilson, *et al.*, "Surface-potential of the water liquid vapor interface," *Journal Of Chemical Physics*, vol. 88, pp. 3281-3285, Mar 1 1988.
- [46] M. L. Schlossman, "X-ray scattering from liquid-liquid interfaces," *Physica B: Condensed Matter*, vol. 357, pp. 98-105, 2005.

- [47] J. C. Conboy, *et al.*, "Studies of alkane/water interfaces by total internal reflection second harmonic generation," *Journal of Physical Chemistry* vol. 98, pp. 9688-9692, 1994.
- [48] C. S. Tian and Y. R. Shen, "Structure and charging of hydrophobic material/water interfaces studied by phase-sensitive sum-frequency vibrational spectroscopy," *Proceedings of the National Academy of Sciences of the United States of America*, vol. 106, pp. 15148-15153, 2009.
- [49] S. A. Patel and C. L. Brooks III, "Revisiting the hexane-water interface via molecular dynamics simulations using nonadditive alkane-water potentials," *Journal of Chemical Physics* vol. 124, 2006.
- [50] D. Michael and I. Benjamin, "Solute orientational dynamics and surface roughness of water/hydrocarbon interfaces," *Journal of Physical Chemistry* vol. 99, pp. 1530-1536, 1995.
- [51] J. Chowdhary and B. M. Ladanyi, "Water/hydrocarbon interfaces: Effect of hydrocarbon branching on single-molecule relaxation," *Journal of Physical Chemistry B* vol. 112, pp. 6259-6273, 2008.
- [52] F. Bresme, *et al.*, "Intrinsic structure of hydrophobic surfaces: The oil-water interface," *Physical Review Letters* vol. 101, 2008.
- [53] J. P. Nicolas and N. R. de Souza, "Molecular dynamics study of the n-hexane--water interface: Towards a better understanding of the liquid--liquid interfacial broadening," *The Journal of Chemical Physics*, vol. 120, pp. 2464-2469, 2004.
- [54] J. L. Rivera, *et al.*, "Molecular simulations of liquid-liquid interfacial properties: Water-n-alkane and water-methanol-n-alkane systems," *Physical Review E - Statistical, Nonlinear, and Soft Matter Physics*, vol. 67, pp. 116031-1160310, 2003.
- [55] M. L. Schlossman, "Liquid-liquid interfaces: Studied by X-ray and neutron scattering," *Current Opinion in Colloid and Interface Science* vol. 7, pp. 235-243, 2002.
- [56] C. Miqueu, *et al.*, "Simultaneous application of the gradient theory and Monte Carlo molecular simulation for the investigation of methane/water interfacial properties," *The Journal of Physical Chemistry B*, vol. 115, pp. 9618-9625, 2011/08/11 2011.
- [57] F. Biscay, *et al.*, "Adsorption of n-alkane vapours at the water surface," *Physical Chemistry Chemical Physics* vol. 13, pp. 11308-11316, 2011.

- [58] L. F. Scatena and G. L. Richmond, "Orientation, hydrogen bonding, and penetration of water at the organic/water interface," *Journal Of Physical Chemistry B*, vol. 105, pp. 11240-11250, Nov 15 2001.
- [59] D. M. Mitrinović, *et al.*, "Noncapillary-wave structure at the water-alkane interface," *Physical Review Letters* vol. 85, pp. 582-585, 2000.
- [60] A. R. van Buuren, *et al.*, "A molecular dynamics study of the decane/water interface," *The Journal of Physical Chemistry*, vol. 97, pp. 9206-9212, 1993/09/01 1993.
- [61] A. Chakma, "Interfacial phenomena in petroleum recovery, edited by Norman R. Morrow, 1991, 449 +viii pages, Marcel Dekker Inc., New York. ISBN: 0-8247-8385-9. Price: US \$125.00," *The Canadian Journal of Chemical Engineering*, vol. 71, pp. 493-494, 1993.
- [62] H. Freiser, "Metal complexation at the liquid-liquid interface," *Chemical Reviews* vol. 88, p. 611, 1988.
- [63] C. M. Starks, *et al.*, *Phase Transfer Catalysis*. New York: Chapman and Hall, 1994.
- [64] C. L. McFearin and G. L. Richmond, "The unique molecular behavior of water at the chloroform-water interface," *Applied Spectroscopy* vol. 64, pp. 986-994, 2010.
- [65] P. Srivastava, *et al.*, "Odd-even variations in the wettability of n-alkanethiolate monolayers on gold by water and hexadecane: A molecular dynamics simulation study," *Langmuir*, vol. 21, pp. 12171-12178, 2005.
- [66] G. M. Florio, *et al.*, "Chain-length effects on the self-Assembly of short 1-bromoalkane and n-alkane monolayers on graphite," *The Journal of Physical Chemistry C*, vol. 112, pp. 18067-18075, 2008.
- [67] C. L. McFearin and G. L. Richmond, "The role of interfacial molecular structure in the adsorption of ions at the liquid - liquid interface," *Journal of Physical Chemistry C*, vol. 113, pp. 21162-21168, 2009.
- [68] S. Pal and F. Müller-Plathe, "Molecular dynamics simulation of aqueous NaF and NaI solutions near a hydrophobic surface," *Journal of Physical Chemistry B* vol. 109, pp. 6405-6415, 2005.
- [69] L. Vrbka, *et al.*, "Propensity of soft ions for the air/water interface," *Current Opinion In Colloid & Interface Science*, vol. 9, pp. 67-73, Aug 2004.

- [70] L. X. Dang and T. M. Chang, "Molecular dynamics study of water clusters, liquid, and liquid-vapor interface of water with many-body potentials," *Journal Of Chemical Physics*, vol. 106, pp. 8149-8159, May 15 1997.
- [71] C. D. Wick and G. K. Schenter, "Critical comparison of classical and quantum mechanical treatments of the phase equilibria of water," *Journal of Chemical Physics*, vol. 124, Mar 2006.
- [72] C. D. Wick and L. X. Dang, "Molecular dynamics study of ion transfer and distribution at the interface of water and 1,2-dichlorethane," *Journal of Physical Chemistry C*, vol. 112, pp. 647-649, 2008.
- [73] R. D. Levine and R. B. Bernstein, *Molecular Reaction Dynamics and Chemical Reactivity*: Oxford University Press, 1987.
- [74] M. Karplus and J. A. McCammon, "Molecular dynamics simulations of biomolecules," *Nature Structural and Molecular Biology*, vol. 9, pp. 646-652, 2002.
- [75] L. Verlet, "Computer "experiments" on classical fluids. I. thermodynamical properties of Lennard-Jones molecules," *Physical Review*, vol. 159, pp. 98-103, 1967.
- [76] L. Verlet, "Computer "experiments" on classical fluids. II. equilibrium correlation functions," *Physical Review*, vol. 165, pp. 201-214, 1968.
- [77] W. C. Swope, *et al.*, "A computer simulation method for the calculation of equilibrium constants for the formation of physical clusters of molecules: Application to small water clusters," *The Journal of Chemical Physics*, vol. 76, pp. 637-649, 1982.
- [78] D. A. McQuarrie, *Statistical Mechanics*: University Science Books, 2000.
- [79] F. Schwabl, *Statistical mechanics*: Springer, 2006.
- [80] B. Widom, *Statistical Mechanics: A Concise Introduction for hCemists*: Cambridge University Press, 2002.
- [81] T. L. Hill, *Statistical Mechanics: Principles and Selected Applications*: Dover Publications, 1987.
- [82] D. F. Styer. (2007). *Statistical Mechanics*. Available: <http://www.oberlin.edu/physics/dstyer/StatMech/book.pdf>
- [83] D. Frenkel and B. Smit, *Understanding Molecular Simulation: from Algorithms to Applications*: Academic Press, 1996.

- [84] H. J. C. Berendsen, *et al.*, "Molecular dynamics with coupling to an external bath," *The Journal of Chemical Physics*, vol. 81, pp. 3684-3690, 1984.
- [85] H. Ehrenreich and D. Turnbull, *Solid State Physics: Advances in Research and Applications*: Academic Press, 1987.
- [86] M. P. Allen and D. J. Tildesley, *Computer Simulation of Liquids*: Clarendon Press, 1989.
- [87] G. Gompper and M. Schick, *Soft matter: Lipid bilayers and red blood cells*: Wiley-VCH, 2008.
- [88] S. I. Sandler, *An Introduction to Applied Statistical Thermodynamics*: John Wiley & Sons, 2010.
- [89] W. D. Cornell, *et al.*, "A second generation force field for the simulation of proteins, nucleic acids, and organic molecules," *Journal of the American Chemical Society*, vol. 117, pp. 5179-5197, 1995.
- [90] S. P. Parker, *McGraw-Hill Dictionary of Scientific and Technical Terms*: McGraw-Hill, 2003.
- [91] C. D. Wick, *et al.*, "The Effect of polarizability for understanding the molecular structure of aqueous interfaces," *Journal of Chemical Theory and Computation*, vol. 3, pp. 2002-2010, 2007.
- [92] C. D. Wick and S. S. Xantheas, "Computational investigation of interfacial and bulk chloride and iodide first solvation shell aqueous structure," *Journal of Physical Chemistry B* vol. 113, pp. 4141-4146, 2009.
- [93] J. Kolafa, "Gear formalism of the always stable predictor-corrector method for molecular dynamics of polarizable molecules," *The Journal of Chemical Physics*, vol. 122, p. 164105, 2005.
- [94] L. X. Dang, *et al.*, "Gibbs ensemble Monte Carlo simulations of coexistence properties of a polarizable potential model of water," *Journal Of Chemical Physics*, vol. 117, pp. 3522-3523, Aug 15 2002.
- [95] J. P. Ryckaert, *et al.*, "Numerical-integration of cartesian equations of motion of a system with constraints - molecular dynamics of n-alkanes," *Journal Of Computational Physics*, vol. 23, pp. 327-341, 1977.
- [96] U. Essmann, *et al.*, "A smooth particle mesh Ewald method," *Journal Of Chemical Physics*, vol. 103, pp. 8577-8593, Nov 15 1995.

- [97] C. D. Wick and L. X. Dang, "Computational observation of enhanced solvation of the hydroxyl radical with increased NaCl concentration," *Journal Of Physical Chemistry B*, vol. 110, pp. 8917-8920, May 11 2006.
- [98] B. T. Thole, "Molecular polarizabilities calculated with a modified dipole interaction," *Chemical Physics* vol. 59, pp. 341-350, 1981.
- [99] M. Masia, *et al.*, "On the performance of molecular polarization methods. II. Water and carbon tetrachloride close to a cation," *Journal of Chemical Physics* vol. 123, pp. 164505(1-13), 2005.
- [100] W. H. Press, *et al.*, *Numerical Recipes in Fortran*. Cambridge: Cambridge University Press, 1992.
- [101] G. M. Torrie and J. P. Valleau, "Nonphysical sampling distributions in Monte Carlo free-energy estimation: Umbrella sampling," *Journal of Computational Physics*, vol. 23, p. 187, 1977.
- [102] D. E. Smith and L. X. Dang, "Computer simulations of NaCl association in polarizable water," *The Journal of Chemical Physics*, vol. 100, p. 3757, 1994.
- [103] C. D. Wick and L. X. Dang, "Computational investigation of the influence of organic-aqueous interfaces on NaCl dissociation dynamics," *Journal of Chemical Physics* vol. 132, p. 044702, 2010.
- [104] C. D. Wick and L. X. Dang, "The behavior of NaOH at the air-water interface: A computational study," *The Journal of Chemical Physics*, vol. 133, pp. 024705-8, 2010.
- [105] L. X. Dang and T. M. Chang, "Molecular mechanism of ion binding to the liquid/vapor interface of water," *Journal Of Physical Chemistry B*, vol. 106, pp. 235-238, Jan 17 2002.
- [106] P. Wang, *et al.*, "Modeling surface tension of concentrated and mixed-solvent electrolyte systems," *Industrial & Engineering Chemistry Research*, vol. 50, pp. 4086-4098, 2011.
- [107] R. D'Auria and D. J. Tobias, "Relation between surface tension and ion adsorption at the air-water interface: A molecular dynamics simulation study," *Journal of Physical Chemistry A*, vol. 113, pp. 7286-7293, 2009.
- [108] Z.-B. Li, *et al.*, "Surface tension model for concentrated electrolyte aqueous solutions by the Pitzer equation," *Industrial & Engineering Chemistry Research*, vol. 38, pp. 1133-1139, 1999.

- [109] Y. Marcus, "Surface tension of aqueous electrolytes and ions," *Journal of Chemical & Engineering Data*, vol. 55, pp. 3641-3644, 2010.
- [110] E. W. Washburn, Ed., *International Critical Tables of Numerical Data, Physics, Chemistry and Technology (1st Electronic Edition)*. Knovel, 2003
- [111] S. Hård and K. Johansson, "The surface tension of concentrated aqueous solutions of 1:1-electrolytes measured by means of Wilhelmy and laser light scattering methods," *Journal of Colloid and Interface Science*, vol. 60, pp. 467-472, 1977.
- [112] A. Heydweiller, "Über physikalische Eigenschaften von Lösungen in ihrem Zusammenhang. II. Oberflächenspannung und elektrisches Leitvermögen wässriger Salzlösungen," *Annalen der Physik*, vol. 338, pp. 145-185, 1910.
- [113] T. Ishiyama and A. Morita, "Molecular dynamics study of gas-liquid aqueous sodium halide interfaces. I. flexible and polarizable molecular modeling and interfacial properties," *The Journal of Physical Chemistry C*, vol. 111, pp. 721-737, 2006.
- [114] J. Song and M. W. Kim, "Excess charge density and its relationship with surface tension increment at the air-electrolyte solution interface," *The Journal of Physical Chemistry B*, vol. 115, pp. 1856-1862, 2011.
- [115] J. Sala, *et al.*, "The polarizable point dipoles method with electrostatic damping: Implementation on a model system," *Journal of Chemical Physics* vol. 133, 2010.
- [116] E. Guardia, *et al.*, "On ion and molecular polarization of halides in water," *Journal of Chemical Theory and Computation*, vol. 5, pp. 1449-1453, 2009.
- [117] M. Masia, "Ab initio based polarizable force field parametrization," *Journal of Chemical Physics* vol. 128, p. 184107, 2008.
- [118] C. D. Wick, "Electrostatic dampening dampens the anion propensity for the air-water interface," *Journal of Chemical Physics* vol. 131, p. 084715, 2009.
- [119] C. D. Wick, "Hydronium behavior at the air-water interface with a polarizable multistate empirical valence bond model," *Journal of Physical Chemistry C*, vol. 116, pp. 4026-4038, 2012.
- [120] G. S. Fanourgakis and S. S. Xantheas, "The bend angle of water in ice Ih and liquid water: The significance of implementing the nonlinear

monomer dipole moment surface in classical interaction potentials," *Journal of Chemical Physics*, vol. 124, p. 174504, May 2006.

- [121] C. D. Wick and L. X. Dang, "Investigating hydroxide anion interfacial activity by classical and multistate empirical valence bond molecular dynamics simulations," *The Journal of Physical Chemistry A*, vol. 113, pp. 6356-6364, 2009.
- [122] C. Hättig and B. A. Heß, "TDMP2 calculation of dynamic multipole polarizabilities and dispersion coefficients for the halogen anions F-, Cl-, Br- and I," *Journal of Chemical Physics* vol. 108, pp. 3863-3870, 1998.
- [123] G. D. Mahan, "Modified Sternheimer equation for polarizability," *Physical Review A*, vol. 22, pp. 1780-1785, 1980.
- [124] J. Kolafa, "Time-reversible always stable predictor-corrector method for molecular dynamics of polarizable molecules," *Journal of Computational Chemistry*, vol. 25, pp. 335-342, 2004.
- [125] C. J. Burnham, *et al.*, "The parametrization of a Thole-type all-atom polarizable water model from first principles and its application to the study of water clusters (n=2-21) and the phonon spectrum of ice Ih," *Journal of Chemical Physics*, vol. 110, p. 4566, 1999.
- [126] R. W. Zwanzig, "High-temperature equation of state by a perturbation method .1. nonpolar gases," *Journal of Chemical Physics*, vol. 22, pp. 1420-1426, 1954.
- [127] B. Hess, *et al.*, "Osmotic coefficients of atomistic NaCl (aq) force fields," *Journal of Chemical Physics* vol. 124, 2006.
- [128] I. Kalcher and J. Dzubiella, "Structure-thermodynamics relation of electrolyte solutions," *Journal of Chemical Physics* vol. 130, 2009.
- [129] Y. Luo and B. Roux, "Simulation of osmotic pressure in concentrated aqueous salt solutions," *Journal of Physical Chemistry Letters*, vol. 1, pp. 183-189, 2010.
- [130] A. Ben-Naim, *Statistical Thermodynamics for Chemists and Biochemists*, 1992.
- [131] J. G. Kirkwood and F. P. Buff, "The statistical mechanical theory of solutions. i," *The Journal of Chemical Physics*, vol. 19, pp. 774-777, 1951.

- [132] S. Weerasinghe and B. M. Pettitt, "Ideal chemical potential contribution in molecular dynamics simulations of the grand canonical ensemble," *Molecular Physics* vol. 82, pp. 897-912, 1994.
- [133] S. Weerasinghe and P. E. Smith, "A Kirkwood-Buff derived force field for sodium chloride in water," *Journal of Chemical Physics* vol. 119, pp. 11342-11349, 2003.
- [134] M. B. Gee, *et al.*, "A Kirkwood-Buff derived force field for aqueous alkali halides," *Journal of Chemical Theory and Computation*, vol. 7, pp. 1369-1380, 2011.
- [135] S. Weerasinghe and P. E. Smith, "A Kirkwood-Buff derived force field for the simulation of aqueous guanidinium chloride solutions," *Journal of Chemical Physics* vol. 121, pp. 2180-2186, 2004.
- [136] H. J. C. Berendsen, *et al.*, "Molecular-dynamics with coupling to an external bath," *Journal Of Chemical Physics*, vol. 81, pp. 3684-3690, 1984.
- [137] D. A. Case, *et al.*, in *Amber 10*, ed. San Francisco: University of California, 2008.
- [138] Y. Marcus, *Ion Solvation*. New York: John Wiley and Sons Ltd., 1985.
- [139] T. L. Beck, "The influence of water interfacial potentials on ion hydration in bulk water and near interfaces," *Chemical Physics Letters* 2013.
- [140] D. E. Smith and L. X. Dang, "Interionic potentials of mean force for SrCl<sub>2</sub> in polarizable water. A computer simulation study," *Chemical Physics Letters* vol. 230, pp. 209-214, 1994.
- [141] L. X. Dang, *et al.*, "Understanding ion-ion interactions in bulk and aqueous interfaces using molecular simulations," *Faraday Discussions* vol. 160, pp. 151-160, 2013.
- [142] R. A. Robinson and R. H. Stokes, *Electrolyte Solutions*: Dover Publications, 1970.
- [143] R. D'Auria and D. J. Tobias, "Relation between surface tension and ion adsorption at the air-water interface: A molecular dynamics simulation study," *Journal of Physical Chemistry A* vol. 113, pp. 7286-7293, 2009.
- [144] O. T. Cummings and C. D. Wick, "Computational study of cation influence on anion propensity for the air-water interface," *Chemical Physics Letters* vol. 500, pp. 41-45, 2010.

- [145] K. A. Prather, *et al.*, "Bringing the ocean into the laboratory to probe the chemical complexity of sea spray aerosol," *Proceedings of the National Academy of Sciences*, April 25, 2013 2013.
- [146] M. Xu, *et al.*, "Water structure at the air–aqueous interface of divalent cation and nitrate solutions<sup>†</sup>," *The Journal of Physical Chemistry B*, vol. 113, pp. 4102-4110, 2009.
- [147] M. P. Allen and D. J. Tildesley, *Computer Simulation of Liquids*. Oxford: Oxford University Press, 1987.
- [148] P. Atkins and J. de Paula, *Atkins' Physical Chemistry, 5th ed.* Oxford, U.K.: University Press, 1994.
- [149] A. J. Lee and S. W. Rick, "The effects of charge transfer on the properties of liquid water," *Journal of Chemical Physics* vol. 134, p. 184507, 2011.
- [150] J. Korchowiec, *et al.*, "New energy partitioning scheme based on the self-consistent charge and configuration method for subsystems: Application to water dimer system," *Journal of Chemical Physics* vol. 112, pp. 1623-1633, 2000.
- [151] E. D. Glendening, "Natural energy decomposition analysis: Extension to density functional methods and analysis of cooperative effects in water clusters," *Journal of Physical Chemistry A* vol. 109, pp. 11936-11940, 2005.
- [152] R. Z. Khaliullin, *et al.*, "Electron donation in the water-water hydrogen bond," *Chemistry - A European Journal*, vol. 15, pp. 851-855, 2009.
- [153] O. Gálvez, *et al.*, "Variation with the intermolecular distance of properties dependent on the electron density in hydrogen bond dimers," *Journal of Chemical Physics* vol. 115, pp. 11166-11184, 2001.
- [154] P. O. Åstrand, *et al.*, "Atomic charges of the water molecule and the water dimer," *Journal of Physical Chemistry A* vol. 102, pp. 7686-7691, 1998.
- [155] C. D. Wick, *et al.*, "How intermolecular charge transfer influences the air-water interface," *Journal of Chemical Physics* vol. 137, 2012.
- [156] C. Wagner, *Physikalische Zeitschrift*, vol. 25, p. 474, 1924.
- [157] L. Onsager and N. N. T. Samaras, "The surface tension of debye-hückel electrolytes," *The Journal of Chemical Physics*, vol. 2, pp. 528-536, 1934.

- [158] W. L. Jorgensen, *et al.*, "Development and testing of the OPLS all-atom force field on conformational energetics and properties of organic liquids," *Journal of the American Chemical Society*, vol. 118, p. 11225, 1996.
- [159] J. Wang, *et al.*, "Development and testing of a general amber force field," *Journal of Computational Chemistry*, vol. 25, pp. 1157-1174, 2004.
- [160] Applequist, J, *et al.*, "Atom dipole interaction model for molecular polarizability - application to polyatomic-molecules and determination of atom polarizabilities," *Journal of the American Chemical Society*, vol. 94, pp. 2952-2960, 1972.
- [161] C. L. Yaws, *Chemical Properties Handbook*. New York: McGraw-Hill, 1999.
- [162] S. Zeppieri, *et al.*, "Interfacial tension of alkane + water systems," *Journal of Chemical and Engineering Data* vol. 46, pp. 1086-1088, 2001.
- [163] I. Benjamin, "Molecular structure and dynamics at liquid-liquid interfaces," *Annual Review of Physical Chemistry* vol. 48, pp. 407-451, 1997.
- [164] F. P. Buff, *et al.*, "Interfacial density profile for fluids in the critical region," *Physical Review Letters*, vol. 15, p. 621, 1965.
- [165] J. S. Rowlinson and B. Widom, *Molecular Theory of Capillarity*. New York: Oxford University Press, 1989.
- [166] K. R. Wilson, *et al.*, "Surface relaxation in liquid water and methanol studied by x-ray absorption spectroscopy," *Journal of Chemical Physics*, vol. 117, pp. 7738-7744, Oct 2002.
- [167] I. F. W. Kuo and C. J. Mundy, "An ab initio molecular dynamics study of the aqueous liquid-vapor interface," *Science*, vol. 303, pp. 658-660, Jan 2004.
- [168] I. F. W. Kuo, *et al.*, "Structure and dynamics of the aqueous liquid-vapor interface: A comprehensive particle-based simulation study," *Journal of Physical Chemistry B*, vol. 110, pp. 3738-3746, Mar 2006.
- [169] C. D. Wick, *et al.*, "Simulated surface potentials at the vapor-water interface for the KCl aqueous electrolyte solution," *Journal Of Chemical Physics*, vol. 125, p. 024706, Jul 14 2006.

- [170] V. L. Shapovalov, *et al.*, "Effect of gramicidin A on the dipole potential of phospholipid membranes," *Biophysical Journal*, vol. 77, pp. 299-305, 1999.
- [171] T. J. McIntosh, *et al.*, "Interbilayer interactions between sphingomyelin and sphingomyelin/cholesterol bilayers," *Biochemistry*<sup>®</sup>, vol. 31, pp. 2020-2024, 1992.
- [172] S. M. Kathmann, *et al.*, "Understanding the surface potential of water," *Journal of Physical Chemistry, B* vol. 115, pp. 4369-4377, 2011.
- [173] C. D. Wick, *et al.*, "Computational investigation of the n-alkane/water Interface with many-body potentials: the effect of chain length and ion distributions," *The Journal of Physical Chemistry C*, vol. 116, pp. 783-790, 2011.
- [174] D. K. Schwartz, *et al.*, "Thermal diffuse x-ray-scattering studies of the water-vapor interface," *Physical Review A*, vol. 41, pp. 5687-5690, 1990.
- [175] J. D. Weeks, "Structure and thermodynamics of the liquid-vapor interface," *The Journal of Chemical Physics*, vol. 67, pp. 3106-3121, 1977.
- [176] A. Braslau, *et al.*, "Capillary waves on the surface of simple liquids measured by x-ray reflectivity," *Physical Review A*, vol. 38, pp. 2457-2470, 1988.
- [177] A. Braslau, *et al.*, "Surface roughness of water measured by x-ray reflectivity," *Physical Review Letters* vol. 54, pp. 114-117, 1985.
- [178] M. L. Schlossman, in *Encyclopedia of Applied Physics*, G. L. Trigg, Ed., ed New York: VCH Publishers, 1997, p. 311.
- [179] E. Sloutskin, *et al.*, "The surface structure of ionic liquids: Comparing simulations with x-ray measurements," *The Journal of Chemical Physics*, vol. 125, pp. 174715-7, 2006.
- [180] W. L. Jorgensen, *et al.*, "Development and testing of the OPLS all-atom force field on conformational energetics and properties of organic liquids," *Journal of the American Chemical Society*, vol. 118, pp. 11225-11236, 1996.
- [181] J. Wang, *et al.*, "Development and testing of a general Amber force field," *Journal of Computational Chemistry*, vol. 25, pp. 1157-1174, 2004.

- [182] J. Applequist, *et al.*, "An atom dipole interaction model for molecular polarizability. Application to polyatomic molecules and determination of atom polarizabilities," *Journal of the American Chemical Society*, vol. 94, pp. 2952-2960, 1972.
- [183] C. L. Yaws, *Chemical Properties Handbook: Physical, Thermodynamic, Environmental, Transport, Safety, and Health Related Properties for Organic and Inorganic Chemicals*: McGraw-Hill, 1998.
- [184] E. Sloutskin, *et al.*, "The surface structure of concentrated aqueous salt solutions," *The Journal of Chemical Physics*, vol. 126, p. 054704, 2007.
- [185] Y. Zhao and D. Truhlar, "The M06 suite of density functionals for main group thermochemistry, thermochemical kinetics, noncovalent interactions, excited states, and transition elements: two new functionals and systematic testing of four M06-class functionals and 12 other functionals," *Theoretical Chemistry Accounts: Theory, Computation, and Modeling (Theoretica Chimica Acta)*, vol. 120, pp. 215-241, 2008.
- [186] R. A. Kendall, *et al.*, "High performance computational chemistry: An overview of NWChem a distributed parallel application," *Computer Physics Communications*, vol. 128, pp. 260-283, Jun 2000.
- [187] M. D. Baer, *et al.*, "Re-examining the properties of the aqueous vapor-liquid interface using dispersion corrected density functional theory," *Journal of Chemical Physics* vol. 135, 2011.
- [188] Y. Zhang and P. S. Cremer, "The inverse and direct Hofmeister series for lysozyme," *Proceedings of the National Academy of Sciences of the United States of America*, vol. 106, pp. 15249-15253, 2009.
- [189] W. L. Guest and W. C. M. Lewis, "The effect of electrolytes upon the interfacial tension between water and dekaline (trans-decahydronaphthalene)," *Proceedings of the Royal Society of London. Series A. Mathematical and Physical Sciences*, vol. 170, pp. 501-513, April 21, 1939 1939.
- [190] R. Aveyard and S. M. Saleem, "Interfacial tensions at alkane-aqueous electrolyte interfaces," *J. Chem. Soc., Faraday Trans.*, vol. 72, pp. 1600-1617, 1976.
- [191] P. K. Weissenborn and R. J. Pugh, "Surface tension of aqueous solutions of electrolytes: Relationship with ion hydration, oxygen solubility, and bubble coalescence," *Journal of Colloid and Interface Science* vol. 184, pp. 550-563, 1996.
- [192] Y. Levin, "Polarizable ions at interfaces," *Physical Review Letters* vol. 102, pp. 147803-4, 2009.

- [193] B. Kirby, *Micro- and Nanoscale Fluid mechanics*: Cambridge University Press, 2010.
- [194] J. L. F. Abascal, *et al.*, "The melting temperature of the six site potential model of water," *The Journal of Chemical Physics*, vol. 125, pp. 166101-2, 2006.
- [195] J.-P. Ryckaert, *et al.*, "Numerical integration of the cartesian equations of motion of a system with constraints: molecular dynamics of n-alkanes," *Journal of Computational Physics*, vol. 23, pp. 327-341, 1977.
- [196] A. M. Mathiowetz, "Dynamic and stochastic protein simulations: From peptides to viruses," California Institute of Technology, 1992.
- [197] H. C. Andersen, "Rattle: A "velocity" version of the shake algorithm for molecular dynamics calculations," *Journal of Computational Physics*, vol. 52, pp. 24-34, 1983.
- [198] B. Roux, "The calculation of the potential of mean force using computer simulations," *Computer Physics Communications*, vol. 91, pp. 275-282, 1995.
- [199] D. Frenkel and B. Smit, *Understanding Molecular Simulation: from Algorithms to Applications*: Academic Press, 2002.